

**Dissertation zur Erlangung des Doktorgrades
der Fakultät für Chemie und Pharmazie
der Ludwig-Maximilians-Universität München**

**Development of Two-Hybrid FRET applications to
investigate endolysosomal protein-protein
interactions**

**Colin Feldmann
aus
Hannover, Deutschland**

2024

Erklärung

Diese Dissertation wurde im Sinne von § 7 der Promotionsordnung vom 28. November 2011 von Herrn Christian Wahl-Schott betreut und von Herrn Martin Biel von der Fakultät für Chemie und Pharmazie vertreten.

Eidesstattliche Versicherung

Die Dissertation wurde eigenständig und ohne unerlaubte Hilfsmittel erarbeitet.

München, 13.05.2024

Colin Feldmann

Dissertation eingereicht am: 13.05.2024

1. Gutachter: Prof. Dr. Martin Biel

2. Gutachter: Prof. Dr. Christian Wahl-Schott

Mündliche Prüfung am: 20.06.2024

Table of Contents

Zusammenfassung.....	6
1 Summary	7
2 Introduction	8
Part I: Two-Hybrid FRET.....	9
2.1 Förster resonance energy transfer.....	9
2.2 The Two-Hybrid FRET assay.....	13
2.2.1 Spectral correction requires determination of the spectral correction factors R_{A1} , R_{D1} and R_{D2}	17
2.2.2 FRET calibration requires the determination of the calibration constants G_{ratio} and F_{ratio}	19
2.2.3 Determination of Binding curves	21
Part II: Proteins used in Two-Hybrid Fret assays.....	24
2.3 Calmodulin – MyosinVa reference protein interaction	24
2.4 Two-pore channels.....	27
2.5 The role of Rab GTPases for endosome maturation.....	30
3 Aim of the study.....	33
4 Methods.....	34
4.1 Generation of plasmids for Two-Hybrid FRET assays.....	34
4.2 Restriction-Ligation cloning and mutagenesis	34
4.3 Cell culture for Two-Hybrid FRET assays	35
4.4 Two-Hybrid FRET assay on a photometry setup	36
4.5 Two-Hybrid FRET assay on a flow cytometer.....	38
4.6 Image-based Two-Hybrid FRET measurements on a wide-field optical plate reader	38
4.7 Setup of automatic cell detection from wide-field images.....	39
4.8 Wide-field image conversion into data tables using automatic cell detection ...	41

4.9	Image-based Two-Hybrid FRET measurements on a confocal microscope.....	41
4.10	Confocal multi-stack image conversion into fluorescence data tables	42
4.11	Two-Hybrid FRET data analysis	43
4.12	Confocal image processing.....	43
4.13	2D mapping of FRET efficiencies (E_A and E_D).....	44
4.14	Mathematical background of FRET	44
4.15	Mathematical background of Two-Hybrid FRET binding curves.....	45
5	Results.....	51
	Part I: Two-Hybrid FRET development	51
5.1	Aim 1 – Advancements of the Two-Hybrid FRET method.....	51
5.1.1	Employing an optimized fluorophore pair for Two-Hybrid FRET.....	51
5.1.2	Design of novel, improved FRET calibration probes	52
5.1.3	Development of a custom made Matlab script for Two-Hybrid FRET data analysis54	
4.1.4	Validation of the photometry based Two-Hybrid FRET assay using a reference protein-protein interaction	55
5.2	Aim 2 – Development of a flow cytometry based Two-Hybrid FRET assay	57
5.3	Aim 3 – Development of an image-based Two-Hybrid FRET assay.....	58
5.4	Aim 4 – Development of a confocal Two-Hybrid FRET assay.....	63
	Part II: Characterization of Protein-Protein interactions using FRET assays.....	68
5.5	Aim 5 – Cross-validation of determining protein binding affinity on four instruments.....	68
5.6	Aim 6 – Subcellular Two-Hybrid FRET analysis of endolysosomal proteins.....	82
5.6.1	Co-localization of Rab7a and TPC2.....	82
5.6.2	Functional analysis of Rab7a wildtype and mutants with TPC2	83
5.6.3	Two-Hybrid FRET binding curves of Rab7a with TPC2	86
5.6.4	Two-Hybrid FRET binding curves of Rab7 with TPC1	88

5.6.5	Two-Hybrid FRET binding curve of Rab5 with TPC1.....	89
5.6.6	Two-Hybrid FRET binding curves of Rab7 with TRPML1-3.....	90
5.6.7	Two-Hybrid FRET binding curves of Rab7B with TPC2, TRPML1 and TPC1.....	93
6	Discussion.....	95
	Part I: Two-Hybrid FRET.....	95
6.1	Improvements to the Two-Hybrid FRET assay	95
6.2	Establishment and validation of the Two-Hybrid FRET assay on four devices	97
	Part II: Proteins used in Two-Hybrid FRET assays	100
6.3	Mutation of the IQ6 motif to alter its binding affinity to CaM	100
6.4	Analysis of protein interactions in the endolysosomal system	101
7	References	104
8	Publications.....	109
9	Appendix	110
9.1	List of abbreviations	110
9.2	Supplementary tables	112
9.3	Acknowledgements.....	119

Zusammenfassung

Meine Dissertationsarbeit beschäftigt sich mit der Entwicklung der Two-Hybrid FRET Methode an vier verschiedenen Messinstrumenten, die jeweils für spezielle Messanforderungen ausgelegt sind. Zusätzlich wurden mögliche Proteininteraktionen im endolysosomalen System untersucht. Im ersten Teil der Dissertation wurde die Two-Hybrid FRET Methode optimiert und an vier Instrumenten etabliert. Zuerst wurde das Two-Hybrid FRET Assay an einem Photometrie-Setup optimiert, indem ein potenteres FRET-Paar eingesetzt und neue FRET Kalibrationsdimere entwickelt wurden. Zusätzlich wurde die Datenevaluation und Bindungskurven Datenanpassung über ein Matlab Skript verbessert. Die Verbesserungen führten bei der gleichen Proteininteraktion zu einer 75 % erhöhten FRET-Signalsstärke (35 % FRET) im Vergleich zu früheren Ergebnissen (20 % FRET, Abbildung 12). Daraufhin wurde das Two-Hybrid FRET Assay an einem FACS (Flow Cytometer) Instrument etabliert. Dieses Instrument bietet einen hohen Messdurchsatz mit dem Nachteil von deutlich verringerter Messgenauigkeit. Letztlich wurde ein bildbasiertes FRET Assay an einem optischen Plattenlesegerät entwickelt. Die neue, bildbasierte Methode unterscheidet sich von den klassischen Two-Hybrid FRET Assays durch die Auswertung von Fluoreszenzbildern anstatt gemessener Fluoreszenz-Signale. Die bildbasierte FRET Methode zeichnet sich durch eine hohe Messgeschwindigkeit und guter Datenqualität aus. Weiterhin wurde eine konfokale bildbasierte Two-Hybrid FRET Methode entwickelt, welche die Analyse von Bindungskurven aus subzellulären Regionen ermöglicht. Diese Methode wurde außerdem weiterentwickelt, um ganze Fluoreszenzbilder in farbkodierte FRET-Effizienzen zu transformieren, was die orts aufgelöste Bestimmung von FRET Signalen in Fluoreszenzbildern ermöglicht.

Im zweiten Teil wurden die entwickelten Techniken angewandt. Die Referenz-Proteininteraktion zwischen Calmodulin und der IQ6-domäne von MyosinVa wurde mutiert, um die Protein-Bindungsaffinität zu verringern. Mit der mutierten Referenzinteraktion wurde verifiziert, dass die Bestimmung von relativen Bindungsaffinitäten mit dem bildbasierten Two-Hybrid FRET Assay zuverlässig ist. Das konfokale bildbasierte Two-Hybrid FRET Assay wurde dann verwendet, um mögliche Proteininteraktionen zwischen Rab-GTPasen und Ionenkanälen im endolysosomalen System zu untersuchen. Im Fokus dieser Untersuchungen stehen Rab7 und TPC2. Die Untersuchungen deuten auf vesikelspezifische Proteininteraktionen zwischen Rab-GTPasen und TPC-Kanälen hin.

1 Summary

In my thesis, the Two-Hybrid FRET assay was established on four different instruments and applied on putative protein-protein interactions, specifically proteins of the endolysosomal system. Part I focused on the overall improvement of the Two-Hybrid FRET methods and establishing the assay on four devices, which are tailored to specific needs in terms of speed and measurement fidelity. First, the Two-Hybrid FRET method was improved by employing a more potent FRET pair, new calibration constructs and an optimized fitting procedure. These improvements resulted in a 75 % increased dynamic range (35 % FRET) compared to previous results¹ (20 % FRET, Figure 12) using the same protein interaction on a similar photometry setup. Then, the Two-Hybrid FRET assay was established on a flow cytometer as a high-throughput version: This FRET assay yields over 50.000 data points in under one hour but suffers from inaccurate fluorescence quantification. An image-based Two-Hybrid FRET assay was developed on an optical plate reader. In contrast to previous methods, the image-based approach uses fluorescence images to generate binding curves, instead of raw fluorescence data. The image-based plate reader assay is a high-throughput assay similar to the flow cytometer-based assay, but with better fidelity. Further, the image-based Two-Hybrid FRET technique was developed on confocal microscopes, which allows for subcellular evaluation of binding curves. This method was then modified to transform fluorescence images into 2D FRET maps that visualize subcellular FRET signals color coded in corresponding, original confocal images, in parallel to the creation of Two-Hybrid FRET binding curves.

Part II focuses on the application of the developed techniques. The IQ6 motif from the reference interaction of CaM and the myosinVa IQ6 motif was mutated to generate an additional reference interaction with decreased binding affinity. This served to test the reliability of determining relative binding affinities, especially when using the confocal Two-Hybrid FRET assay. All devices were able to detect a decreased binding affinity and the confocal Two-Hybrid FRET assay is reliable even on different instrument configurations. Lastly, the confocal Two-Hybrid FRET assay was used to investigate putative protein-protein interactions in the endolysosomal system, with a focus on Rab7 and TPC2. These results indicate that small Rab GTPases indeed interact with TPC channels within the endolysosomal system, but in a vesicle dependent manner, so that the late-endosomal Rab7 only interacts with TPC2, while the early endosomal Rab5 only interacts with TPC1.

2 Introduction

My thesis focuses on the application of the Two-Hybrid FRET technique to investigate protein-protein interactions in living cells. The presented FRET applications are based on the non-radiative energy transfer between molecules, which was initially described by Theodor Förster at the Max Planck Institute in Göttingen²⁻⁴.

Starting point of my doctoral thesis was the Two-Hybrid FRET method published by the Wahl-Schott's group (Department of Pharmacy) at the LMU München in Butz et al. 2016¹. This Two-Hybrid FRET assay is based on a wide field fluorescence microscopy setup equipped with a photometry system. In the beginning of my doctoral thesis (September 2019) I established and extended this method together with Dr. Michael Schänzler at the Institute of Neurophysiology at the Hanover Medical School. I continued my work after relocation of the group from Hannover to Munich at the Institute of Cardiovascular Physiology and Pathophysiology at the Biomedical Center of the LMU in 2022.

The thesis is sectioned in into two interconnected parts. The first part focuses on developing and improving the Two-Hybrid FRET technique on four different devices: A wide-field photometry setup, a flow cytometer, an imaging plate-reader and a confocal microscope. The latter two FRET techniques are a novel, image-based approach while the first two are non-image based. In the second part, the techniques are applied to investigate the binding affinities of cytosolic protein interactions and also subcellular protein-protein interactions in the endolysosomal system.

In the introduction theoretical background will be given to introduce FRET in general and in particular with relation to the specific applications used in part I. Then background will be given about the specific proteins used for FRET assays in part II.

Part I: Two-Hybrid FRET

2.1 Förster resonance energy transfer

Following the foundational advancements in classical and quantum physics by scientists such as Perrin, Heisenberg, Oppenheimer, Dirac and Schrödinger in the 1920s⁵, Theodor Förster described an energy transfer mechanism between molecules based on dipole-dipole coupling in detail in the 1940s⁶. Later, these descriptions became the basis of what is now called the Förster Resonance Energy Transfer (FRET): When a donor molecule is excited, its electronic distribution changes, which causes a change in its dipole moment. This leads to an oscillation of the electron distribution within the dipole. If a nearby non-excited acceptor molecule has a dipole moment with a similar oscillation frequency, it can resonate with the excited donor. This resonance allows an energy transfer from the donor to the acceptor molecule based on matching charge oscillation frequencies without the exchange of photons (Figure 1 A). Importantly, FRET only occurs when both FRET partners are in close spatial proximity, with a distance of approximately 1-10 nm^{6,7} between donor and acceptor molecules.

The amount of FRET that occurs can be quantified by determining the FRET efficiency, which is the fraction of FRET related and total energy release. The process is illustrated in the kinetic schematic in Fig 1 B: An excited donor molecule returns from an excited state to the ground state predominantly through radiative decay (k_r), manifested as fluorescence emission, and through non-radiative relaxation (k_{nr}). If a non-excited acceptor fluorophore is present in close proximity, the FRET related de-excitation pathway (k_T) becomes available in addition to k_r and k_{nr} , giving rise to a third pathway of de-excitation that competes with the other two pathways (equation 1), (Figure 1 B). The FRET related de-excitation pathway leads to reduced donor fluorescence emission, because less energy is released through radiative decay (k_r). This reduction in donor fluorescence due to FRET is called donor quenching. Furthermore, FRET leads to enhanced acceptor emission, as the acceptor molecule is excited via FRET¹. The increase of acceptor fluorescence emission due to FRET is called sensitized emission.

Both FRET related emission changes (donor quenching and sensitized emission), quantified as individual FRET efficiencies, are denoted as E_D and E_A for donor and acceptor, respectively (Figure 1 C). Both FRET efficiencies depend on three key parameters (equations 2-5): 1. The overlap integral of the donor's emission with the acceptor's excitation spectra, 2. The

orientation factor of the FRET partners, and 3. The intermolecular distance between the FRET partners.

The last parameter has an extremely high impact on FRET efficiency, as the FRET efficiency is inversely proportional to the sixth power of the distance between the fluorophores, as shown in equation 2. As a consequence, distances below the diffraction limit⁸⁻¹⁰ in the range of 1 to approximately 10 nm can be measured by quantifying FRET efficiencies¹¹. Therefore, intermolecular distances can be successfully assessed by FRET, rather than by light microscopy. This includes protein-protein interactions, which can be measured using FRET signals.

In order to investigate intramolecular interactions by FRET, molecules of interest are linked to FRET donor and acceptor fluorophores¹². Depending on the interaction between two binding partners, there are several different applications for FRET in research. One common application is to characterize protein-protein interactions by quantifying FRET signals. In nucleic acid analysis, such as DNA hybridization¹³, FRET probes can indicate if DNA molecules hybridize. Furthermore, genetically encoded FRET sensors are used to assess pH values, Ca²⁺- or voltage-dependent signals in subcellular locations¹⁴. These molecules contain a FRET donor and acceptor separated by the sensing domain. If the sensor undergoes a conformational change, the distance between the fused FRET partners change and in turn affect the FRET efficiency. Due to the capability of measuring distances between 1-10 nm, FRET quantification is often referred to as a “molecular ruler”¹⁵.

In my doctoral thesis, I used FRET to investigate protein-protein interactions. For this purpose, several FRET techniques are available, with each of them having individual advantages and disadvantages: Protein-protein interactions can be measured by FRET either by quantifying the lifetime of an excited donor molecule. This approach is termed Fluorescence Lifetime Imaging (FLIM): FLIM exploits the fact that in presence of FRET, the excited donor molecules have a shorter lifetime in which they emit photons, because the available FRET related de-excitation pathway accelerates the return to ground state (Figure 1 A). Deriving FRET signals from the excited donor lifetime is a robust, but solely donor-centric FRET application¹⁶. FRET can also be determined by quantifying the FRET related emission changes via donor quenching or sensitized emission. This technique is called intensity-based FRET. It can be classified in

destructive and non-destructive methods: Destructive FRET approaches rely on two measurements that quantify donor fluorescence in the presence and absence of a FRET acceptor by photo-bleaching the acceptor¹⁷. Acceptor photo-bleaching (APB) is a solely donor-centric FRET quantification. Non-destructive FRET approaches^{11,18} quantify FRET related emission changes from total fluorescence intensities of donor and acceptor emission in channels with specific spectral properties to separate the emission from each of the two fluorophores.

The FRET approach used in my doctoral thesis is the Two-Hybrid FRET method^{1,19-21}. The method was developed from intensity-based FRET methods described above and incorporates the simultaneous and non-destructive quantification of both, donor quenching and sensitized emission. The quantification and comparison of both FRET efficiencies can yield information about the binding stoichiometry and maximum FRET efficiencies of each FRET partner, by estimating the donor and acceptor concentration¹⁹. FRET assays are best suited to complement other approaches when investigating protein-protein interactions: In contrast to co-immunoprecipitation, FRET assays have a lower probability of false-positive signals. On the other hand, the rate of false negatives using FRET methods is higher. Thus, an optimal approach to investigate a set of proteins is to employ both methods consecutively, with co-immunoprecipitation followed by mass-spectrometry being the first test to detect a limited number of interesting interaction candidates that are further investigated using FRET assays.

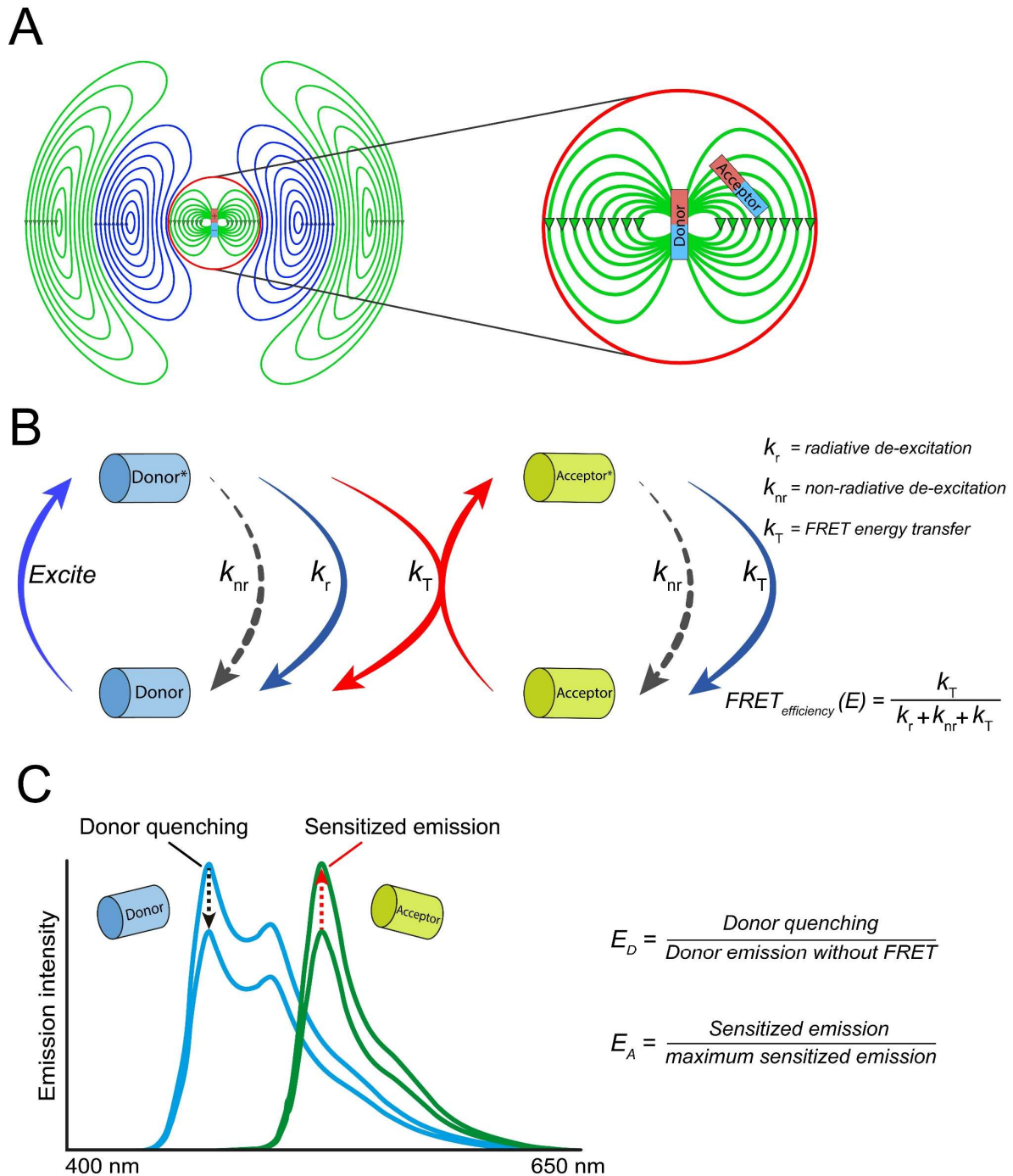


Figure 1: Principle of Förster Resonance Energy Transfer: **A**, FRET is an energy exchange between two dipoles without photon exchange: The electric field of a donor dipole is depicted on the left. The area within the red circle displays the electrical near-field, the outer area depicts the emitted waves in the transition zone and electrical far-field. Waves that separate from the dipole (photon emission) only occur outside of the near field. The right image displays the near field in presence of an acceptor dipole. FRET occurs in a small area within the near-field, in approximately 1-10 nm distance of the donor dipole. The frequency in which the polarity of the donor dipole changes can resonate with an acceptor dipole, hence the name Resonance Energy Transfer. **B**, De-excitation pathways of a donor molecule in the presence of a FRET partner: A photon is absorbed by the donor, leading to an electronically excited state (Donor*). The fluorophore transitions into ground-state by releasing energy via radiative decay (k_r), nonradiative relaxation (k_{nr}) and FRET (k_T). Pathways of excitation and relaxation are indicated by arrows. Note that the FRET related pathway excites the acceptor while the donor relaxes. The FRET efficiency (E) is denoted as the fraction of energy that is released via FRET (k_T) in relation to the sum of all

de-excitation pathways, as indicated on the right. **C**, The FRET related emission changes of donor and acceptor emission are displayed. The emission spectrum for the donor is shown in blue, the emission of the acceptor in green: When FRET occurs, the donor emission is quenched (E_D), shown by a black dotted arrow. Simultaneously, the acceptor emission is sensitized (E_A), shown by a red dotted arrow. Emission values shown here are normalized. Using the equations on the right, both phenomena (E_D and E_A) can be expressed as absolute FRET efficiencies.

2.2 The Two-Hybrid FRET assay

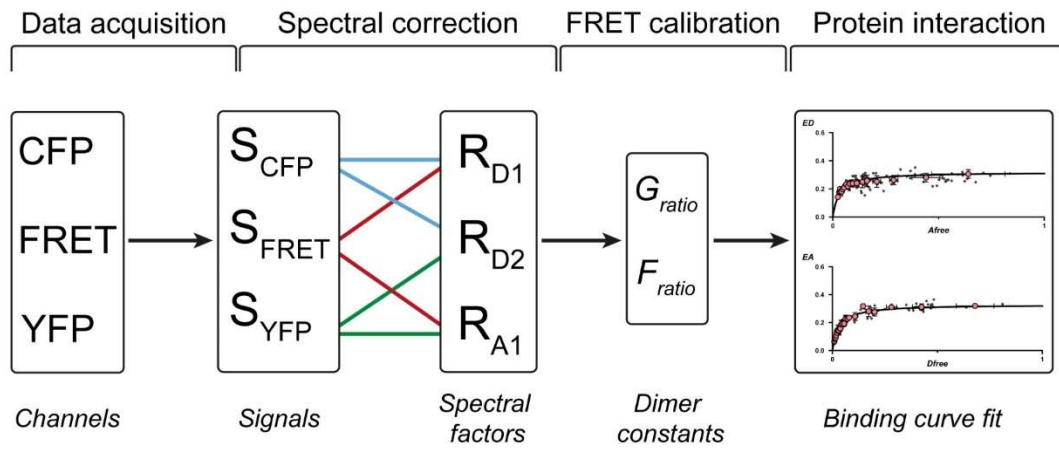
The “Two-Hybrid FRET assay” is named in analogy to the yeast Two-Hybrid system, as both methods employ fusion proteins to investigate protein-protein interactions. Recently, the Two-Hybrid FRET assay has been described both mathematically and experimentally, for wide-field photometry setups^{1,19,21,22} and flow cytometers^{23,24}. In the Two-Hybrid FRET assay, one protein is fused to a donor fluorophore and the other to an acceptor fluorophore, allowing both proteins of interest to form a FRET pair. The Two-Hybrid FRET assay relies on a three-cube or three-channel FRET setup^{25,26}, which embody three separate fluorescence channels for signal acquisition: The CFP channel aims to excite donor molecules while measuring donor fluorescence emission. The FRET channel is designed to excite donor molecules and to measure acceptor related emission. The YFP channel is for acceptor excitation and for measuring acceptor emission. The three quantified fluorescence signals are then termed S_{CFP} , S_{FRET} and S_{YFP} , which are derived from a cell under investigation (Figure 2 A). The first important measurement in the workflow is the spectral correction (Figure 2 A). Spectral correction is necessary to adjust for crosstalk in the measured fluorescence signals due to the overlapping excitation and emission spectra of the donor and acceptor (Figure 3 A). This is achieved by determining three spectral correction factors (R_{D1} , R_{D2} , R_{A1}).

The second essential measurement in the workflow is to calibrate the assay by 1.) scaling the excitation dependent properties (equation 12) of the donor fluorophore to the acceptor fluorophore by determining the G_{ratio} , and 2.) by scaling the emission dependent properties (equation 13) of the acceptor fluorophore to those of the donor fluorophore by determining the F_{ratio} . In order to perform spectral correction and FRET calibration, several donor-acceptor fusion constructs are required which are listed in Table 1 and depicted in Figure 2 B.

Using the Two-Hybrid FRET assay, two distinct binding curves can be determined: Each binding curve corresponds to either the donor or acceptor FRET efficiency. The protein binding

parameters $E_{A,max}$ and $E_{D,max}$, derived from the asymptotic maximum of the curve, describe the maximum FRET efficiency of each FRET partner under optimal conditions. In addition, the K_D -value, which is the relative dissociation constant of a given protein-protein binding reaction, can be determined from the half-maximum. This parameter is also named $K_{D,eff}$ in previous literature, because it is derived from the binding model that is applied to the data and therefore likely represent an apparent K_D rather than the absolute K_D .

A



B

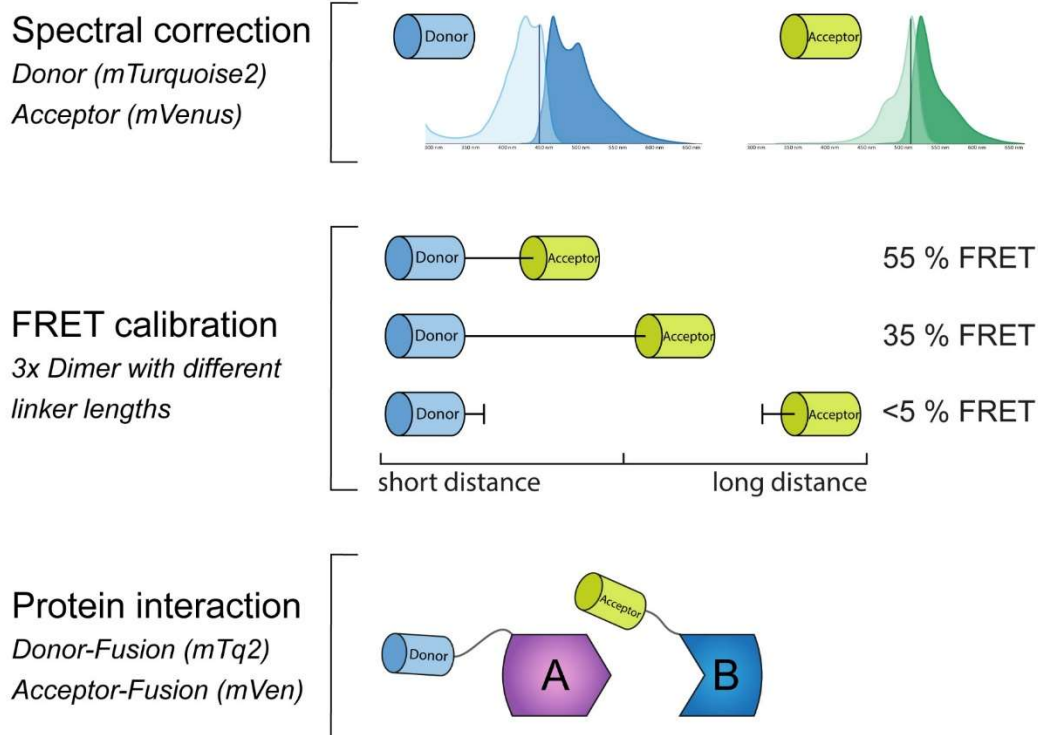


Figure 2: Workflow of the Two-Hybrid FRET assay. A, Required steps for creating Two-Hybrid FRET binding curves from a protein interaction are shown: First, each measurement is conducted in three distinct fluorescence-channels as depicted in the step “Data acquisition” (CFP, FRET, YFP). Each measurement in one channel is converted into a fluorescence signal, which correspond to the channel they were acquired in (S_{CFP} , S_{FRET} , S_{YFP}). The fluorescence signals (S_{CFP} , S_{FRET} , S_{YFP}) are corrected in the spectral correction step to yield the pure fluorescence signals corresponding to donor emission, FRET emission and acceptor emission. The FRET calibration step yields the G_{ratio} and F_{ratio} and is required to calculate the absolute FRET efficiencies for both the donor and acceptor (E_D and E_A), as well as relative donor and acceptor concentration from the spectrally corrected S_{CFP} , S_{FRET} , and S_{YFP} signals. Lastly, measurement data (S_{CFP} , S_{FRET} , S_{YFP}) from protein interaction samples can be plotted in form of binding curves against the relative concentration of free FRET partners (E_A against

donor-tagged proteins, E_D versus acceptor-tagged proteins) using the spectral correction factors, the FRET calibration ratios and a Langmuir binding isotherm. **B**, Required constructs for the calibration and protein interaction analysis are displayed: The Two-Hybrid FRET assay requires the determination of three spectral correction factors (R_{A1} , R_{D1} , R_{D2}) and two FRET calibration constants (G_{ratio} and F_{ratio}). Spectral correction factors are acquired by measuring cells expressing the acceptor fluorophore only (R_{A1}) and subsequently measuring cells expressing the donor fluorophore only (R_{D1} , R_{D2}). The dimer constants are determined by measuring three different dimer constructs individually. Each of these samples produce stable and equal FRET efficiencies for both E_D and E_A . The analysis of a protein interaction requires that one protein is tagged to the donor-fluorophore (depicted as protein A) and the other to the acceptor-fluorophore (depicted as protein B).

Determined Parameters	Constructs transfected
Spectral correction R_{A1} , R_{D1} , R_{D2}	donor fluorophore only acceptor fluorophore
FRET calibration G_{ratio} , F_{ratio}	short dimer medium dimer long dimer
Test interaction Binding curves E_A and E_D	fusion protein 1 + donor Fluorophore fusion protein 2 + acceptor Fluorophore
Scramble DNA Background subtraction	empty vector backbone

Table 1: Required samples for Two-Hybrid FRET assays. This table lists all required constructs to conduct a Two-Hybrid FRET assay: Two constructs expressing either the donor or acceptor are necessary for determining the spectral correction factors R_{A1} , R_{D1} and R_{D2} . Furthermore, three dimer constructs are used to determine the FRET calibration coefficients F_{ratio} and G_{ratio} . These dimers contain the donor and acceptor separated by a linker of specific length (short, medium and long) thus giving rise to high, medium and low FRET efficiency, individually. In addition, two constructs are used, coding for two proteins of interest, which potentially interact with each other. The interaction of these two proteins of interests can be determined by Two-Hybrid FRET. The interaction can be quantified by determining two different FRET binding curves, one for E_A and one for E_D . The first construct is designed by fusing the donor fluorophore to the N- or C-terminus of the first protein of interest. For the second construct, the acceptor fluorophore is fused to the N- or C-terminus of the second protein of interest (Figure 2 B). For the background sample, an empty expression vector is used.

2.2.1 Spectral correction requires determination of the spectral correction factors R_{A1} , R_{D1} and R_{D2}

FRET pairs usually inhabit a spectral overlap in the excitation and emission spectra between the donor and acceptor. The overlap between the donor emission spectrum and the acceptor excitation spectrum is required for FRET to occur (equation 4). However, if both excitation spectra overlap as well, the targeted donor excitation leads to a cross-excitation of the acceptor and vice versa. Similarly, if both emission spectra overlap, the measured emission of the donor will contain fractions of acceptor emission and vice versa. This phenomenon is depicted in Figure 3 A, displaying the excitation overlap and emission overlap for a given FRET pair. Therefore, it is necessary to apply a spectral correction to calculate and subtract the emission signals that arise from cross-excitation due to the excitation spectra overlap and the bleed-through of emission from the emission spectra overlap in the three channels used for the Two-Hybrid FRET fluorescence acquisition²⁷. The emission signals that arise from the spectral overlaps in the FRET channel are displayed in Figure 3 B. By employing spectral correction factors, the fundamental emission quantities can be calculated, as depicted in Figure 3 D: These emission quantities are the donor emission from direct excitation (CFP_{direct} , equation 9), acceptor emission from donor excitation (YFP_{FRET} , equation 11) and acceptor emission from direct excitation (YFP_{direct} , equation 10). The spectral correction factors are determined by measuring the single-fluorophore samples (monomers of the donor and acceptor fluorophore individually) and plot fluorescence signals (S_{CFP} , S_{FRET} and S_{YFP}) against each other, as shown in Figure 3 C. From the slopes of the linear relationship of these signals, the fractional amount of cross-excitation (R_{A1} , R_{D2}) and emission bleed-through (R_{D1}) can be determined. R_{A1} relates the cross-excitation of acceptor molecules from the FRET channel to the direct excitation via the YFP channel (equation 6). R_{D2} relates the CFP cross-excitation via the YFP channel to the direct excitation via the CFP channel (equation 8). R_{D1} is the fractional amount of CFP emission that is measured via the FRET cube (equation 7). Spectral correction factors for a given FRET pair should remain stable over weeks on an instrument, as they are solely dependent on the properties of the setup in use and spectral properties of the fluorophores.

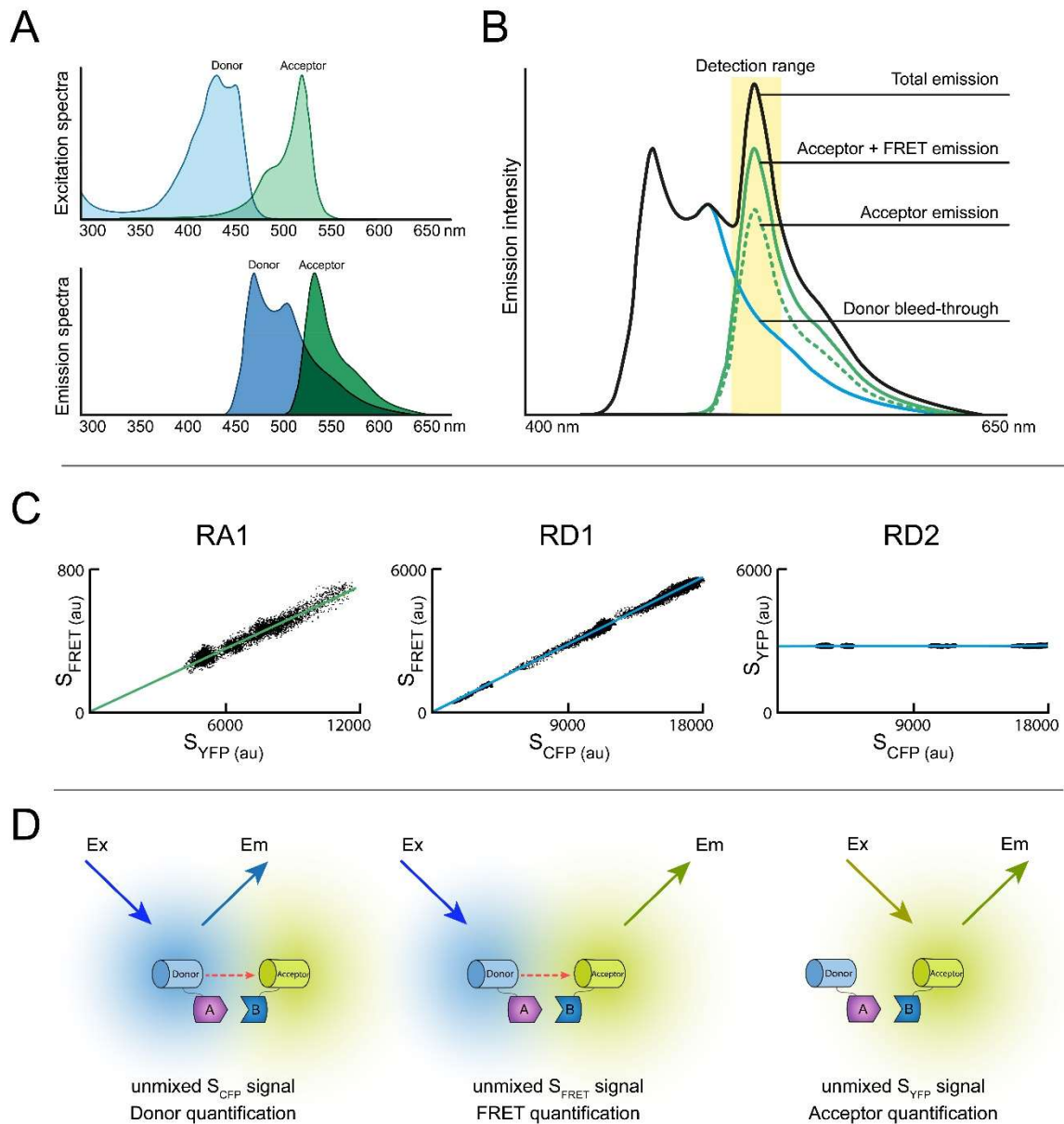


Figure 3: Spectral correction of fluorescence signals. **A**, The spectral overlap of the excitation (top) and emission (bottom) spectra from the FRET donor (mTurquoise2) and the FRET acceptor (mVenus) are displayed. Blue graphs show spectra of the donor and green graphs spectra of the acceptor. Because of these overlaps, measurements in each of the three FRET channels contain bleed-through or cross-excitation dependent fluorescence signals that have to be subtracted from the total fluorescence intensity measured. **B**, The black line indicates the overall emission spectrum of both donor and acceptor combined. The detection range of the FRET acceptor fluorescence signals in the FRET and YFP channel is highlighted in yellow. The fluorescence emission of the acceptor in the FRET channel can be dissected into three components: 1. The acceptor emission contains the FRET induced sensitized emission (green line). 2. The acceptor is directly cross-excited from the donor directed excitation light in the FRET channel (dotted green line). 3. The donor emission partially bleeds into the detection range of the FRET channel (blue line). All signals add up to the total emission measured when assessing the acceptor emission (black line). **C**, To quantify the dissected emission signals, three spectral correction factors are required. These are determined experimentally by measuring a sample containing the acceptor only (for spectral correction factor R_{A1}) and a sample containing the donor only (for spectral correction factors R_{D1} and R_{D2}) in all three channels. The cross-excitation of the FRET acceptor due to donor directed excitation in the CFP channel is expressed as R_{A1} . R_{A1} is the slope of the linear relationship of fluorescence intensities of the acceptor in the YFP

channel (S_{YFP} ; Y-axis) and the intensities of the acceptor in the FRET channel (S_{FRET} , X-axis, leftmost diagram, green line). The other two spectral factors are determined measuring donor molecules only: The donor emission bleed-through in the acceptor detection range is expressed as R_{D1} . R_{D1} is the slope of the linear relationship between the donor emission intensities in the CFP channel (S_{CFP}) and the donor emission intensities in the FRET channel (S_{YFP} , central diagram, blue line). In parallel, the donor intensities in the CFP channel (S_{CFP}) are plotted against the donor intensities in the YFP channel (S_{YFP}) to determine the cross-excitation of the donor through acceptor directed excitation in the YFP channel. Similarly, the slope of the linear relationship yields the spectral factor R_{D2} (blue line, rightmost graph). **D**, After the spectral correction, the emission signals from all three channels (S_{CFP} , S_{FRET} , S_{YFP}) can be calculated into pure emission quantities: The signals measured in the CFP channel are calculated into donor emission from direct donor excitation only. This signal might be quenched due to FRET, which is assessed in a calculation step afterwards. The signal measured in the FRET channel is calculated into FRET related sensitized emission of the acceptor from donor excitation only, and the signal measured in the YFP channel is transformed into acceptor emission from direct acceptor excitation only.

2.2.2 FRET calibration requires the determination of the calibration constants G_{ratio} and F_{ratio}

Calculating absolute FRET efficiencies from donor quenching (E_D) and the sensitized emission (E_A), as shown in equation 17 and 18, requires the determination of two FRET calibration constants, The G_{ratio} and F_{ratio} . In order to determine these constants, fusion proteins are used that contain a donor and acceptor fluorophore separated by a linker (Figure 4 A). These fusion proteins, termed dimers^{11,28}, generate stable and equal FRET efficiencies ($E_D = E_A$) in a strict 1:1 stoichiometry ($N_D = N_A$), as depicted in Figure 4 B. Three dimers are measured individually and plotted into a diagram as displayed in Figure 4 C. The FRET calibration constants G_{ratio} and F_{ratio} can be derived from the linear relationship of these dimer measurements.

Determination of the G_{ratio} relates excitation properties of the FRET partners

The excitation properties of both FRET partners depend on the excitation light, the excitation spectrum of each fluorophore and their respective extinction coefficient (equation 12). Measuring dimers in all three Two-Hybrid FRET channels and plotting them according to Figure 4 C results in a linear relationship. From the slope of the linear regression (equation 19), the G_{ratio} is derived, which relates the extinction properties of the donor to the acceptor when excited via the instrument specific excitation light in a given FRET channel.

Determination of the F_{ratio} relates emission properties of the FRET partners

Additionally, the F_{ratio} is determined to account for the different emission properties of the fluorophores at a given excitation wavelength (equation 13). Analogous to the G_{ratio} , the F_{ratio} is determined from the Y-axis offset from various measurements of dimers that are plotted in a diagram as displayed in Figure 4 C.

The FRET calibration determines both the G_{ratio} and F_{ratio} . This terminology is derived from Rivas et al. 2021 and outlined in equation 12 and 13. Both ratios have a significant impact on the accuracy of FRET measurements, thus the FRET calibration has to be optimized thoroughly^{18,29}. Small derivations in the calibration can have a great impact on the estimated K_D and maximum FRET efficiencies. Consequently, three dimer constructs are used to facilitate a linear regression instead of two (Figure 4 C). Further, these dimer constructs ideally yield very distinct FRET efficiencies due to different linker lengths, which place the fluorophores at varying distances to each other, as indicated in Figure 4 C (dimers 1-3, shown in grey, red and yellow).

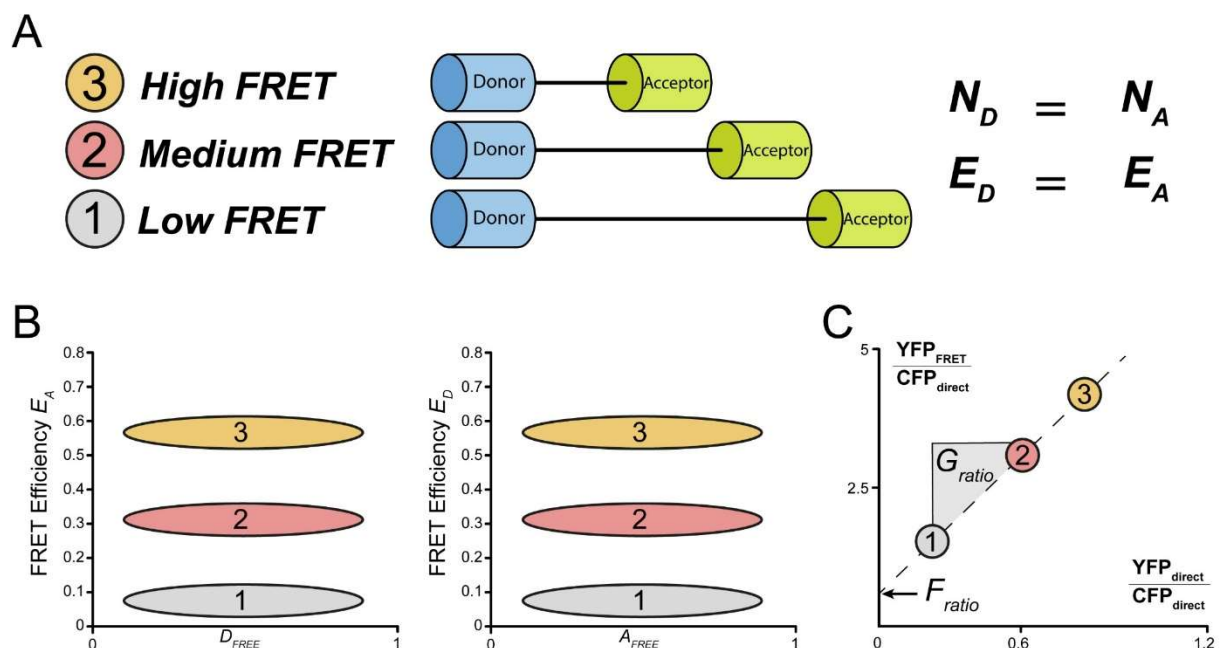


Figure 4: Functionality of FRET calibration constructs (dimers). **A**, Two-Hybrid FRET calibration requires three dimers (1-3) with different FRET efficiencies. These dimers contain linkers of different lengths, as shown in the center. The approximated number of donor molecules (N_D) and acceptor molecules (N_A) is equal for each dimer (1:1 stoichiometry). Additionally, the FRET efficiency from donor quenching (E_D) and sensitized emission (E_A) is equal for each dimer as well. **B**, Expected results when measuring each dimer individually and plotting the data

on Two-Hybrid FRET diagrams: The “Low FRET” dimer, which inhabits a long linker, results in a low FRET efficiency for both E_A and E_D . Expected data points are indicated as a grey ellipse. Further, the “Medium FRET” dimer (red ellipses) and “High FRET” dimer (yellow ellipses) result in stable and higher FRET efficiencies as shown. **C**, To determine the G_{ratio} and F_{ratio} from the dimer measurements, a graphical analysis of the raw data obtained from each dimer sample is required. The relative amount of sensitized emission (Y-axis) and donor quenching (X-axis) form a linear relationship when all dimer data are plotted (grey, red and yellow circles). The graphical analysis of the Y-intercept and slope of the regression line is used to obtain the G_{ratio} and F_{ratio} , respectively (equation 19).

2.2.3 Determination of Binding curves

After determining the spectral correction factors R_{A1} , R_{D1} and R_{D2} , as well as the FRET calibration constants G_{ratio} and F_{ratio} , two distinct binding curves can be calculated by using the fusion constructs of the proteins of interest, one accounting for donor-related FRET efficiencies (E_D) and the other for acceptor-related FRET efficiencies (E_A). Both FRET efficiencies are plotted individually against the concentrations of their free opposite FRET partners: E_A versus free donor concentration, E_D versus free acceptor concentration. The purpose is to enable a nonlinear fit of the data analogous to a Langmuir binding isotherm. In the context of a Langmuir binding model, it can be assumed that the FRET donor acts as a ligand and the acceptor as a receptor, and vice versa: Thus, the acceptor-related FRET efficiencies E_A (Y-axis, analogous to bound receptors) are plotted against free donor (X-axis, analogous to free ligand) concentration. The E_D binding curve is similar plotted, but with the donor representing the receptor and the acceptor representing the ligand instead. This is done because FRET efficiencies from both donor and acceptor depend on the abundance of the opposite FRET partner: In a given scenario where donor molecules are in excess compared to acceptor molecules, the measured donor FRET efficiency is low, because large amounts of donor molecules are unable to find an acceptor molecule for binding. However, in this scenario, the measured acceptor FRET efficiency is high, because all acceptor molecules are able to bind to donor molecules (Figure 5 B). Therefore, the protein-protein interaction samples are measured under various scenarios with varying donor and acceptor concentrations ideally, to cover both binding curves with data points along their X-axes (Figure 5 A).

Using this binding model, the concentration of FRET partners that is required until the FRET maximum is reached provides insight into the relative binding affinity. The relation between the maximum donor-related FRET efficiency ($E_{D,max}$) and acceptor-related FRET efficiency

($E_{A,max}$) gives insight about the apparent binding stoichiometry: In case of a 1:1 binding stoichiometry, the maximal donor and acceptor FRET efficiencies are similar. However, if, for example, two donor molecules undergo FRET with one acceptor molecule, the FRET efficiency of each donor (E_D) is half of the amount of the acceptor (E_A).

However, the classical Langmuir binding model makes the assumption of a fixated receptor on a monolayer, which is different in protein-protein interactions (Figure 5 B), where both partners are mobile in most cases. Further, by using this binding model, the Two-Hybrid FRET assay simplifies protein-protein interactions, neglecting factors like 3D diffusion, orientation, and protein binding cooperativity. Most importantly, it also doesn't consider collision dependent FRET signals³⁰, which occur when the tagged proteins come in close proximity at high concentrations in a confined space. Collision dependent FRET signals are significantly increased if the fluorophore tags tend to dimerize with each other. This leads to two consequences: The Two-Hybrid FRET assay only allows for determining a K_D that diverges from the true K_D due to the limited binding model, notably when applied to complex protein-protein interactions²². Therefore, measured K_D values were normalized to a reference interaction for a comparative analysis (e.g., wildtype vs. mutants) in my thesis. Further, the impact of collisional FRET on binding curves was assessed but not corrected: Collisional FRET signals were previously estimated by measuring non-interacting FRET pairs experimentally. However, FRET signals that occurred due to collisional FRET at physiologically relevant concentrations were negligible, especially when using fluorophores that do not tend to dimerize²¹.

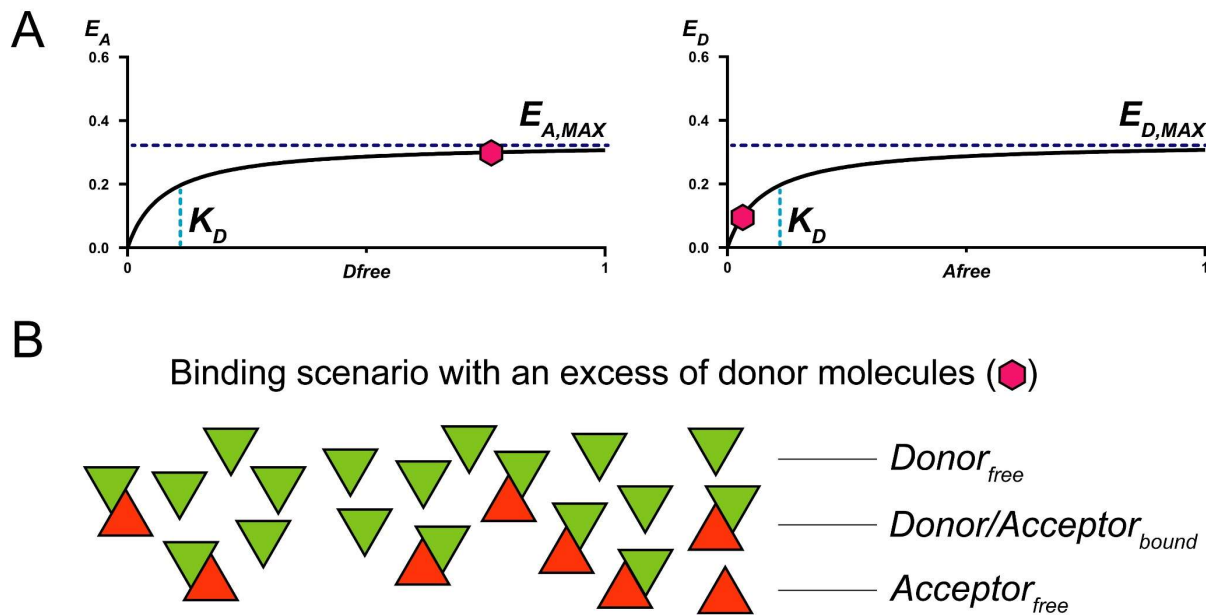


Figure 5: Two-Hybrid FRET binding curve generation. **A**, The FRET efficiencies are dose dependent, E_D is plotted as a function of free acceptor concentration, E_A is plotted as a function of free donor concentration. The relative K_D and the estimated FRET maxima for E_D and E_A can be derived from the dotted lines as indicated, after enough data points were obtained to generate the fit. The fit is displayed as a black line. Interrelation of E_A and E_D plots: a point in the saturating part of E_A function (magenta symbol, left diagram) corresponds to a point in the early ascending part of the E_D function (magenta symbol, right diagram). The magenta symbols depict a measurement point of a sample with an excess of donor molecules, which results in a low fractional number of bound donors, thus a low measured E_D FRET value (right diagram). In contrast, almost all acceptor molecules are bound which results in a high measured E_A value (left diagram). **B**, The molecular scenario of the measurement point indicated by the magenta symbols is depicted. Analogous to the Langmuir binding isotherm, E_A and E_D diagrams are plotted as follows. E_A diagram: The acceptor (red molecule) is the receptor, which is mostly bound (high E_A value), because the ligand, which represents the donor, (green molecule) is present in excess (high D_{free} value). The E_D diagram: The donor (green molecule) is the receptor, which is rarely bound (low E_D value), because the ligand, which represents now the acceptor (red molecule) is present in low amounts (low A_{free} value). Due to this interrelation, the E_A and E_D binding curves are generated by measuring multiple scenarios with varying donor:acceptor abundancies to cover both the curves with data points along the x-axis.

Part II: Proteins used in Two-Hybrid FRET assays

The following section describes the proteins used for the reference standard, then the endolysosomal cation channels and their potential interacting proteins will be introduced.

2.3 Calmodulin – MyosinVa reference protein interaction

The known and highly potent protein-protein interaction between calmodulin (CaM) and the IQ6 motif of myosinVa was used as a reference protein interaction to validate the four Two-Hybrid FRET assays developed.

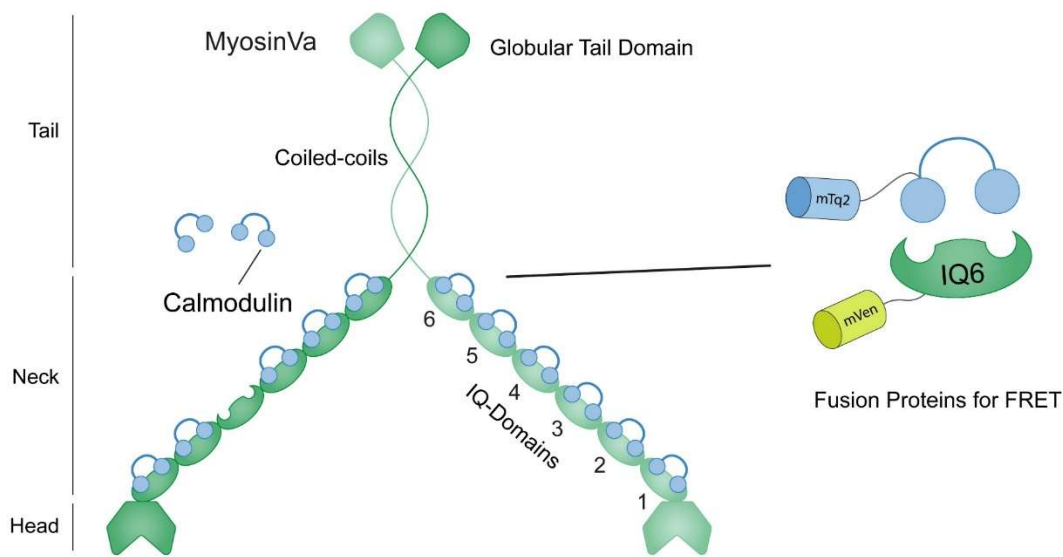
CaM is a Ca^{2+} binding protein which is highly conserved among eukaryotes. It contains two globular domains, connected by a linker. Each of the globular domains contains a pair of EF-hand motifs, each of which can bind one calcium ion³¹. Upon binding of calcium, the conformation of this protein changes³² from a compact (Ca^{2+} -free apo CaM) to an extended form (4Ca^{2+} -CaM). CaM is well known to bind to canonical IQ motifs³³. IQ motifs are conserved sequences that bind CaM domains³³. The IQ motif used for the FRET assay was derived from the unconventional myosinVa protein and resembles the canonical sequence of the upmost IQ6 motif in the neck region (Figure 6 A). MyosinVa³⁴ is a homodimeric motor-protein that facilitates transport of vesicles and cargo along microtubules by a mechanism that involves Rab GTPases³⁵⁻³⁷. It consists of three distinct regions³⁸ (Figure 6 A): 1. The C-terminal tail-region consists of a globular domain that binds cargo and coiled-coils that connect both monomers. 2. The neck region consists of six IQ motif repeats that bind CaM. 3. The N-terminal head region comprises a domain that binds to the actin filament. The unconventional myosinVa is particularly abundant in melanocytes and neurons. A dysfunctional myosinVa leads to the Griscelli syndrome, which leads to pigmentation loss and neurological impairment³⁹.

Each of the 6 IQ motifs in the neck region is able to bind one CaM³³. The calcium association with CaM induces a conformational change in CaM and consequently changes the structure of the neck region of myosinVa. The calcium and CaM dependent movement along the actin filament is often referred to as the “power stroke”⁴⁰. CaM can bind without calcium (apo-CaM) and with calcium (holo-CaM), and its calcium dependent conformational change directly

interacts with the helical structure of the neck region of myosinVa due to its distinct claw-shaped form that changes upon binding with calcium (Figure 6 B). The CaM binding to the IQ motif relies on a conserved IQ motif sequence that is not only similar between all IQ motifs of myosinVa (IQ1-6), but also similar between different proteins in different species that also contain IQ motifs of any kind²⁰.

To generate the reference FRET pair for the FRET Two-Hybrid assay, mTq2 (mTurquoise2) was fused to the N-terminus of CaM (mTq2–CaM) and mVen (mVenus) to the N-terminus of the IQ6 domain of myosinVa (mVen-IQ6 WT). The fusion proteins are depicted in detail in Figure 6 A. The reference FRET assay of mTq2–CaM with mVen-IQ6 WT was conducted at resting Ca²⁺ concentrations.

A



B

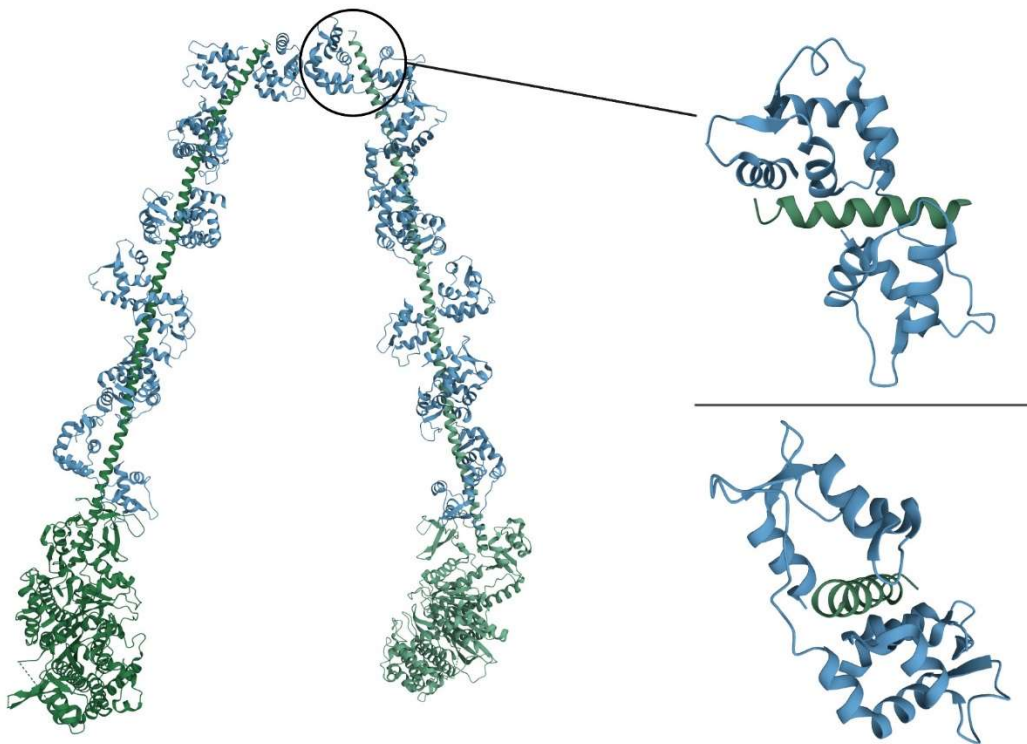


Figure 6: Reference protein interaction for Two-Hybrid FRET. **A**, Schematic view of MyosinVa (green), which comprises of a Head (N-terminus), Neck and Tail region (C-terminus). The IQ motifs are numbered from 1 to 6. Blue objects represent CaM proteins at their respective binding location. The FRET reference constructs are displayed on the right, fused to their corresponding fluorescent FRET partners. **B**, Cryo-EM structure of the MyosinVa protein (green) with bound CaM proteins (blue, PDB ID: 2DFS)⁴¹. Only the Neck and Head region of the MyosinVa protein are displayed. Six CaM molecules bind to the IQ motifs and are colored in blue. The Binding geometry of the IQ6 motif to a CaM protein is shown in two perspectives on the right.

2.4 Two-pore channels

Two-Pore channels (TPCs) are intracellular ion channels, which have been shown to be key regulators of ion homeostasis in organelles and in particular intracellular trafficking of endosomes and lysosomes. TPCs share sequence homology with members of the TRP channel superfamily, in particular with TRPML1-3, TRPV5 and TRPV6 channels⁴². TPCs are homodimers that form together 24 transmembrane domains and a pore⁴³ (Figure 7). Each monomer contains two similar repeats of 6 transmembrane domains. The transmembrane regions 1-6 (TM 1-6) of domain I are linked to TM7-12 of domain II by an intracellular linker which is exposed to the cytosol, and which contains two EF-hand motifs (Fig. 8). The two-domain topology of TPCs is unique across cation channels and name-giving for the channels. TPC channels are assumed to be evolutionary intermediates between the one-domain (1x6) Ca²⁺- or Na⁺- channels and four-domain (4x6) K⁺ channels^{44,45}. The pore region of the channel is formed by transmembrane domains 5 and 6 which are linked by the pore loop and the selectivity filter (Figure 7).

In humans and mice there are 2 TPCs, named TPC1 and TPC2^{46,47}, which appear to be expressed in all tissues. The research groups of Prof. Biel, Prof. Wahl-Schott and Prof. Grimm and others have demonstrated that TPC1 and TPC2 are endolysosomal cation channels mainly permeable to Ca²⁺ and Na⁺ (Figure 7 D) that are activated by NAADP and PI(3,5)P₂ (an endolysosomal membrane phosphoinositol) and inhibited by interaction with mTOR (mammalian target of rapamycin), which is reviewed in Grimm, C., Chen, C. C., Wahl-Schott, C., & Biel, M. (2017)⁴⁸. TPC1 is localized in early endosomes and TPC2 at late endosomes.

Functional studies of the Wahl-Schott's group and others revealed 2 findings key to TPC2 function: 1. TPC2s are required for fusion of late endosomes (LEs) and lysosomes (LY)⁴⁸⁻⁵⁰; 2. LEs and their precursors, multivesicular bodies (MVB), can transport complex cargo—including low density lipoprotein, growth factors, transferrin, integrins, viruses (e.g. Ebola and coronaviruses), and bacterial toxins^{48,51}, and these molecules and pathogens accumulate when TPC2 is suppressed^{48,50,51}. In my work, the investigation of endolysosomal proteins focuses mainly on the TPC2 channel.

The precise control of calcium release is required for the effective functioning of the trafficking in the degradation pathway⁵². The permeability of TPC2 for Ca²⁺ and Na⁺ is regulated by

specific ligands⁵³: NAADP is a calcium modulator^{54,55} and a ligand of TPC2 that has shown to alter the permeability⁵⁶ for Ca²⁺. NAADP controlled Ca²⁺ release plays a crucial role in maturing endosomes, as it is required for proper trafficking^{57,58}. Further, the mTOR complex bound to ATP acts as an inhibitor on the TPC2 dependent Ca²⁺ release⁵⁹ (Figure 7 D), while proteins that interact directly with NAADP also influence TPC2 dependent Ca²⁺ release, such as LSM12⁶⁰. PI(3,5)P₂ is a membrane lipid that is found in the membranes of late endosomes and has shown to promote the permeability of Na⁺ in TPC2 channels^{61,62}. TPC2 is a key modulator for melanosomes. Polymorphisms in the TPC2 gene lead to phenotypic variations of hair color and pigmentation⁶³. There is growing evidence that pigmentation directly depends on the affinity of PI(3,5)P₂ to TPC2 and the pH⁶⁴. The effects of NAADP and PI(3,5)P₂ on TPC2 are supported by experimental data using synthetic compounds mimicking either NAADP (TPC-A1-N) or PI(3,5)P₂ (TPC-A1-P)⁶⁵ in vitro. TPC2 plays an essential role in the integrity of the degradation pathway⁶⁶. The interplay of TPC channels and other endolysosomal proteins, specifically TPC2 with other LE associated proteins such as the GTPase Rab7, is therefore of special interest.

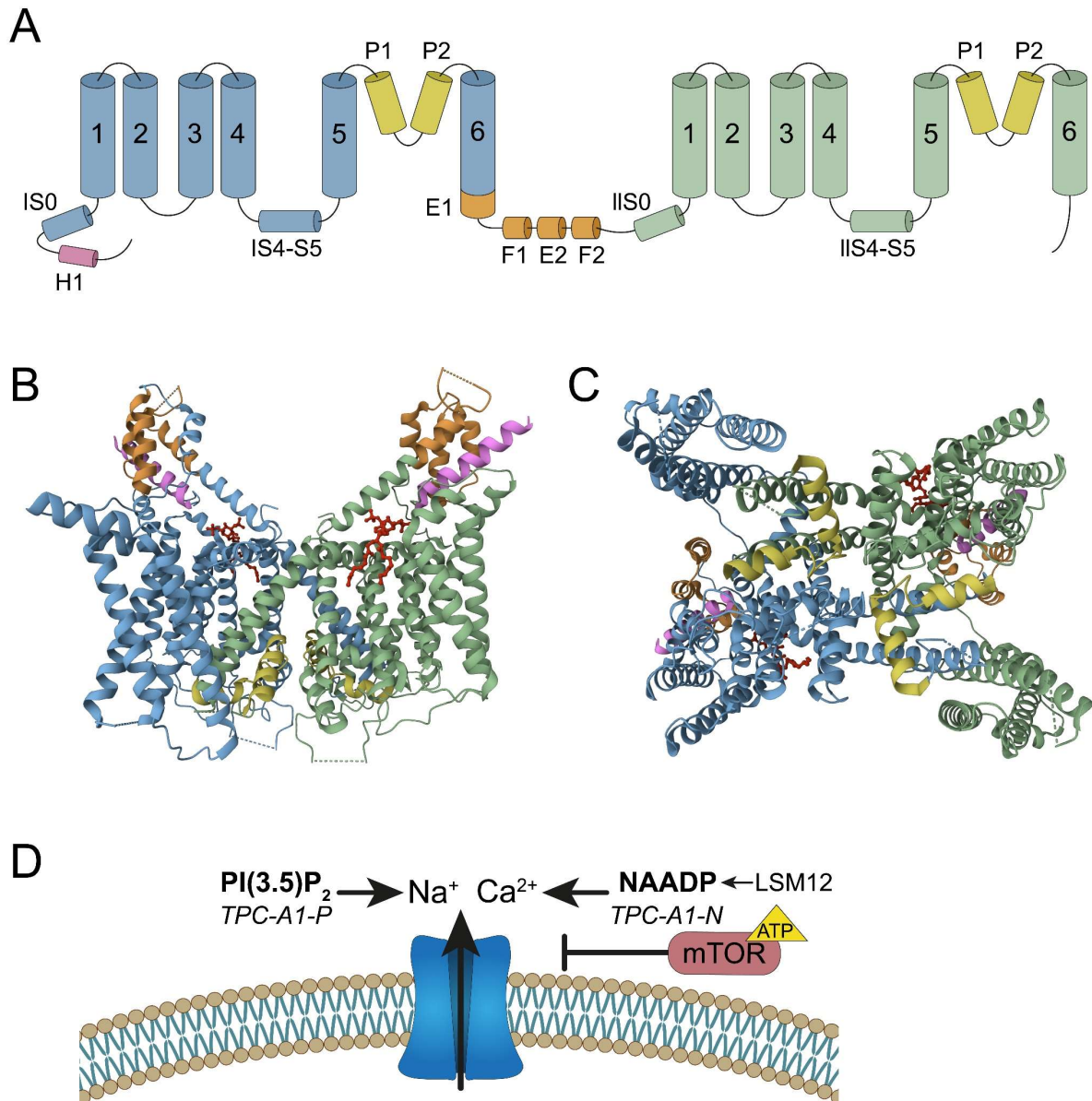


Figure 7: Topology and 3D-protein-structure of the TPC2 channel **A**, The schematic topology of one TPC2 monomer is displayed. The N-terminal Helix domain is shown in pink. The first segment is displayed in blue. A cytosolic helix structure (IS0) is connected to the first of the six transmembrane domains from the first segment (1-6). A second cytosolic helix structure in segment 1 is formed between the transmembrane domains 4 and 5 (IS4-S5). Two EF motifs form the connection between the first and second segment, displayed in orange. The second segment is shown in green. Similar to segment 1, cytosolic helix structures are formed before the first transmembrane domain (IIS0) and between the transmembrane domains 4 and 5 (IIS4-S5). The lumen facing pore-forming region consists of S5, the pore loop, and S6. The pore loop contains two additional helix structures in both segments (IP1,2 and IIP1,2), which are displayed in yellow. **B**, Lateral view on the Cryo-EM structure of the holoprotein hstPC2 (PDB ID: 6NQ1)⁶⁷. Color coding of TPC2 domains correspond to A. The protein assembles as a homodimer and binds two PI(3,5)P molecules on each monomer, shown in red. **C**, View on the hstPC2 pore domain from the luminal side⁶⁷. Color coding as in A. PI(3,5)P ligands are shown in red. The pore domain is formed by eight helical structures, four from each monomer (IP1-2 and IIP1-2). **D**, Mechanisms of the TPC2 channel: The two main ligands are displayed in bold (PI(3,5)P₂ and NAADP). Their synthetic counterparts are shown in italics (TPC-A1-N, TPC-A1-P). ATP bound mTOR is displayed on the Ca²⁺ side bound to ATP, as well as the NAADP binding protein LSM12.

2.5 The role of Rab GTPases for endosome maturation

Rab GTPases are soluble, small proteins that bind Guanosine-diphosphate (GDP) or Guanosine-triphosphate (GTP)⁶⁸. They contain a prenylated C-terminus, specifically a geranylgeranyl anchor by which they insert into the outer leaflet of vesicular membranes (Figure 8 A).

After translation, the GDP-bound Rab-protein is escorted by a Rab escort protein (REP) to a geranylgeranyl-transferase (GGT) for posttranslational modification, which adds the prenyl anchor to the protein^{69,70}. Further, the geranylgeranylated protein then binds to a Guanosine dissociation inhibitor (GDI)^{69,71}. In this state, the Rab-protein is considered inactive, characterized by bound GDP and the association of a GDI, which binds the Rab-protein in the cytosol and covers the lipid anchor, thereby preventing the binding of the lipid anchor to membranes. Activation of the Rab-GTPase is initiated by the GDI displacement factor (GDF) which induces the dissociation of the GDI. Subsequently the exchange of GDP by GTP is triggered by a Guanine nucleotide exchange factor (GEF)⁷². The active state of most Rab GTPases is characterized by three properties: Bound GTP, a free geranylgeranyl anchor, and the integration of this anchor into a target endosomal membrane, which enables the interaction with effector proteins at the target membrane. The conversion back to the inactive state is facilitated by GTP hydrolysis. The GTP hydrolysis is driven by the intrinsic Rab GTPase activity and also catalyzed by a GTPase activating protein (GAP). The activation cycles of Rab-proteins make them excellent regulators⁷³. Activation and inactivation cycles are tightly managed by accessory proteins: Maturing endosomes exchange Rab5 with Rab7 in a process that is commonly named Rab-switch, which involves numerous proteins⁷⁴⁻⁷⁶. Numerous Rab GTPases occur in higher eukaryotes, each having a specific protein activation cycle that, in collaboration with other proteins, target the Rabs to specific vesicles, which makes them suitable markers for different vesicle types (Figure 9 B). The specific mechanism of the membrane targeting is not fully understood, but proposed to be facilitated by either GDF⁷⁷, GDI^{78,79} or GEF^{80,81} proteins.

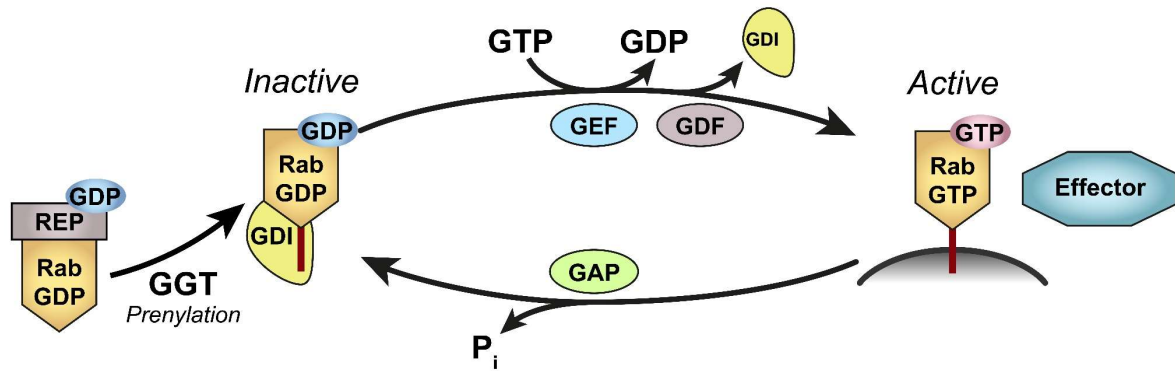


Figure 8: The Rab GTPase system. The activation cycle of Rab-GTPases is displayed schematically: After translation, The Rab-GTPase is escorted via a Rab escort protein (REP). In this state, the Rab-protein is GDP (Guanosine di-phosphate) bound and inactive. The guanine exchange factor (GEF) exchanges the GDP with GTP. The GDI dissociates through a GDI displacement factor (GDF). In this state, most Rab-proteins are considered active and reside at a target membrane to interact with effector proteins. The Rab-GTPase is inactivated by GTP-hydrolysis through intrinsic catalytic activity and a GTPase activating protein (GAP). Consequently, the GDP bound Rab-protein binds with the Guanosine dissociation inhibitor (GDI) and re-localizes to the cytosol.

Rab5 and TPC1 are mostly located at early endosomes, as shown in Figure 9 B. Rab5, by attracting effector proteins to early endosomes, facilitates the early endosomal maturation process^{75,82}. In early endosomes, Rab5 could interact with TPC1, given that both proteins are localized in this compartment. This question will be investigated in my thesis. Conversely, Rab7 and TPC2 mainly associate with late endosomes, also depicted in Figure 9 B. Here, Rab7 facilitates late endosomal fusion with early lysosomes and vesicle trafficking by recruiting and interacting with effector proteins^{75,82}. One potential interaction partner of rab7 could be TPC2⁷³. This hypothesis will also be tested in the present thesis.

Notably, the localization of Rab5 and Rab7 is not limited to early and late endosomes, respectively. Further, TPC1 and TPC2 expression potentially overlap in maturing vesicles as well. Thus, an interaction between Rab5 and TPC2, as well as between Rab7 and TPC1 are possible as well and will be tested in this thesis too.

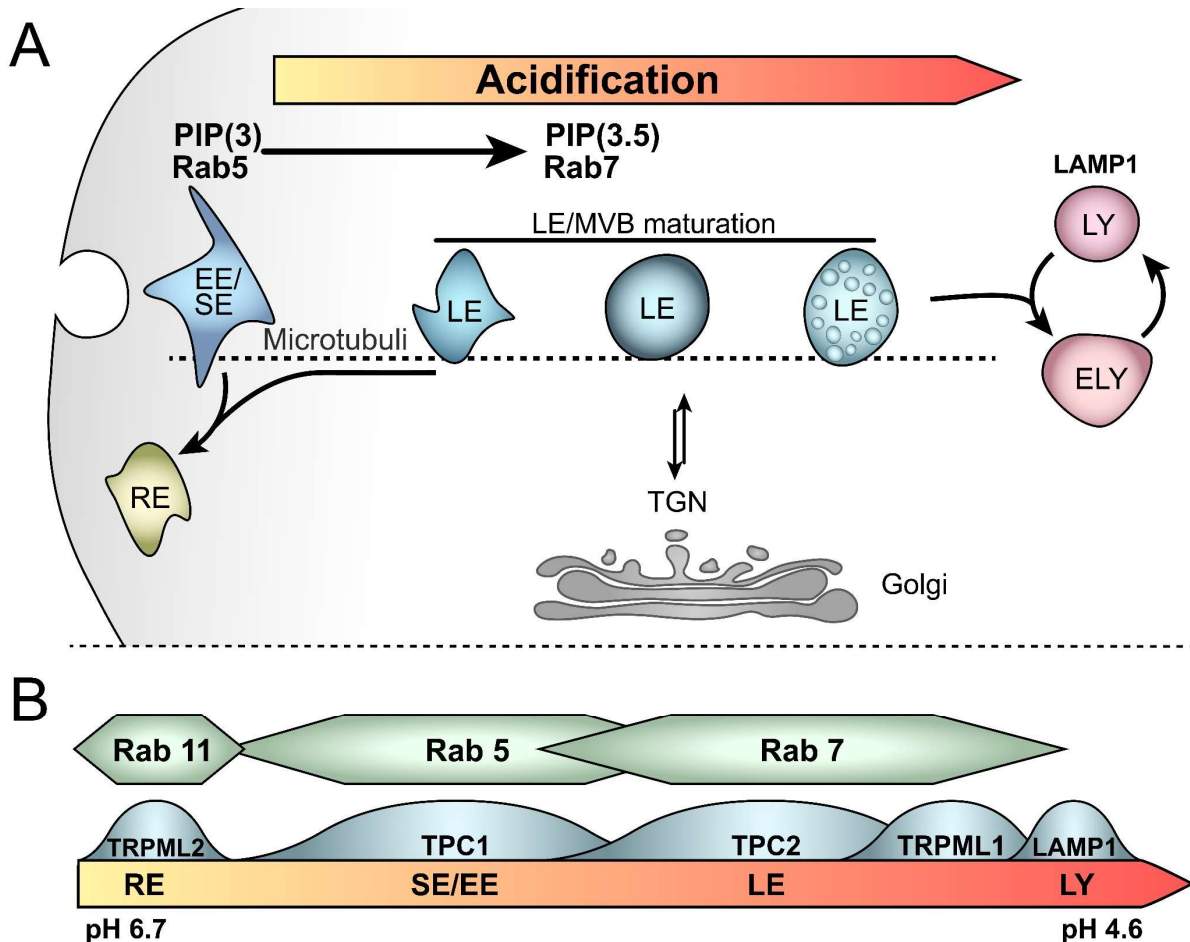


Figure 9: The endolysosomal system. A, The trafficking and maturation of intracellular vesicles after endocytosis is depicted: Early endosomes and sorting endosomes (EE and SE) are formed by accumulating cargo carrying vesicles from invaginations of the cellular membrane. The fate of the cargo is then (or in some cases later) decided for either recycling to the cellular membrane via recycling endosomes (RE), or for degradation. The latter process involves maturation from EEs into late endosomes and multivesicular bodies (LEs/MVBs). In the process of maturation, vesicles undergo several changes: Rab5 is exchanged for Rab7, while PIP(3) is phosphorylated to PIP(3.5)P₂. Further, an acidification process takes place accompanied by a change in the ionic composition within the maturing vesicle. Intraluminal hydrolases accumulate and lysosomal membrane proteins are exchanged. During the maturation process, LEs are transported in perinuclear direction via saltatory movement along microtubuli (MT). LEs are lastly converted into endolysosomes (ELY), resembling an intermediate vesicle type which reversibly becomes a lysosome (LY). In the whole process, proteins and lipids are exchanged with the trans-golgi network (TGN). **B,** Endosomal localization of Rab-GTPases and vesicular ion channels: RE: Recycling endosome. SE/EE: Sorting endosome, early endosome. LE: Late endosome. LY: Lysosome. Rab GTPases that localize on vesicular membranes are shown above in green hexagons. Ion channels that reside at endosomal membranes of specific vesicles are shown below in blue. The acidification during endosome maturation is highlighted on the bottom. Rab11 is localized at recycling endosomes. TRPML2 too, but also at LEs and LY (not shown). Rab5 and TPC1 at early endosomes, Rab7 and TPC2 predominantly at late endosomes. LAMP1 is predominantly present at lysosomes, TRPML1 is found on early lysosomes and late endosomes as well.

3 Aim of the study

This thesis is divided into two interconnected parts: Part I outlines methodological and technical advancements to the Two-Hybrid FRET assay, while Part II focuses on its application on putative protein-protein interactions. The first aim in Part I is to improve the Two-Hybrid FRET assay on the established photometry setup¹ by employing a new FRET pair, developing new FRET calibration standards and improving the fitting procedure. In aim 2, a flow cytometer based Two-Hybrid FRET assay^{1,29} should be established, which allows for high-throughput FRET screenings. In aim 3 a novel, image-based Two-Hybrid FRET assay should be developed on a wide-field plate-reader microscope. This technique will rely on fluorescence images instead of raw fluorescence data and is designed to improve the accuracy compared to flow cytometer assays, while maintaining a high-throughput workflow. The final aim of part I (aim 4) is to establish the image-based Two-Hybrid FRET approach on a confocal microscope. This approach aims to generate binding curves from subcellular regions of interest. The confocal Two-Hybrid FRET method is further refined to transform fluorescence images into color-coded 2D FRET maps, allowing for a spatial analysis of FRET signals within confocal images. All developments made in part I are validated by using the well-known protein-protein interaction between the IQ6-domain of myosinVa and CaM.

Part II focuses on the application of these FRET assays to investigate interactions between proteins of interest: In aim 5, the IQ6 motif is mutated at critical positions to lower the binding affinity to CaM. The WT and mutated IQ6 motifs should serve as high-affinity and low-affinity interaction standards with CaM to assess the reliability of determining binding affinity parameters when using the novel image-based FRET assay. In aim 6 interactions between endolysosomal ion channels, especially Two-Pore channels, and small regulatory proteins (Rab-GTPases) are investigated in micro-domains of the endolysosomal system. The basis of these experiments are two large interactome studies of ion channels in the endolysosomal system^{83,84}. Experiments will be performed on the confocal microscope to resolve and analyze subcellular FRET signals. Rab7 is of special interest and will be investigated using two additional mutants: The constitutively active Rab7 [Q67L]⁸⁵ mutant is locked in the GTP-bound state and lacks the intrinsic GTPase activity. The Rab7 [T22N]⁸⁵ mutant is locked in the GDP-bound state⁸⁵ and considered to be constitutively inactive. The interaction of Rab7 and additional ion-channels that belong to the TRPML-family will be investigated as well.

4 Methods

4.1 Generation of plasmids for Two-Hybrid FRET assays

A plasmid database was generated by cloning 109 constructs containing different calibration constructs (Table S1). All plasmids were cloned via classical restriction-ligation cloning. Additionally, overlap extension PCR and site-directed mutagenesis techniques were employed for several plasmid designs. Primer and restriction sites for constructs described in detail are displayed in Table S2. The database was generated using SnapGene and contains FRET constructs for other proteins and further calibration plasmids that are not addressed here. All calibration constructs and both the wildtype and mutated reference protein-protein constructs used here are available via AddGene (ID: 198192 and ID's: 198196-198202)

4.2 Restriction-Ligation cloning and mutagenesis

A Taq DNA polymerase and a PCR master-mix was used for generating amplicons for molecular cloning (Merck, Cat#12140314001). The PCR cycle is displayed in Table 3. Primers were chosen to have an annealing temperature between 58-62°C. Overlap extension PCRs were conducted using the same Taq polymerase and 100 ng of each parental DNA strand. PCR products are purified through 1 % Agarose Gel electrophoresis in TAE buffer. Fragments smaller than 300 bp were loaded on 2 % Agarose gels. Amplicons and plasmids were digested with restriction enzymes from (ThermoFisher, Cat#K1991) for 10-35 min. at 37°C, depending on the enzymes used. Digested amplicons and linearized vectors were loaded on 1 % Agarose gels in TAE buffer. Gel runs were conducted at 120 V for 25 min. For cloning, DNA bands were cut, solubilized and the DNA purified using a Gel extraction KIT (Macherey-Nagel, Ref#740609.50). Vector and insert concentration were determined through DNA quantification gel electrophoresis assay. Ligation was performed with a T4 DNA ligase (ThermoFisher, Cat#15224041) at room temperature for 1 hour. Site-directed mutagenesis was achieved by using a PfuTurbo polymerase and 100 ng of parental DNA. Parental DNA was destroyed by DpnI digest at 37° for 30 min. (Agilent, Cat#200518). Cloned or mutagenized plasmids were transformed into DH5α chemical competent *E. coli* through heat-shock at 42°C for 60 seconds

and subsequent incubation in SOC medium (ThermoFisher, Cat#15544034) at 37°C for 45 min. Bacteria were plated on Agar plates with either 100 µg/ml ampicillin or 50 µg/ml kanamycin, depending on the vector resistance.

Template DNA	100 ng
Primer 1	10 µM
Primer 2	10 µM
Taq DNA Polymerase	5 U
PCR Master Mix	1X
DMSO	2 %
H2O	Add to 50 µl vol.

Table 2: PCR components

Initial Denaturation	94°C	30 seconds
30 Cycles	94°C	20 seconds
	55°C	2 min
	68°C	1 min / kb
Hold	4°C	/

Table 3: PCR cycling conditions

4.3 Cell culture for Two-Hybrid FRET assays

Seeding, splitting and transfection of cells were performed identical regardless of the instrument used for Two-Hybrid FRET assays.

HEK293T cells were cultured in DMEM high glucose (ThermoFisher, Cat#41965039). 1×10^5 cells were seeded in 6 Well Plates (Thermo Fisher Scientific, Cat#140675). Cells were transfected with FRET constructs on the next day using Lipofectamine 2000 (ThermoFisher, Cat#11668030). 1 µg DNA was used for each calibration construct (spectral correction samples and FRET dimers). For Two-Hybrid FRET assays, multiple stoichiometries of the test interaction were transfected at varying ratios (up to 2 µg:0.5 µg DNA for donor:acceptor and vice versa).

For image-based Two-Hybrid FRET assays, both partners were transfected with equal amounts of DNA (1 μg DNA of each sample plasmid) only. The transfected amounts of DNA for subcellular expressed proteins had to be adjusted by trying out different stoichiometries and transfected DNA amounts ranging from 100 ng up to 2 μg DNA until both partners are equally expressed. Transfected cells were seeded one day after transfection on optical-grade glass bottom imaging dishes (Ibidi, Cat#81158) or well plates (Cellvis, Cat#P06-1.5H-N) that contain a glass bottom with a thickness of 1.5H (170 μm) or lower. The glass bottom was treated with 0.01 % PLL solution for 1 hour beforehand. Flow cytometer Two-Hybrid FRET assays were conducted immediately by splitting cells into PBS instead of transferring cells on imaging dishes. For all other assays, cells are left overnight to adhere to the imaging dish. The growth medium was replaced with Tyrode's solution 30 minutes before measurement. For vesicular expressed proteins, cells were treated with 1 μM apilimod 16 h before measurement.

Reagent	Final concentration
NaCl	140 mM
KCl	5 mM
CaCl ₂	2 mM
MgCl ₂	1 mM
HEPES	10 mM
D-Glucose)	10 mM
ddH ₂ O	n/a

Table 4: Tyrode Imaging-solution. Stored at 4° for up to 6 months

4.4 Two-Hybrid FRET assay on a photometry setup

The hardware used and methodic details are described here, while data-related content is displayed in the results. The hardware used is similar to the HORIBA photometry setup used in previous publications¹. A Leica DMI-8 setup was used, equipped with a photometry setup from Horiba (model no. D-104 B, 914, R1527). A short arc Xenon lamp (Ushio, no. UXL-75XE) and a collimator were installed for illumination. A 40X Oil Objective (1.3 NA, Olympus) was used. The FelixGX software and DeltaRamX (Horiba) was used to record fluorescence signal

traces. The PMT voltage was set to 750 V and the dark current of the PMT was subtracted from all measurements. A time-based acquisition protocol was created to screen the dish for fluorescent cells in the CFP channel. The excitation wavelength for the screening protocol was 436 nm for 600 second at a sampling rate of 10 points per second using the CFP cube. To measure fluorescence signals (S_{CFP} , S_{FRET} , S_{YFP}) from a fluorescent cell, an acquisition macro was created: The CFP and FRET signals were acquired using a 436 nm excitation wavelength. The CFP signal was acquired by using the CFP filter cube, 3 seconds of illumination and recording by the PMT. The FRET signal was acquired by using the FRET cube, 3 seconds of illumination and recording by the PMT. The YFP signal was acquired by using a 512 nm excitation wavelength and the FRET cube for 3 seconds and recording by the PMT. The macro was recording the three signals in this order. The pinhole of the photometer was adjusted to the size of a cell and not changed throughout the experiment. Fluorescent cells were focused using bright field illumination and measured once in each channel as described. Multiple cells were measured for each calibration sample and protein interaction sample. Fluorescence signal traces which contain data from each channel used were exported as .txt files. Each .txt file contained three fluorescence signal traces corresponding to the emission signals measured (S_{CFP} , S_{FRET} , S_{YFP}). A custom Octave script was used to convert fluorescence signal traces into average fluorescence values: Fluorescence signal traces are saved in FelixGX as tabulated signals over time, the script converts the raw data tables into .txt file data tables. The first and last 0.5 seconds of each trace were excluded to minimize artifacts that arise during the start due to the shutter opening and photo-bleaching artefacts during the end of each trace. Using the Octave script, a new .txt file was created containing the averaged signals as data triplets (S_{CFP} , S_{FRET} , S_{YFP}). All data triplets from one sample (background, spectral correction, dimer, or protein interaction) were pasted in columns into an empty excel sheet. Excel sheets containing all data table from specific samples were uploaded in the Matlab FRET analysis script (Figure 11) for FRET evaluation.

4.5 Two-Hybrid FRET assay on a flow cytometer

The hardware used and methodic details are described here, while data-related content is displayed in the results. A BD FACS Calibur was used for measurements. Similar devices were used previously by others²⁹. Cells are vortexed for up to one second in a FACS tube before measurement. Three emission channels were set: The CFP channel was measured using the 405 nm excitation laser and the PacificBlue (450/50 band-pass) emission filter. The FRET channel was measured simultaneously with the same excitation laser but in the AmCyan (510/50 band-pass) emission filter. The FRET channel was measured using the 488 nm excitation laser and the FITC (530/30 band-pass) emission filter. At least 5.000 cells were measured for each calibration sample. At least 50.000 cells were measured for each protein interaction sample. The measurement count was limited to fluorescent cells in specific gates: The FSC (forward scatter) and SSC (side scatter) were adjusted by measuring un-transfected cells and adjusting their corresponding PMT to visualize all cells in a scatter plot. The FSC/SSC gate was applied to isolate the HEK293t single-cell population while excluding other groups. Three additional fluorescence-gates for each emission filter (PacificBlue, AmCyan and FITC) were created to limit the counting to fluorescent cells. Subsequently, each sample was measured separately (background, spectral correction, dimers, protein interaction). The fluorescence-gates were removed for the background measurement. The acquired data were exported in .FSC 3.0 format. The .FSC files were converted into .ffa files using the custom MatLab script "Filter_FACS". All measurements in the .FSC 3.0 file were gated (FSC-H/SSC-H, FSC-A/SSC-H and SSC-A/SSC-H) to exclude cell duplets and debris during conversion to .ffa files. The .ffa files were uploaded in the Matlab FRET analysis script described in Figure 11 for FRET evaluation.

4.6 Image-based Two-Hybrid FRET measurements on a wide-field optical plate reader

The hardware used and methodic details are described here, while data-related content is displayed in the results. A BioTek Cytation5 optical plate-reader from Agilent (Figure 14 A) was used for all measurements. Filter cubes were installed as shown in Figure 14 B and C. The Gen5

imaging software was utilized to operate the instrument. Methodological details are described further in the corresponding publication⁸⁶.

An optical-grade well plate or imaging dishes were mounted into the sample carrier of the instrument with cells transfected with the protein interaction sample. A 20X air objective was selected. Three fluorescence channels were set up, each using one of the three filter cubes in the following order: CFP, FRET, YFP. After insertion of the sample carrier, the CFP channel was used to focus cells in any of the wells or imaging dishes of the sample carrier manually. The Z-plane offset was saved and set as the focus-standard for all measurements throughout one session. An image of the focused cells in all three channels was acquired while setting the digital gain to zero. Emission intensities were compared, and the illumination power adjusted to equalize emission signals in all channels, covering the histograms to a minimum of 40 %. The integration time was set to 50 ms for the CFP channel, 30 ms for the FRET channel, and 20 ms for the YFP channel. After the acquisition settings were optimized to the protein interaction sample, the acquisition protocol was created using the Z-plane offset and illumination powers determined before. The acquisition protocol was designed to take tile-stacks (3x3) for each well or imaging dish that is mounted using all three channels subsequently. After running the protocol, the remaining calibration samples or further protein interaction samples were measured using the same protocol. Images acquired are saved as .tif files during the acquisition protocol in the acquisition folder. After the acquisition process, saved images were reorganized and labeled according to their corresponding sample and channel they were acquired in, for example: Dimer_D3_CFP.tif, Dimer_D3_FRET.tif, Dimer_D3_YFP.tif are the images acquired of the D3 dimer in one imaging dish in the CFP channel (first image), FRET channel (second image) and YFP channel (third image).

4.7 Setup of automatic cell detection from wide-field images

For automatic cell detection, the deep-learning software Ilastik⁸⁷ was utilized (Figure 15 - 16).

Before starting the cell detection training process, a new folder was created and labeled "Training". This folder is required and will later contain all files from the pixel- and object-classifiers, as well as the image used for the automatic cell detection training. First, the CFP-

channel D3 (FRET calibration dimer sample) image is copied from the acquisition folder and pasted into the “Training” folder. Then Ilastik is started, and the pixel classification option selected. The D3 image in the CFP channel from the “Training” folder is then opened in the pixel classifier. Two classes are displayed by default and renamed as follows: The first class was labeled “Cell” and the color set to yellow; the second class was labeled “Background” and the color set to blue as shown in Figure 16 A. After selecting the first class (“Cells”), lines were drawn across cells in the image exemplary. After selecting the second class (“Background”), lines were drawn in regions without cells. The prediction was updated by applying the live update option. Additional lines were drawn until the prediction of the automatic image segmentation in cells and background was adequate. The segmentation prediction file is labeled prediction.h5. This file is exported into the “Training” folder by pressing the “export” button. Additionally, the pixel classification project file is labeled pixel_classifier.ilp and saved into the “Training” folder by pressing the “Save as” button as well. Up to this step, the “Training” folder contains the CFP-channel image of D3, the pixel_prediction.h5 file and the pixel_classifier.ilp file. The pixel classification window is then closed. In Ilastik, the object classification option is then selected. By pressing the “import” button, the CFP-channel image of D3 from the Training folder is loaded in the object classification window. Additionally, the pixel_prediction.h5 file is loaded similarly. The segmented image is now shown in the object classification window (Figure 16 B). Two classes are displayed by default and renamed as follows: The first class was labeled “good” and the color set to green. This class defines representative cell shapes. The second class was labeled “bad” and the color set to red. This class defines artifacts and cell aggregates that form non-representative shapes. After selecting the first class (“good”), multiple representative cell shapes in the image were clicked on. They are then determined as “good” cells and displayed in green. Similarly, after selecting the second class (“bad”), shapes that represent cell clusters or artefacts are clicked on. They are determined “bad” and displayed in red. After clicking on the live update option, all cells in the image are automatically sorted in “good” and “bad”, displayed in faint green and red coloring, respectively. Additional annotations were done until the prediction was adequate. The object classification project (object_classifier.ilp) is then saved into the “Training” folder by clicking on the “Save as” button. After this, the “Training” folder contains all required files for the automatic cell detection of all images that are evaluated for the wide-field image-based Two-Hybrid FRET assay.

4.8 Wide-field image conversion into data tables using automatic cell detection

Ilastik is used as described in 3.7 to generate ROIs within wide-field images. ImageJ is now used to convert ROIs into fluorescence data tables, by using the previously generated Ilastik files (Figure 16 B).

ImageJ was started and the ImageJ macro “segmentation_wf” opened. The CFP, FRET and YFP image of one calibration sample or protein interaction sample is uploaded in the respective dialogue windows of the macro. Subsequently, the pixel_classifier.ilp and object_classifier.ilp from the “Training” folder are uploaded similarly in their respective dialogue windows. After these five uploads, the macro was started and the automatic cell detection process is active. Fluorescence data tables, displaying the averaged fluorescence intensity signals from all three channels (S_{CFP} , S_{FRET} , S_{YFP}) for each detected cell, are created the completion of the macro. These data tables are saved as .csv files and used for Two-Hybrid FRET evaluation in the Matlab script.

4.9 Image-based Two-Hybrid FRET measurements on a confocal microscope

The hardware used and methodic details are described here, while data-related content is displayed in the results. In addition, details concerning this method are described further in the corresponding publication⁸⁶.

For the confocal image-based Two-Hybrid FRET measurement, four different instruments were used in a similar fashion: An upright Zeiss Airyscan (LSM980), an inverted Zeiss Airyscan (LSM980, Figure 18 A), an inverted Leica SP8, and an inverted Leica Stellaris.

Three channels (CFP, FRET, YFP) were set up according to Figure 18 B and C. These settings refer to the Zeiss LSM980 confocal microscope used. The pinhole was set to 1 AU (airy unit). Acquisition properties were chosen to optimize fluorescence quantification: Averaging was set to 4X between line scans. Channel properties: CFP: 445 nm excitation laser, 445-526 nm detection range. FRET: 445 nm excitation laser, 526-561 nm detection range. YFP: 514 nm excitation laser, 526-561 nm detection range. The CFP and FRET channel were measured simultaneously, the YFP channel was subsequently after the CFP and FRET line scan. Excitation power was adjusted to the brightness of the protein interaction samples. PMT voltage was

between 650 and 750 V but was not changed in-between a session. A 63X objective with a 1.3 NA was used for all measurements. The image resolution was adjusted based on the Nyquist criterion in the acquisition software.

Leica instrument properties differed in following aspects: A 40X objective with a 1.3 NA was used. Line averaging was set to 3X. HyD detectors were set to a gain value of 50 (au), PMT detectors to 700 V. Channel properties: CFP: 458 nm excitation laser, 462-493 nm detection range. FRET: 458 nm excitation laser, 524-548 nm detection range. YFP: 514 nm excitation laser, 524-548 nm detection range. Later, these properties were further changed by altering emission detection ranges in all channels. The following steps were identical for all instruments used: An imaging dish was mounted, and the Z-position was adjusted using bright field illumination through oculars. After setting up or changing the acquisition protocol, fluorescent cells were screened using the CFP channel in a live mode (fast acquisition time without capturing images). Once a field of view was selected for imaging, the acquisition protocol was started to acquire multi-stack images (i_{CFP} , i_{FRET} , i_{YFP}). At least five images of the same field of view were captured. Fluorescence intensities between these images in identical regions and histograms were compared to rule out photo-bleaching effects resulting caused by the excitation light. Subsequently, the acquisition protocol was used throughout a measurement session for all calibration samples (background, spectral correction samples and dimers) and all protein interaction samples. A different field of view was selected and captured using the acquisition protocol for each measurement. This step was repeated at least 5 times for calibration samples and at least 15 times for protein interaction samples. Images were labeled corresponding to the type of sample they belong to and exported in their native image format (.czi for Zeiss instruments, .lif for Leica instruments).

4.10 Confocal multi-stack image conversion into fluorescence data tables

The workflow is depicted in Figure 19. Each calibration (dimers and single-fluorophores) and protein interaction sample (e.g. myosinVa IQ6 + CaM) was transformed consecutively: The image (.czi or .lif) was opened in ImageJ. The "FRET_PIX" ImageJ macro was opened if a calibration sample image was to be evaluated. Otherwise, for protein interaction sample images, the "FRET_ROI" ImageJ macro was opened. After opening one of these two macros,

ROIs are drawn as follows: At least 3 ROIs were drawn in cytosolic regions from two different cells for each dimer spectral correction sample image. A minimum of 5 ROIs were drawn in cytosolic regions from three different cells for each dimer sample image. A minimum of 20 ROIs in multiple cells (1-3 ROIs per cell) were drawn in images of a protein interaction sample image. After defining a minimum of 20 ROIs in the image, the FRET_PIX or FRET_ROI macro was started by pressing “OK”. The FRET_PIX macro generated a fluorescence data table consisting of fluorescence data (S_{CFP} , S_{FRET} , S_{YFP}) in each pixel within the drawn ROIs of the image. The FRET_ROI macro generated a fluorescence data table consisting of averaged fluorescence data from all pixels within each ROI of the image. These data tables were saved as .csv files and labeled corresponding to their calibration sample or protein interaction sample for evaluation in the Two-Hybrid FRET analysis Matlab script.

4.11 Two-Hybrid FRET data analysis

A custom Matlab script was used to calculate calibration parameters and binding curves. The user interface is displayed in Figure 11. The calculation process is described in the Two-Hybrid FRET calculation section. Data tables were imported in .csv, .xls or .ffa format. Fluorescence signals below 1% of the detector range and above the saturation limit were filtered out. The maximum imbalance of N_A/N_D and N_D/N_A was set to 5. All binding curves were calculated using a simultaneous iterative fitting procedure of the E_A and E_D curves to find a combined least error-fit (Matlab function: nlinfit). Binding curve parameters and diagrams were exported into excel and visualized using GraphPad Prism.

4.12 Confocal image processing

Multi-stack images (i_{CFP} , i_{FRET} , i_{YFP}) were exported in native format (.czi or .lif) and loaded into ImageJ. Images were then saved as .tif files and each channel opened individually in GIMP. Images were converted into RGB colors and colorized in either red (255, 0, 0) or green (0, 255, 0). Composite images were created by summation of RGB colors from both images. A linear brightness adjustment was applied to images to equalize the perceived brightness of overlay images.

4.13 2D mapping of FRET efficiencies (E_A and E_D)

Images were loaded into ImageJ. The custom “lsm_FRET_calc_alpha2” macro was started. Calibration parameters corresponding to the measurement session of the image under investigation (Background, R_{A1} , R_{D1} , F_{ratio} and G_{ratio}) were adjusted in the source code of the macro. Similarly, the minimum and maximum thresholds for background and oversaturated pixels were set. The alpha blending minimum value (“fluo_alpha_min”) was set to 0.1, the maximum value to 0.4. The background for the alpha-blending (increasing transparency of regions with low brightness) is set to be black. A Gaussian blur (0.3 pixel radius) was applied to the input image and additionally to the heatmaps (1 pixel radius). FRET efficiencies were displayed using the “physics” LUT (look up table) from ImageJ, ranging from 0 % to 40 % FRET for both E_A and E_D .

4.14 Mathematical background of FRET

As shown in Figure 1 B, FRET occurs when an excited donor transfers energy to an acceptor to return to the ground state. The FRET efficiency can be described as the fractional amount of energy that is released via FRET compared to all de-excitation pathways. k_T describes the FRET related donor de-excitation, k_r the radiative decay and k_{nr} the nonradiative relaxation. Thus, the FRET efficiency (E) is denoted as a relative quantity in percentage.

$$E = \frac{k_T}{k_r + k_{nr} + k_T} \quad (1)$$

E depends on the distance, overlap integral and orientation factor of the FRET partners. The conditions for FRET to occur are described in the following equations.

$$E = \frac{1}{\left(1 + r/R_0\right)^6} \quad (2)$$

R_0 is the Förster distance. It represents the distance at which the E is 50 %. Note that R_0 appears in the denominator to the sixth power in equation (2), thus having great influence on the FRET efficiency.

$$R_0^6 = \frac{20.7}{128\pi^5 N_A} * \frac{\kappa^2 Q_D}{n^4} * J \quad (3)$$

R_0^6 depends on the orientation factor (κ) of both dipoles (or fluorophores), quantum yield of the donor (Q_D), refractive index of the medium (n) and the overlap integral of the donor emission spectrum and the acceptor excitation spectrum (J). N_A : Avogadro constant.

$$J = \int \overline{f_D}(\lambda) \epsilon_A(\lambda) \lambda^4 d\lambda \quad (4)$$

J is the overlap integral of donor emission and acceptor excitation spectra. $\overline{f_D}$ is the donor emission spectrum normalized to 1 and ϵ_A the acceptors extinction coefficient.

$$\kappa = \hat{\mu}_A * \hat{\mu}_D - 3(\hat{\mu}_D * \hat{R})(\hat{\mu}_A * \hat{R}) \quad (5)$$

κ describes the orientation between donor and acceptor. However, for fluorophores that are free moving (i.e. bound to a flexible linker or free in solution), κ is approximately 0.66. For Two-Hybrid FRET assays with genetically encoded fluorophores, this will be assumed.

4.15 Mathematical background of Two-Hybrid FRET binding curves

Before binding curves can be determined, two distinct steps are required: The spectral correction and FRET calibration. The spectral correction serves to dissect fluorescence signals acquired in the CFP, FRET and YFP channels (S_{CFP} , S_{FRET} , S_{YFP}) into pure fluorescence components from donor direct excitation and emission, sensitized emission of the acceptor due to FRET and acceptor direct excitation and emission: CFP_{direct} , YFP_{FRET} , YFP_{direct} (Figure 3 D). This is done by quantifying the spectral crosstalk of the donor and acceptor in all channels with the three spectral correction factors R_{A1} , R_{D1} , R_{D2} . The FRET calibration allows the determination of absolute FRET efficiencies derived from donor quenching (E_D) and sensitized emission (E_A) via the G_{ratio} and F_{ratio} , corresponding to the relative extinction properties between donor and acceptor (G_{ratio}) and relative emission properties between donor and acceptor (F_{ratio})

Spectral correction factors (R_{A1} , R_{D1} , R_{D2}): Three FRET channels (CFP, FRET, YFP) are used to obtain the measured emission signals S_{CFP} , S_{FRET} and S_{YFP} , respectively. These measured signals (S_{CFP} , S_{FRET} and S_{YFP}) contain the emission components CFP_{direct} , YFP_{FRET} , YFP_{direct} , respectively. CFP_{direct} is the emission of the donor upon direct excitation, YFP_{FRET} is the sensitized emission of the acceptor upon donor excitation, and YFP_{direct} is the acceptor emission on direct excitation. However, because the excitation and emission spectra of the donor and acceptor

overlap, S_{CFP} , S_{FRET} and S_{YFP} contain additional emission components that are corrected for using the spectral correction factors: For instance, in a sample containing interacting proteins A (fused to the donor fluorophore) and B (fused to the acceptor fluorophore) that is measured in the FRET channel, three components are in the emission signal S_{FRET} : 1. Emission of the donor that appears when measuring acceptor emission (donor bleed through in the acceptor emission detection range) 2. Emission due to direct excitation of the acceptor when exciting the donor (cross excitation of the acceptor at the donor excitation wavelength), and 3. The desired component YFP_{FRET} , representing FRET related sensitized emission upon donor excitation. The spectral correction factors are required to isolate the YFP_{FRET} signal from the measured signal in the S_{FRET} channel. Additionally, the spectral correction factors correct the S_{CFP} signal obtained in the CFP channel to yield CFP_{direct} and the S_{YFP} signal from the YFP channel to yield YFP_{direct} , respectively.

R_{A1} : A fraction of YFP is cross-excited in the FRET channel from donor excitation light. In a sample containing acceptor fluorophores only, R_{A1} is defined as the ratio of excitation in the FRET channel relative to the YFP channel (6).

$$R_{A1} = \frac{S_{FRET}}{S_{YFP}} \quad (6)$$

R_{D1} : The emission spectra of CFP and YFP overlap, therefore a fraction of CFP emission will be detected in the FRET channel. In a sample containing donor fluorophores only, R_{D1} is defined as the ratio of CFP emission in the FRET channel relative to the CFP channel (7).

$$R_{D1} = \frac{S_{FRET}}{S_{CFP}} \quad (7)$$

R_{D2} : A small fraction of CFP is cross-excited in the YFP channel from acceptor excitation light. In a sample containing donor fluorophores only, R_{D2} is defined as the ratio of excitation in the YFP channel relative to the CFP channel (8).

$$R_{D2} = \frac{S_{YFP}}{S_{CFP}} \quad (8)$$

Using the spectral correction factors, the raw fluorescence data (S_{CFP} , S_{FRET} and S_{YFP}) can be dissected into the three emission quantities in the FRET channel:

$$CFP_{direct} = R_{D1} * S_{CFP} \quad (9)$$

$$YFP_{direct} = R_{A1} * (S_{YFP} - R_{D2} * S_{CFP}) \quad (10)$$

$$YFP_{FRET} = S_{FRET} - R_{A1} * (S_{YFP} - R_{D2} * S_{CFP}) - R_{D1} * S_{CFP} \quad (11)$$

FRET calibration (G_{ratio} and F_{ratio}): For absolute quantification of FRET, two ratios are determined: The $G_{ratio} \left(\frac{g_D}{g_A}\right)$ corresponds to the relative extinction properties of the donor to the acceptor fluorophore. The $F_{ratio} \left(\frac{f_A}{f_D}\right)$ corresponds to the relative emission ratio of the acceptor to that of the donor. Thus, g_x and f_x (x is either donor or acceptor) can be denoted as displayed below.

$$g_x = I_0 * [\varepsilon_{XFP}(\lambda)] \lambda_{min} \leq \lambda \leq \lambda_{max} \quad (12)$$

$$f_x = QY_{XFP} * [f_{XFP}(\lambda)] \lambda_{min} \leq \lambda \leq \lambda_{max} \quad (13)$$

I_0 denotes the the excitation light intensity, $[\varepsilon_{XFP}(\lambda)] \lambda_{min} \leq \lambda \leq \lambda_{max}$ the apparent extinction coefficient at a defined wavelength and $QY_{XFP} * [f_{XFP}(\lambda)] \lambda_{min} \leq \lambda \leq \lambda_{max}$ the emission of a given fluorophore at a defined wavelength. Note that g_x and f_x are unknown and require an absolute calibration of the used instrument by, for example, using fluorescent beads with known excitation and emission properties. However, the relative ratios $G_{ratio} \left(\frac{g_D}{g_A}\right)$ and $F_{ratio} \left(\frac{f_A}{f_D}\right)$ for any fluorophore pair can be determined by measuring dimer constructs in all Two-Hybrid FRET channels:

When measuring in the three Two-Hybrid FRET channels and correcting the signals for spectral crosstalk by using the previously acquired spectral correction factors, three fundamental emission quantities can be obtained:

$$CFP_{direct} = N_D * g_D * f_D * (1 - E_D) \quad (14)$$

$$YFP_{FRET} = N_D * g_D * f_A * E_A \quad (15)$$

$$YFP_{direct} = N_D * g_A * f_A \quad (16)$$

The $G_{ratio} \left(\frac{g_D}{g_A}\right)$ and $F_{ratio} \left(\frac{f_A}{f_D}\right)$ can now be determined by rearranging these equations.

Equations (15) and (16) yield the absolute FRET efficiency from sensitized emission, by solving for E_A :

$$E_A = \frac{g_A}{g_D} * \frac{YFP_{FRET}}{YFP_{direct}} \quad (17)$$

Equations (14) and (15) yield the absolute FRET efficiency resulting from donor quenching by solving for E_D , if we can assume $N_A E_A = N_D E_D$. This notion is true when dimers are measured.

$$E_D = \frac{YFP_{FRET}}{YFP_{FRET} + \frac{f_A}{f_D} * CFP_{direct}} \quad (18)$$

For mTq2-mVen dimers with a 1:1 stoichiometry, $E_A = E_D$. Thus, the equations (17) and (18) can be rearranged into a linear function. The $G_{ratio} \left(\frac{g_D}{g_A} \right)$ becomes the slope and the $F_{ratio} \left(\frac{f_A}{f_D} \right)$ the y-intercept:

$$\frac{YFP_{FRET}}{CFP_{direct}} = \frac{g_D}{g_A} * \frac{YFP_{direct}}{CFP_{direct}} - \frac{f_A}{f_D} \quad (19)$$

Equation (19) can now be solved for $G_{ratio} \left(\frac{g_D}{g_A} \right)$ and $F_{ratio} \left(\frac{f_A}{f_D} \right)$ by using the dimer constructs (Table 1): Both ratios are determined as outlined in Figure 4 C by plotting dimer data according to the diagram.

Two-Hybrid FRET binding curve generation: With the three corrected emission signals from the spectral correction and the G_{ratio} and F_{ratio} , it is possible to approximate the relative amount of donor and acceptor molecules from the three emission signals (S_{CFP} , S_{FRET} , S_{YFP}). Additionally, the relative bound and unbound fraction of FRET partners can be determined, resulting in the ability to impose a binding model to generate the displayed Two-Hybrid FRET binding curves.

Imposing a binding model requires the knowledge of the concentration of donor- and acceptor molecules.

The relative amount of donor and acceptor molecules are determined as follows. This is possible by assuming $\varepsilon_D * g_D = 1$, as only the relative values for g_A versus g_D and f_A versus f_D (G_{ratio} and F_{ratio}) can be acquired from the previous steps.

$$N_D = \frac{CFP_{direct}}{1 - E_D} \quad (20)$$

$$N_A = \frac{YFP_{direct}}{G_{ratio} * F_{ratio}} \quad (21)$$

A given protein interaction sample consist of a mixture of bound and unbound FRET partners.

The bound fractions (D_b and A_b) are calculated as follows:

$$D_b = \frac{N_D + N_A + K_D - \sqrt{(N_D + N_A + K_D)^2 - 4N_D N_A}}{2N_D} \quad (22)$$

$$A_b = \frac{N_D + N_A + K_D - \sqrt{(N_D + N_A + K_D)^2 - 4N_A N_D}}{2N_A} \quad (23)$$

D_{free} and A_{free} are then determined as:

$$D_{free} = N_D * (1 - D_b) \quad (24)$$

$$A_{free} = N_A * (1 - A_b) \quad (25)$$

The fraction of bound molecules (D_b and A_b) determines the apparent FRET-efficiency as shown:

$$E_A = A_b E_{max} \quad (26)$$

$$E_D = D_b E_{max} \quad (27)$$

The parameters described in equations 24-27 can be integrated into a Langmuir binding model (equation 28) with a few adjustments:

$$\theta = \frac{A * K * [L]}{1 + K * [L]} \quad (28)$$

The θ denotes the fraction of adsorption sites on the surface that are occupied by molecules (which would translate into the bound donor or acceptor protein fraction in case of a protein-protein interaction). A multiplied by K describes the effective equilibrium constant with a scaling factor, when $A < 1$. $[L]$ is the ligand when the equation is applied on a classical Langmuir binding model. The inverse of the equilibrium constant yields the dissociation constant:

$$\theta = \frac{A * \left(\frac{1}{K_D} * [L]\right)}{1 + \left(\frac{1}{K_D} * [L]\right)} \quad (29)$$

Simplifying this results in the final equation that is used:

$$\theta = \frac{A * [L]}{K_D + [L]} \quad (30)$$

Which can be rewritten for Two-Hybrid FRET purposes as follows:

$$\theta = \frac{FRET_{max} * x}{K_D + x} \quad (31)$$

$E_{A,max}$, $E_{D,max}$ and K_D can be evaluated by using multiple measurements and fitting a binding curve plotting E_A or E_D on the y-axis and D_{free} or A_{free} on the x-axis, respectively. Note that the K_D is often described as $K_{D,eff}$, because it is an experimental parameter that differs from the real K_D . This leads to the following equations used for the fitting process:

$$E_A = \frac{E_{A,max} * D_{free}}{(D_{free} + K_D)} \quad (32)$$

$$E_D = \frac{E_{D,max} * A_{free}}{(A_{free} + K_D)} \quad (33)$$

$$\begin{pmatrix} E_A \\ E_D \end{pmatrix} = \begin{pmatrix} \frac{E_{A,max} * D_{free}}{(D_{free} + K_D)} \\ \frac{E_{D,max} * A_{free}}{(A_{free} + K_D)} \end{pmatrix} \quad (34)$$

Equation (33) and (34) are fitted to the experimental data using a nonlinear, iterative least-square fitting algorithm (Matlab function: `nlinfit`), resulting in Two-Hybrid FRET binding curve data as shown in Figure 5 A. The K_D is the half-maximum of the binding curve, $E_{D,max}$ and $E_{A,max}$ are the asymptotic maxima, together referred to as the FRET maximum, or $FRET_{max}$. The matrix (35) is used for fitting E_A and E_D simultaneously when using the custom Matlab software.

5 Results

Part I: Two-Hybrid FRET development

5.1 Aim 1 – Advancements of the Two-Hybrid FRET method

Starting from the established photometry based Two-Hybrid FRET assay in Professor Wahl-Schott's group, I improved the FRET assay by employing a more potent FRET pair, designing and cloning optimized FRET calibration constructs, and working on a software-based, improved fitting procedure.

5.1.1 Employing an optimized fluorophore pair for Two-Hybrid FRET

mTurquoise2 (donor) with mVenus (acceptor) were used as a FRET pair for all experiments displayed in my thesis. This FRET pair has an improved dynamic range due to a 23 % increased Förster distance compared to ECFP/EYFP (equation 3⁸⁸⁻⁹²). In addition, mTurquoise2 has an excellent quantum yield and brightness level compared to similar cyan fluorescent proteins and is further pH resistant at physiological level (pK_a 3.1)⁹². mVenus is one of the most pH resistant yellow fluorophores with a pK_a of 5.5, while also providing a high quantum yield and brightness⁹¹. Thus, mTq2/mVenus was determined as the most optimal combination for live-cell FRET concerning robustness and dynamic range.

As displayed in Figure 2, two spectral correction samples expressing the FRET donor and acceptor individually are required for determining the spectral correction factors R_{A1} , R_{D1} and R_{D2} . Both fluorophores, mTq2 and mVenus, were cloned in individual plasmids, respectively. The excitation and emission range, which determine the crosstalk that is calculated as the spectral correction factors, are very similar between mTq2 and mVenus versus ECFP and EYFP. Thus, the spectral correction was, as expected, similar to data presented previously¹, as briefly shown in Figure 3 C.

5.1.2 Design of novel, improved FRET calibration probes

Three FRET calibration constructs are required for determining the G_{ratio} and the F_{ratio} , as shown in Figure 2 A and Figure 4. Plasmids were cloned corresponding to Figure 10 A using mTq2 as the FRET donor and mVenus as the FRET acceptor fluorophore as a fusion protein, separated by a linker. Three different dimer types were designed: One containing a short linker (high FRET-Efficiency), one containing a long linker (intermediate FRET-efficiency), and one containing a cleavage site within the linker (no FRET). FRET efficiency data using these three dimers are displayed in Figure 10 B. Data points are colored according to the color of their corresponding linker in Figure 10 A: All designed FRET calibration standards yield stable FRET efficiencies for E_A and E_D regardless of dimer concentration (X-axis). Given the 1:1 stoichiometry of both fluorophores in all dimers, E_A and E_D are identical. The D3 dimer results in high and equal ($E_A = E_D$) FRET efficiencies (55 % FRET, orange data). The D42 dimer was designed to have the half-maximum FRET efficiency of D3 (30 % FRET, red data). This dimer consists of an arbitrary, 42 amino acid long sequence (Figure 10 A). The D2A dimer contains a T2A peptide between both fluorophores, causing a translational cleavage, separating both fluorophores. The D2A dimer yields very low and equal ($E_A = E_D$) FRET efficiencies of 0-5 %.

To acquire the FRET calibration standards G_{ratio} and F_{ratio} , the dimers are plotted in a diagram as displayed in Figure 10 C. The diagram contains the data from the three dimers displayed in Figure 10 A and B, using the same coloring corresponding to the linker color in Figure 10 A and data point color in Figure 10 B. The data display large and equal spacing between the dimers along the regression line which leads to a robust and accurate linear fit between this data points. The G_{ratio} is derived from the slope, the F_{ratio} from the Y-axis offset of the regression line. In Figure 10 D, some additional dimers that were designed are displayed schematically: All dimers with a short linker (up to 18 amino acids) resulted in high FRET efficiencies, but slightly lower FRET efficiencies than the D3 dimer (40 – 50 %). A dimer consisting of a 42-amino acid long sequence derived from LAMP1 that mostly forms beta-sheet structures was designed to investigate if this secondary protein structure is beneficial for creating stable FRET signals. This dimer resulted in similar FRET values compared to the D42 dimer (Figure 10 D, Medium FRET construct). The chosen dimer combination of D3, D42 and D2A cover a large range of FRET signals and optimal conditions for the linear regression to derive calibration parameters.

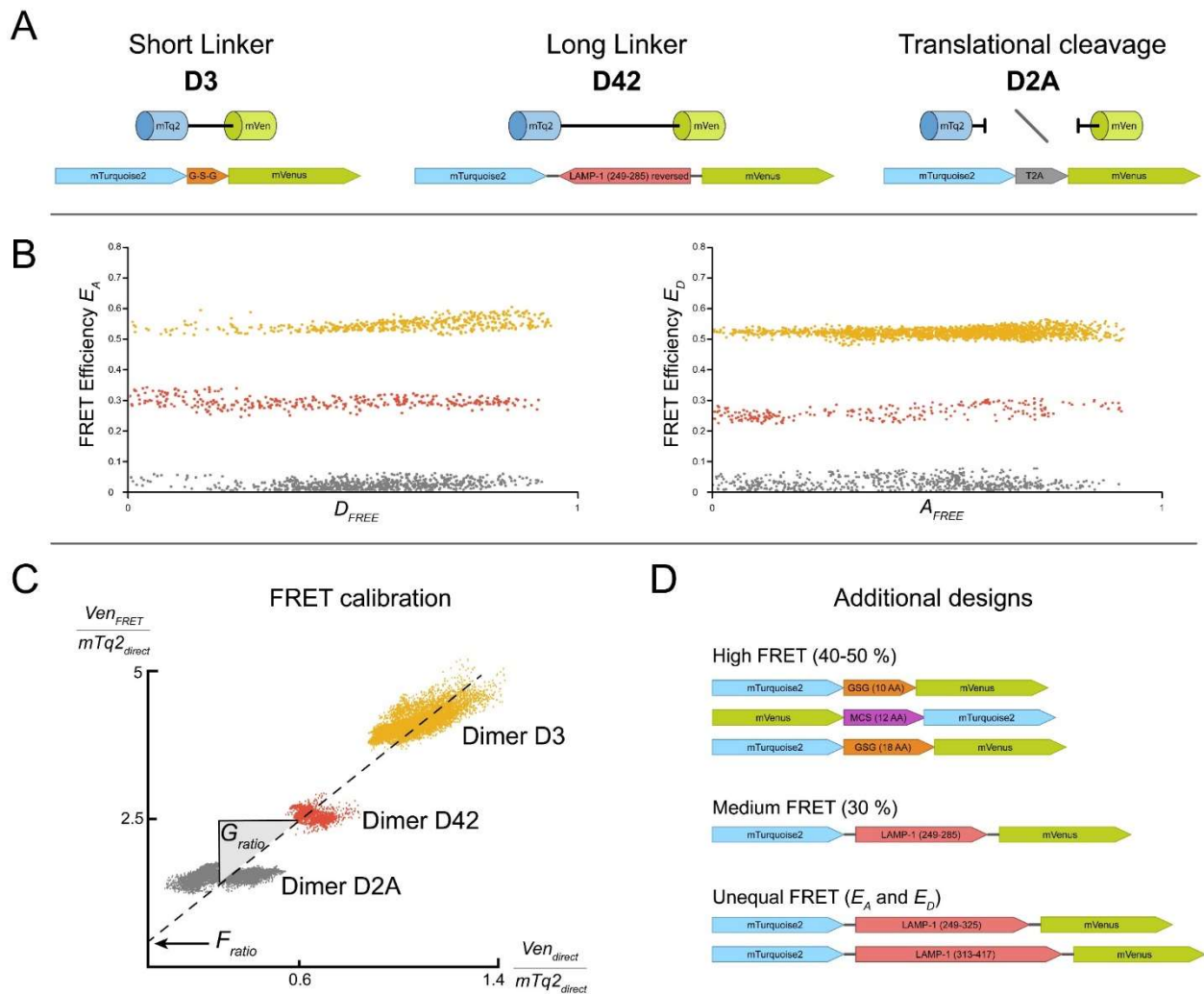


Figure 10: FRET calibration with dimer constructs. **A**, Schematic view of the dimer design that resulted in an optimal FRET calibration. These dimers were chosen for all following Two-Hybrid FRET experiments: Dimers are categorized in three categories: “Short linker”, “Long Linker” and “Translational cleavage”. Dimer names are indicated below the category in bold. The D3 dimer contains a Glycine-Serine-Glycine (GSG) linker, which is indicated in orange. the D42 dimer contains a 37 amino acid arbitrary sequence (a reversed sequence derived from LAMP1, displayed in red). The linker contains additional 5 amino acids (Glycine or Serine) between the fluorophores, adding up to a 42 amino acid linker sequence. The rightmost dimer construct (D2A) contains a linker that encodes a T2A peptide, which causes translational cleavage between both fluorophores. The linker is shown in grey. **B**, Measured FRET efficiencies are displayed for the Dimers in A (E_A and E_D). Dimer data are color coded to their corresponding linker color shown in A: The upmost orange data refer to the D3 dimer, the red data points correspond to D42 data, and the grey data points are measured with the D2A dimer. **C**, The FRET calibration diagram is displayed with data of the three dimers displayed above. The diagram plots the relative sensitized emission signal $Ven_{FRET}/mTq2_{direct}$ (Y-axis) against the relative donor quenching signal $Ven_{direct}/mTq2_{direct}$ (X-axis) from measurements of the dimers. Note that $mTq2_{direct}$, Ven_{FRET} and Ven_{direct} are acquired from the S_{CFP} , S_{FRET} and S_{YFP} signals after spectral correction (equation 9-11). The resulting linear relationship between the dimers can be used to determine the G_{ratio} and F_{ratio} (equation 19): As indicated, the G_{ratio} and F_{ratio} are derived from the y-axis offset and slope, respectively. Dimer data are color coded as before with their corresponding names (D3, D42, D2A). **D**, Schematic view of other dimers that I created. Their corresponding FRET efficiencies are indicated. Both dimers shown on the bottom with long linkers did not result in equal and stable FRET efficiencies between E_A and E_D .

5.1.3 Development of a custom made Matlab script for Two-Hybrid FRET data analysis

In order to increase the efficiency of data analysis and also to be able to obtain an instrument independent analysis platform compatible with instruments chosen for aims 2-4, the FRET analysis algorithms were implemented in Matlab.

Fluorescence data tables consisting of three fluorescence values (S_{CFP} , S_{FRET} , S_{YFP}) are used to calculate Two-Hybrid FRET binding curves (refer to the section Two-Hybrid FRET theory). The custom Matlab script contains a graphical user interface for the calibration and nonlinear fitting algorithm. It is superior to the formerly used excel sheet¹ by determining the lowest error fit for the binding curves automatically, independent of the researcher. The FRET analysis step outlined here was designed to support input data from all instruments used in the aims 2-4: Flow cytometer data are usually generated as .fcs or .ffa files (aim 2) and image-based fluorescence data files are generated in .csv file format (aim 3 and 4). Thus, this software supports not only photometry data (.xls data files), flow cytometry data (.fcs and .ffa data files), but also the newly developed image-based fluorescence data files (.csv data), which are discussed in later sections. The original version of this script was developed by Manu-Ben Johny (Columbia University). Adjustments were made to improve the fitting process of both binding curves to happen simultaneously, finding the combined lowest error fit for both curves together. In addition, a function was implemented to merge several datasets of identical samples. The detailed utilization of the script is displayed in my corresponding publication⁸⁶. Due to the newly implemented ability to simultaneously fit both E_A and E_D binding curves to the lowest error fit, the absence of possible human bias in the fitting process, the ability to filter out low and oversaturated fluorescence signals and its general ease of use, the Matlab script resembles a significant improvement in the consistency and speed of FRET binding curve evaluation compared to the previously used excel sheet¹.

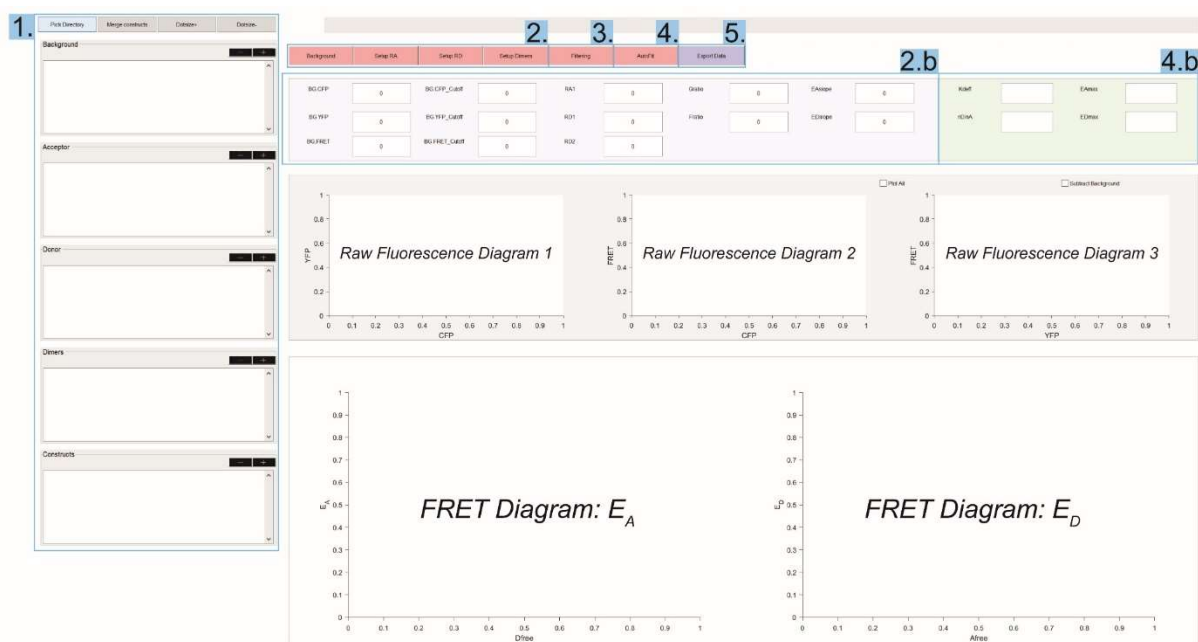


Figure 11: The user interface of the FRET evaluation Matlab script. “Raw Fluorescence Diagrams 1-3” display the fluorescence values of a selected data table in each channel (Diagram 1: YFP vs. CFP, Diagram 2: FRET vs. CFP, Diagram 3: FRET vs. YFP). “FRET Diagram: E_A , E_D ” display the calculated binding curves or dimer calibration FRET data. **1. Upload section:** Fluorescence data tables of calibration samples (Background, Acceptor, Donor, Dimers) and sample data (Constructs) are uploaded in their respective window by pressing the black “+” button on the top right-hand corner of each upload window. Buttons above the upload windows from left to right: Pick Directory, Merge constructs, Dotsize+, Dotsize-. A directory path can be selected with “Pick Directory” to upload fluorescence data tables from a specific folder. The “Merge constructs” button merges all fluorescence data tables uploaded in the “Constructs” window. The Dotsize+/- buttons change the size of data shown in all diagrams. **2. Calibration buttons:** After uploading all calibration samples, the mean background values (“Background” button), the spectral correction factors (buttons “Setup RA” and “Setup RD”) and the FRET calibration constants (“Setup Dimers” button) are calculated from fluorescence data tables uploaded in section 1. **2.b. Calibration parameters:** Calculated calibration constants are shown in their respective field in this section. **3. Filtering:** Raw fluorescence data tables can be filtered for minimum and maximum values by pressing the “Filtering” button. Additionally, a feature to exclude data with high imbalances of donor:acceptor fluorescence emissions can be determined (“Maximum N_A/N_D , N_D/N_A ”). **4. Binding curve fit:** The “AutoFit” button generates the minimum-error value fit with respect to the maximum FRET efficiency only, or the minimum-error value fit with respect to both maximum FRET efficiency and K_D . **4.b. Fit parameter:** The fit parameter, such as $E_{A,max}$, $E_{D,max}$, N_D/N_A and K_D are displayed in this section. **5. Data export:** Two-Hybrid FRET binding curve data can be exported using the “Export” button to plot diagrams in a third-party software.

4.1.4 Validation of the photometry based Two-Hybrid FRET assay using a reference protein-protein interaction

The interaction between CaM and the [WT]-IQ6 motif of myosinVa (Figure 6) is known to result in robust FRET binding curves¹. Therefore, these two binding partners are used as reference and positive control to validate the new fluorophores mTq2 and mVenus and the novel

calibration standards on the photometry setup, because this instrument was the standard prior to my thesis (aim 1).

Binding curves are shown in Figure 12 A. The upper two binding curves display data using the novel FRET constructs. For comparison, the binding curves from Butz et al 2012¹ are shown in the lower part of Fig 12 A. Using mTq2 and mVenus for FRET experiments results in a higher maximum FRET efficiency (35 % $E_{A,max}$ and $E_{D,max}$) compared to the CFP/YFP FRET pair (20 % $E_{A,max}$ and $E_{D,max}$; Figure 12 A, B). Consequently, the mTq2/mVenus FRET pair results in a 75 % increased dynamic range of FRET efficiencies. Both measurements result in a 1:1 binding stoichiometry due to equal maximum FRET values between $E_{A,max}$ and $E_{D,max}$ (Figure 12 B). Even though most instrument specifications were similar, the K_D between both instruments cannot be compared due to differences in the light source and beam pathway between the instrument used here and the instrument used in Butz et al 2012.

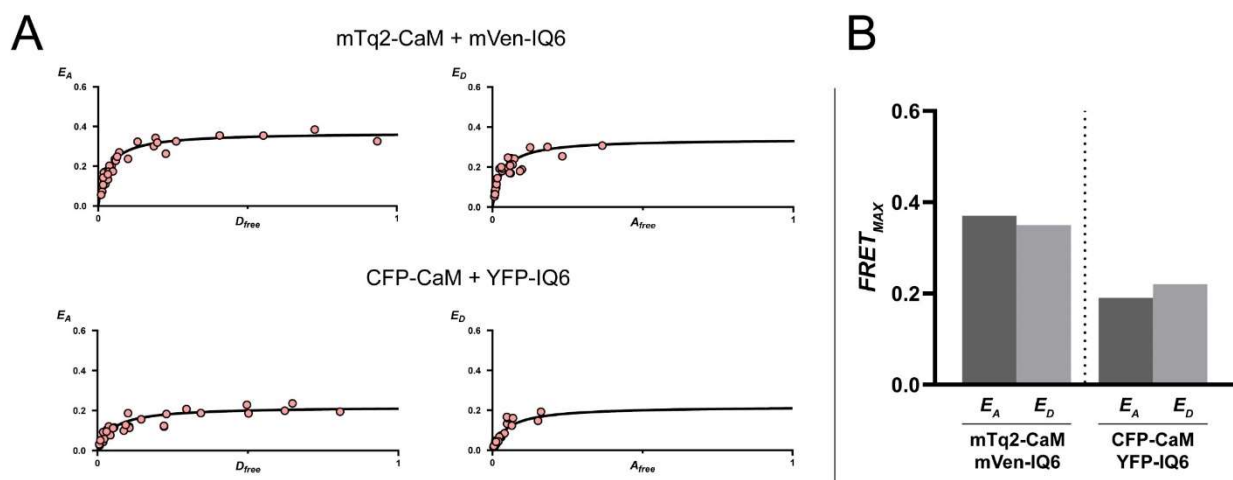


Figure 12: Two-Hybrid FRET binding curves with a novel FRET pair. **A**, Binding curves (E_A and E_D) of CaM interacting with the IQ6 motif of MyosinVa are shown. The top two diagrams were acquired using mTurquoise2 and mVenus as FRET partners (own data). The bottom two binding curves were acquired using CFP and YFP as a FRET pair and are derived from a previous publication (Butz et al. 2012). D_{free} and A_{free} values are normalized. Three samples with different transfection stoichiometries for both proteins were used: 3:1, 1:1 and 1:3 (CaM:IQ6 motif in μg DNA). **B**, $FRET_{max}$ differences using either mTq2 and mVen, or CFP and YFP as a FRET pair for this interaction. Darker columns display E_A maximum FRET values, lighter columns display E_D maximum FRET values. Data derived from binding curves shown in A. D_{free} and A_{free} values are normalized.

5.2 Aim 2 – Development of a flow cytometry based Two-Hybrid FRET assay

All developments established in aim 1 are applied for developing the Two-Hybrid FRET assay on the flow cytometer in this section, as well as the optical plate reader and confocal microscope in the following sections.

The high throughput nature of flow cytometry was exploited to be able to efficiently and quickly screen large numbers of putative protein interaction partners. The method was validated using the reference protein interaction used before (mTq2-CaM and mVenus-IQ6). The flow cytometer binding curves scatter significantly more than the binding curves measured on the photometry setup. Data points containing low fluorescence intensities (which translate into low D_{free} or A_{free} estimations) scatter much more than data points containing high fluorescence intensities (Figure 13). However, due to the high number of single-cell measurements (~50.000 single-cell measurements) for each sample in less than one hour, a robust binding curve fit is still possible. FRET maxima between E_A and E_D are similar, confirming the 1:1 protein interaction stoichiometry measured before. Importantly, the maximum FRET efficiencies are similar on a flow cytometer (32 % for E_A and E_D) compared to measurements using the photometry setup (35 % $E_{A,max}$ and $E_{D,max}$).

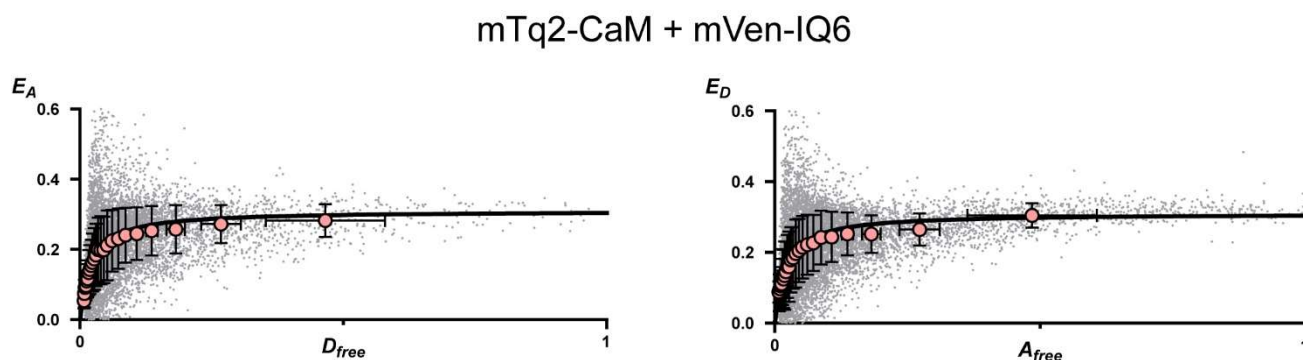


Figure 13: Two-Hybrid FRET on a Flow Cytometer using the reference constructs. Binding curves for the reference protein interaction between mTq2-CaM + mVen-IQ6. Data for the experiments were acquired on a FACS Calibur (BD). Single cell measurements are displayed as grey dots. X-Y binned data are shown in light red. D_{free} and A_{free} values are normalized. Three samples with different transfection stoichiometries for both proteins were used: 3:1, 1:1 and 1:3 (CaM:IQ6 in μg DNA).

5.3 Aim 3 – Development of an image-based Two-Hybrid FRET assay

The advantage of flow-cytometry-based FRET assays is the exceptional high throughput and the high number of data points obtained in one run. The disadvantage is that the flow cytometer suffers from a low fidelity in fluorescence quantification due to the measurement of cells in a streaming flow. To overcome this disadvantage, an image-based Two-Hybrid FRET method on an optical plate reader (Figure 14 A) was developed, which allows for high throughput due to its ability to read multiple samples (multiple wells of a well-plate dish) automatically, while providing a better fidelity compared to the flow cytometer assay. In addition, it provides the ability to compare FRET data to corresponding images. However, this instrument uses large working distance air-objectives (20X) with a maximum NA of 0.6 to switch between wells without the need to focus again. Thus, this assay is limited to cytosolic protein interactions. Like the previously presented Two-Hybrid FRET assays, the image-based Two-Hybrid FRET assay relies on three distinct channels or filter cubes for data acquisition. The device and Filter Cube specifications are displayed in Figure 14.

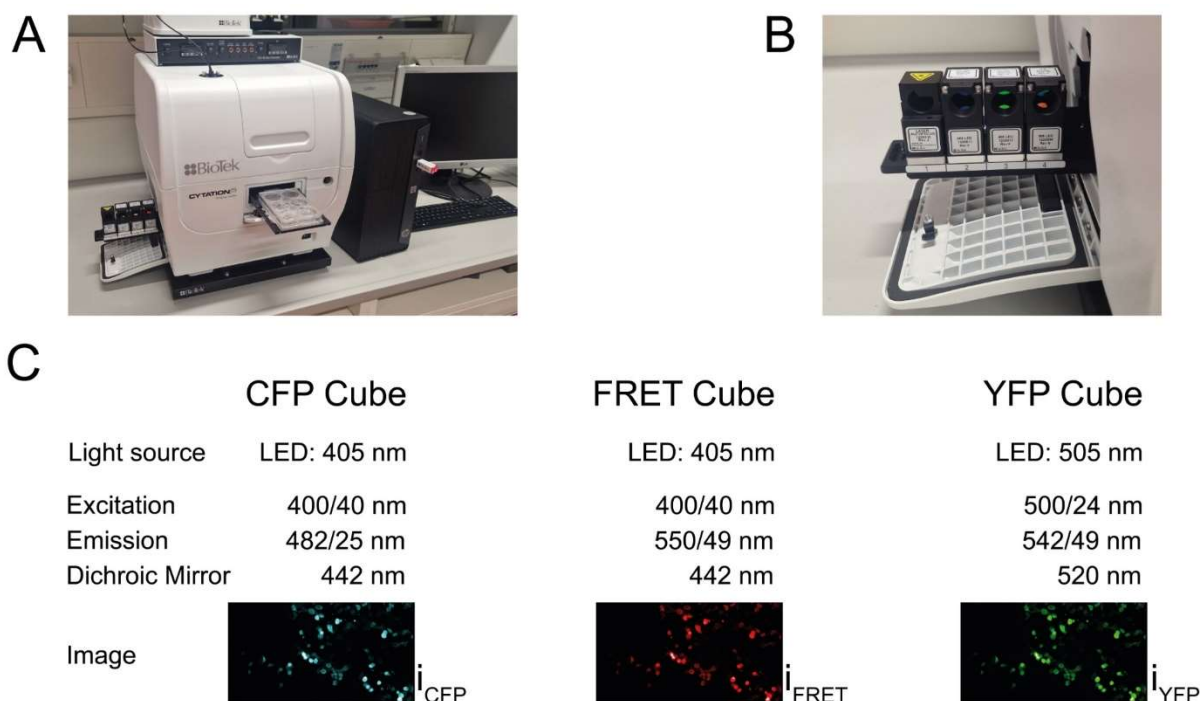


Figure 14: Setup of FRET acquisition channels (Plate reader/wide-field microscope). **A**, Image of the Cytation5 wide-field imaging plate reader used for this protocol. **B**, Installation of the filter cubes to acquire images in all three channels. **C**, Filter cube properties and an exemplary image acquired in all three fluorescence channels (i_{CFP} , i_{FRET} , i_{YFP}).

Image-based approach: Importantly, the image-based Two-Hybrid FRET assay generates fluorescence images (i_{CFP} , i_{FRET} , i_{YFP}) instead of the fluorescence signals (S_{CFP} , S_{FRET} , S_{YFP}) that are acquired in photometry or flow cytometry assays. However, the fluorescence signals (S_{CFP} , S_{FRET} , S_{YFP}) are later derived from ROIs (regions of interest) within the multi-stack image (i_{CFP} , i_{FRET} , i_{YFP}) in two steps: Automatic cell detection using Ilastik, and Data evaluation using ImageJ. These steps are described in the following two sections and outlined in Figure 15 A and B.

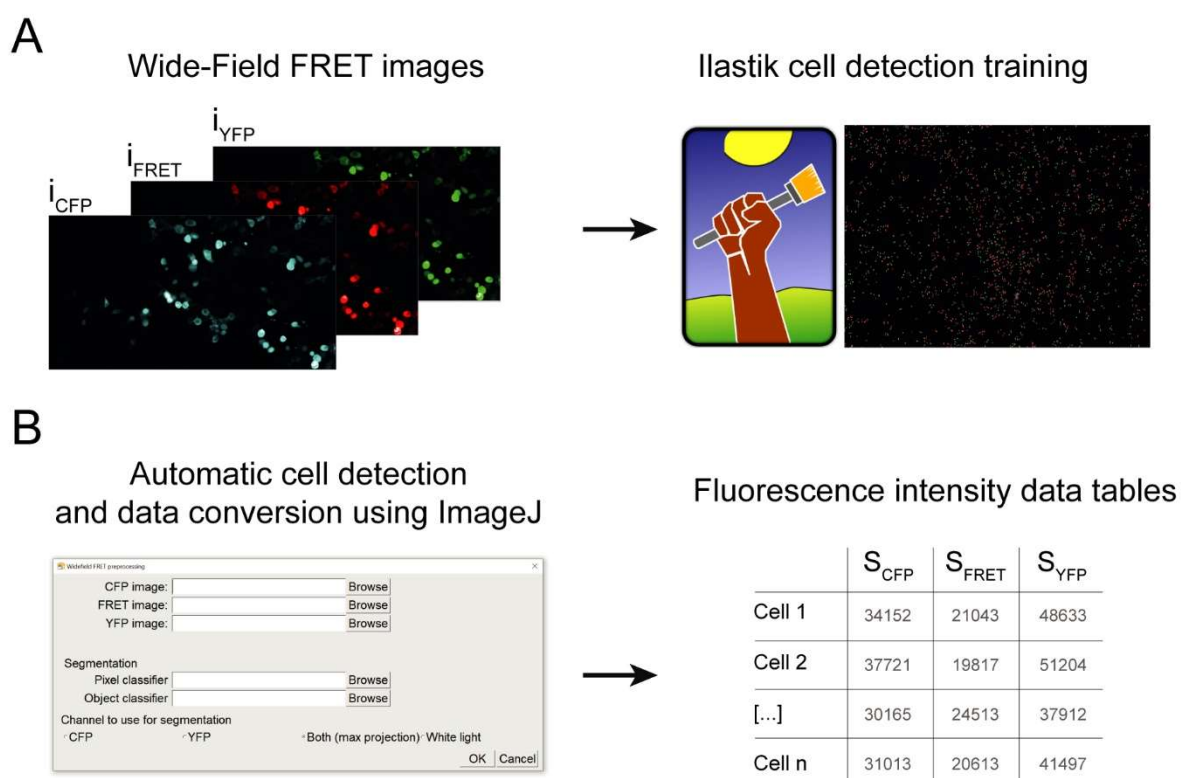


Figure 15: Workflow design of wide-field image-based Two-Hybrid FRET assays. **A**, Any representative wide-field FRET image is loaded into the Ilastik software for cell detection training. The files for automatic cell detection are exported from Ilastik and used for every image required for the Two-Hybrid FRET assay. **B**, The custom “Cell_detect” ImageJ macro utilizes the trained Ilastik files and any fluorescence image captured in CFP, FRET and YFP channels. By starting the macro, cells are annotated with whole-cell ROIs. The fluorescence intensity values from the ROIs are transformed into fluorescence intensity values (S_{CFP} , S_{FRET} , S_{YFP}). All three signals are tabulated corresponding to the cell (ROI) they were derived from (Cell 1, 2...).

Automatic cell detection using Ilastik

Due to the large FOV and the high number of captured cells (50-400 cells per image), manual ROI annotation would be time-consuming. To overcome this problem, automated cell detection enables the determination of whole-cell ROIs without manual intervention (Figure 15 A).

Wide-field multi-stack images containing three fluorescence images (i_{CFP} , i_{FRET} , i_{YFP}) are acquired for each calibration and protein interaction sample (Figure 15 A, left panel). Then, one representative multi-stack image of any dimer or sample is loaded into the Ilastik program to train the software to automatically detect cells in images (Figure 15 A, right panel). Two classifiers are trained for this process: the “pixel_classifier” and “object_classifier”. Both classifiers are then used to identify cells in the fluorescence images (i_{CFP} , i_{FRET} , i_{YFP}), which are later converted into averaged fluorescence signals (S_{CFP} , S_{FRET} , S_{YFP}), which are required for FRET evaluation.

“pixel_classifier”: To train the first classifier (depicted in Figure 16 A), cells and background are annotated by drawing lines in both regions (yellow lines are drawn across cells, blue lines in background regions). The software uses the annotations to predict a segmentation of the image into cells and background. The segmentation is shown in faint yellow (cells) and dark blue (background) while annotating in the image (Figure 17 A). As shown in Figure 16 A, only nine annotations are necessary to generate an accurate segmentation of the image. This segmentation is the first of two classification steps, labelled “pixel classification”. The training is saved as a file (“pixel_classifier.ilp”) and used later for data evaluation.

“object_classifier”: The second classification step is named “object classifier” (Figure 16 B) and is used as a quality control for detected cells. It discriminates detected cells into “good” and “bad” objects. The former refers to representative cell shapes, the latter aims to exclude objects that do not represent cells in size and shape. Like the pixel classifier, twelve exemplary objects are annotated manually (dark green: representative cell shapes, dark red: Cell clusters or artefacts). The software will categorize all remaining objects in the image in one of those two categories, as shown in faint green and faint red colored objects in Figure 16 B. The images displayed in Figure 16 only display a small image excerpt of a wide-field image, which can contain multiple hundred cells. Like the pixel classification, the object classifier is also saved as a file (“object_classifier.ilp”) and used in the next step, data evaluation using ImageJ.

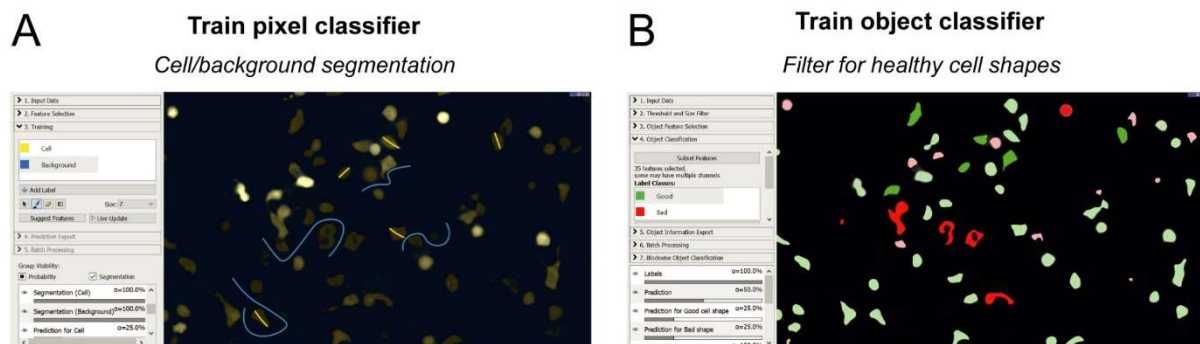


Figure 16: Workflow of the automatic cell detection using Ilastik **A**, Screenshot of the pixel classifier user interface in Ilastik. Yellow lines crossing some cells in the image are manually annotated regions that represent cells. Blue lines in the image are manually annotated background regions. The Ilastik software then predicts cells and background for the rest of the image. The segmentation from the software is shown in faint yellow and dark blue while curating the image manually. **B**, The segmentation data is used on the same image in the second step, using the object classifier in Ilastik. The segmented image is used to manually annotate predictions of cells in two categories, good and bad. Previously detected cell shapes are annotated manually by clicking on the shape while selecting either good (green) or bad (red). The Ilastik software then predicts similarly to **A** the good and bad cell shapes for the rest of the image in faint green and faint red, respectively.

Data evaluation using ImageJ

After training the two classifiers in the Ilastik software to automatically identify cells within the images, a customized ImageJ macro (“Cell_detect”) uses both the “pixel_classifier.ilp” and “object_classifier.ilp”, as well as the acquired fluorescence images (Figure 15 B, left panel): The “Cell_detect” ImageJ macro defines regions of interest (ROIs) around detected cells, based on the two classifiers trained before and transforms the generated ROIs into fluorescence data tables, which are used for the Two-Hybrid FRET evaluation. Each ROI contains three averaged fluorescence values, derived from the three images i_{CFP} , i_{FRET} and i_{YFP} (Figure 15 B, right panel). The evaluation speed of this method is comparable to the level of flow-cytometer based Two-Hybrid FRET assays with the benefit of an included quality control via the object classifier.

Validation of the Wide-field image-based Two-Hybrid FRET

Two-Hybrid FRET binding curves of the reference protein interaction using the optical plate reader and automated cell detection are displayed in Figure 17. The accuracy of data points across the fit is significantly better compared to the flow-cytometer Two-Hybrid FRET assay

while the measurement speed is comparable between both instruments. However, the number of data points is lower for the optical plate reader assay due to the small field of view used for image acquisition. This factor can be eliminated by stitching multiple images or using a 4X objective instead of a 20X objective to increase the amount of data points. However, large images require better computing hardware, especially RAM. As displayed, a sufficient number of data points is generated even by using small excerpts of wide-field images: The binding curve is well covered at all x-values with data points and Maximum FRET efficiencies are comparable to previous results for this protein interaction (34 %) for both $E_{A,max}$ and $E_{D,max}$. Two interaction samples were measured in a 2:1 and 1:2 stoichiometry of donor:acceptor for the displayed binding curves. The optical-plate reader image-based Two-Hybrid FRET assay generates accurate binding curves without the need of manual ROI drawing.

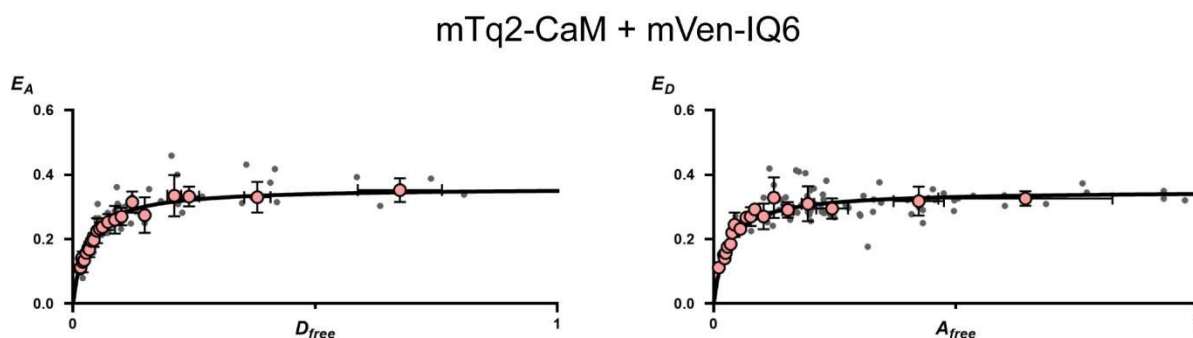


Figure 17: Binding curves using the image-based plate reader Two-Hybrid FRET assay. Each grey data point represents one detected “good” cell shape from the multi-stack image (i_{CFP} , i_{FRET} , i_{YFP}) by using an optical plate reader equipped with a wide-field microscope and evaluation with Ilastik as shown in Figure 15 and 16. The fluorescence intensity information from these cells were converted into data triplets of fluorescence signals (S_{CFP} , S_{FRET} , S_{YFP}) and evaluated using the Matlab Two-Hybrid FRET script. X-Y binned data points are shown in light red. Two different transfection stoichiometries were used for the protein interaction: 2:1 and 1:2 μg plasmid DNA of the donor and acceptor proteins.

5.4 Aim 4 – Development of a confocal Two-Hybrid FRET assay

A confocal image-based Two-Hybrid FRET assay was developed which allows for a high resolution and subcellular FRET analysis in microdomains such as endosomes or lysosomes. The development of the confocal image-based Two-Hybrid FRET assay was crucial for subcellular protein-protein interaction studies that were not possible with previous assays. Thus, multiple different confocal microscopes were employed to test this assay on its robustness and reproducibility: An upright Zeiss LSM 980 Airyscan, an inverted Zeiss LSM 980 Airyscan, a Leica SP8 (inverted) and a Leica Stellaris (inverted). The instrument used for developing the assay is shown in Figure 18 A. Like the image-based plate reader Two-Hybrid FRET assay, the confocal Two-Hybrid assay relies on three distinct channels (CFP, FRET, YFP) to acquire three fluorescence images (i_{CFP} , i_{FRET} , i_{YFP}). The blue and yellow boxes in Figure 18 B and C display recommended properties of these channels. Both the i_{CFP} and i_{FRET} images are excited through the same excitation wavelength (445 nm) and are acquired simultaneously in Track 1.

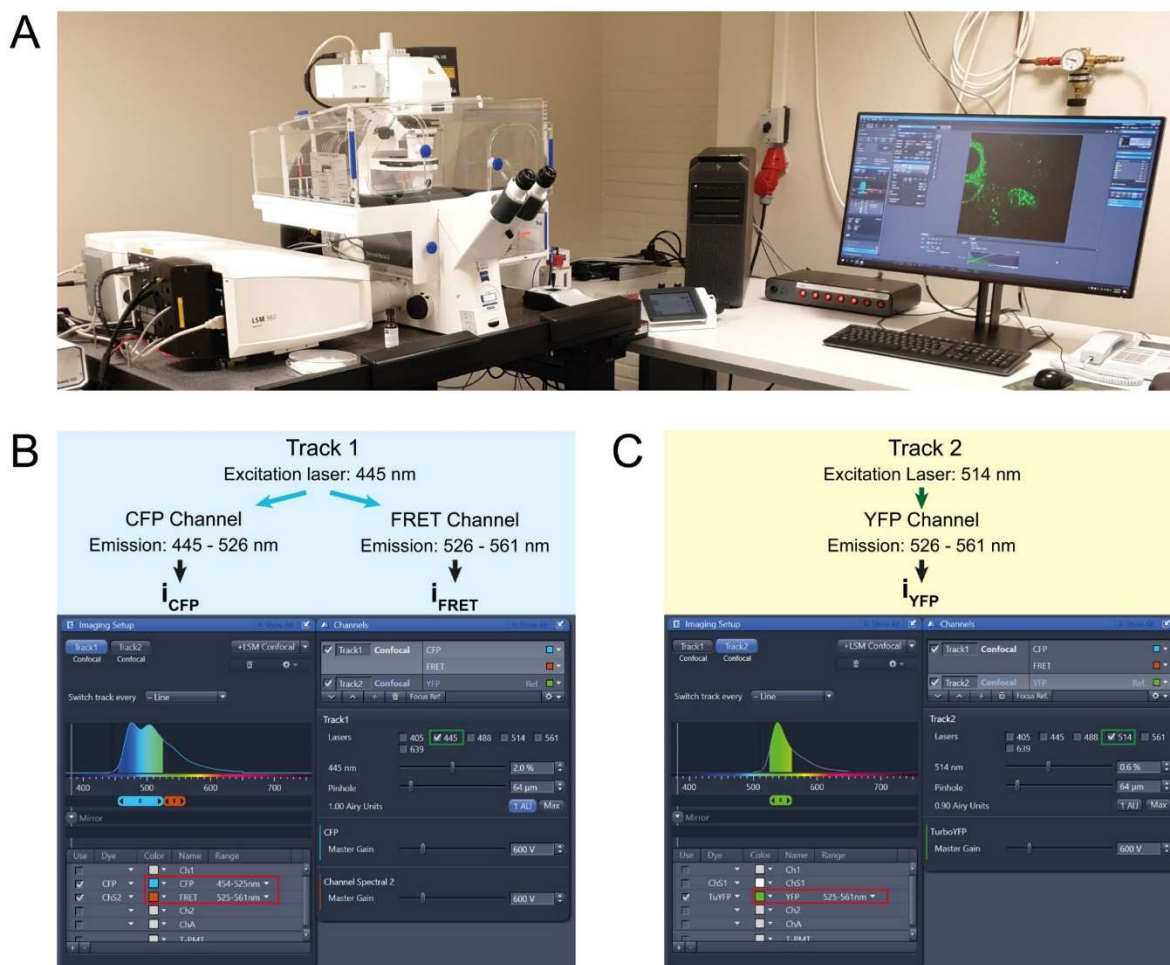


Figure 18: Setup for confocal image-based Two-Hybrid FRET assays. **A**, The Zeiss LSM980 confocal microscope that was used for development of the assay is shown. **B**, Acquisition setup for the CFP and FRET channel is schematically displayed in the blue box above, the acquisition properties are shown below as a screenshot from the acquisition software ZEN blue (Zeiss). Both channels are acquired in parallel using the 445 nm laser for excitation directed to the donor excitation spectrum (green square). The emission signals for the CFP channel are detected from 454-525 nm, the signals for the FRET channel from 526-561 nm (red square). **C**, The acquisition setup for the YFP channel is shown in the yellow box. The YFP channel uses a different excitation wavelength directed to the acceptor excitation spectrum (green square) and is acquired subsequently to Track 1. The emission signals are acquired from 525-561 nm, identical to the FRET channel detection range (red square).

Workflow of confocal image-based Two-Hybrid FRET

The workflow for the confocal image-based Two-Hybrid FRET assay is similar to the wide-field image-based Two-Hybrid FRET assay, only that ROIs are manually determined in subcellular regions, thus there is no cell-detection step required: Multi-stack images (i_{CFP} , i_{FRET} , i_{YFP}) are loaded into ImageJ, and a custom ImageJ macro is started (“FRET_ROI” or “FRET_PIX”). Then, ROIs can be drawn in subcellular regions (Figure 19 A). The macro can be finished by computing all fluorescence values in the ROIs of the multi-stack image into tabulated fluorescence data triplets (S_{CFP} , S_{FRET} , S_{YFP}) as displayed in Figure 19 B.

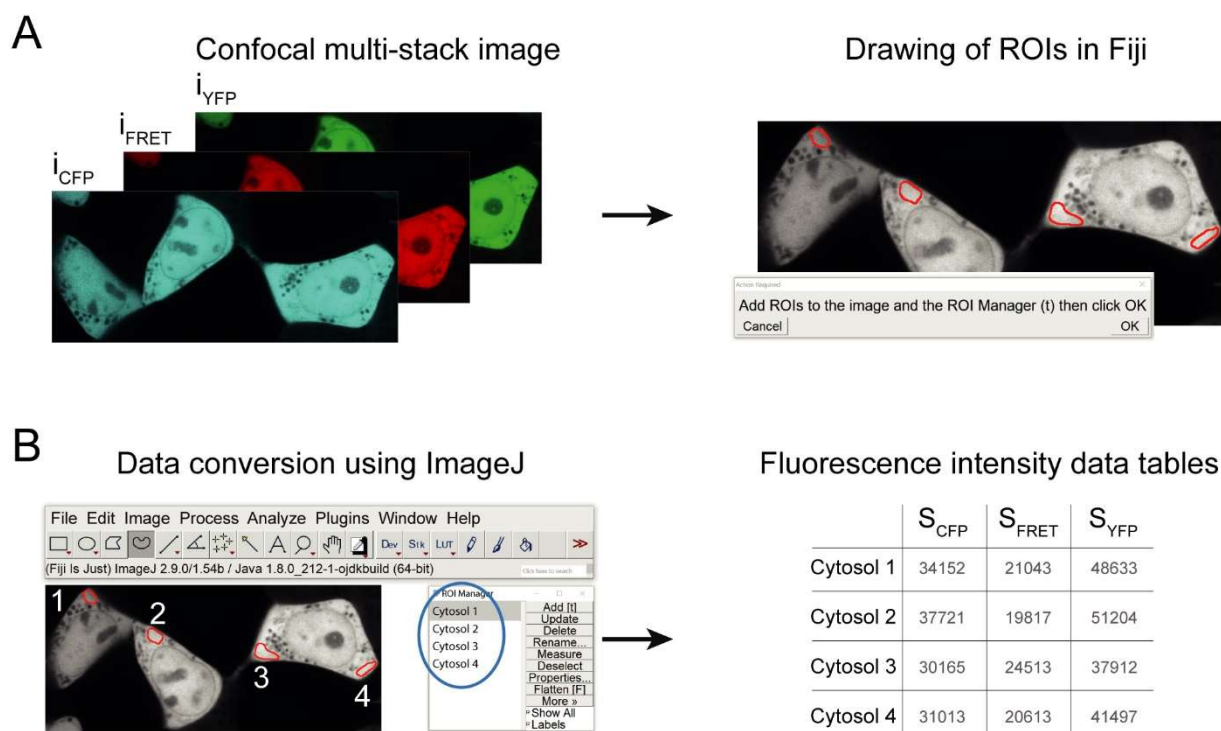


Figure 19: Workflow design of confocal image-based Two-Hybrid FRET assays. **A**, Confocal multi-stack images acquired in the corresponding channels depicted in Figure 18 B and C (i_{CFP} , i_{FRET} , i_{YFP}) are loaded into ImageJ. Then, ROIs are manually drawn of subcellular regions. **B**, ROIs are evaluated into fluorescence intensity data tables

using a custom ImageJ macro. Each ROI can be transformed into a data triplet (“FRET_ROI” custom macro), or alternatively, each pixel in each ROI can be transformed into a data triplet (“FRET_PIX” custom macro). These tabulated data triplets (S_{CFP} , S_{FRET} , S_{YFP}) are shown in the right panel and can be used to generate binding curves using the Two-Hybrid FRET evaluation software depicted in Figure 11.

Validation of the confocal image-based Two-Hybrid FRET

The Two-Hybrid FRET binding curves of the reference protein interaction (CaM with the IQ6 motif from myosinVa) measured on the confocal instrument are shown in Figure 20: FRET maxima for both E_A and E_D are 33 % and similar to values acquired on both the photometry setup (35 %) and the flow cytometer (32 %). Further, E_A and E_D maximum values are similar, indicating 1:1 stoichiometry of the binding reaction. The confocal image-based approach generates more data while requiring less time for measurement (1-2 h) compared to the photometry setup (>2 hours). The accuracy is slightly better when compared to the photometry setup as well. However, the number of data points is significantly lower than measurements on the flow cytometer at similar measurement times. All data points were acquired using only one sample, transfected with 1 μg of donor and acceptor, respectively. Thus, the image-based method achieves binding curve coverage with data points across all X-values without using different amount of DNA of donor and acceptor proteins for transfection: A single sample, measured with the confocal image-based Two-Hybrid FRET assay produces a notably better coverage compared to using three different samples on a photometry setup (Figure 12 A). The binding curves shown in Figure 20 are evaluated using subcellular ROIs from a single sample, as shown in Figure 19 B (left panel).

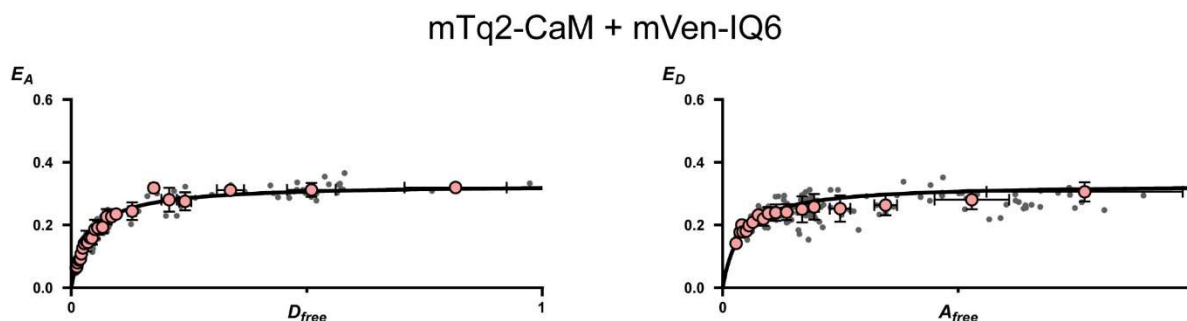


Figure 20: Binding curves using the confocal image-based Two-Hybrid FRET assay. Each grey data point represents one drawn ROI in the multi-stack image (i_{CFP} , i_{FRET} , i_{YFP}) that was converted into a data triplet of fluorescence signals (S_{CFP} , S_{FRET} , S_{YFP}) using the ImageJ macro as shown in Figure 19 (“FRET_ROI”). X-Y binned data points are shown in light red. One transfected sample was used (1 μg CaM and 1 μg IQ6 motif) to generate this binding curve.

Generation of 2D maps of color-coded FRET efficiencies (E_A and E_D)

The confocal image-based Two Hybrid FRET assay allows for binding curves evaluation from subcellular regions. However, it is further interesting to see FRET signals within the image, to get a spatial overview about the apparent FRET signals within a cell. To achieve this, FRET efficiencies can be calculated for each pixel within the image and denoted via color-coding. Thus, a false-color image of a given cell can display spatial FRET efficiencies, giving insight into the distribution of protein-protein events in a cell. However, using this method, no binding affinity information can be derived.

Figure 21 A illustrates the characteristic expression pattern of CaM with the IQ6 motif in a cell cluster. Using the corresponding multi-stack image (i_{CFP} , i_{FRET} , i_{YFP}), the E_A and E_D FRET values were calculated for each pixel in the multi-stack image and color coded as shown in Figure 21 B using the custom “FRET_alpha” ImageJ macro. Two images are generated showing the image in color coded E_A and E_D values. To exclude background and subcellular regions with low fluorescence values, an alpha-blending step was conducted, as shown in Figure 21 C. Alpha-blending transforms low fluorescing regions to be transparent on a black background layer. This leads to the distinct visibility of regions with notable fluorescence signals in colors, excluding background signals and low-fluorescing regions in the image. The LUTs (look-up tables) are shown on the right side for both images in Figure 21 B and Figure 21 C, respectively. The color-coded FRET efficiencies correspond well to the binding curves shown in Figure 20 with a maximum of 33 % (yellow areas) and multiple regions with lower efficiencies, proving that the 2D mapping of E_A and E_D is a helpful tool to localize FRET signals in an image. The E_A and E_D values are not similar in this cell cluster, indicating a lower abundance of donor molecules. FRET efficiencies vary between cells, and further, in different regions within a cell. Thus, the FRET efficiencies, as well as the expression of a transfected protein can be analyzed using this method. However, this method does not provide insight into the relative binding affinity of an interaction.

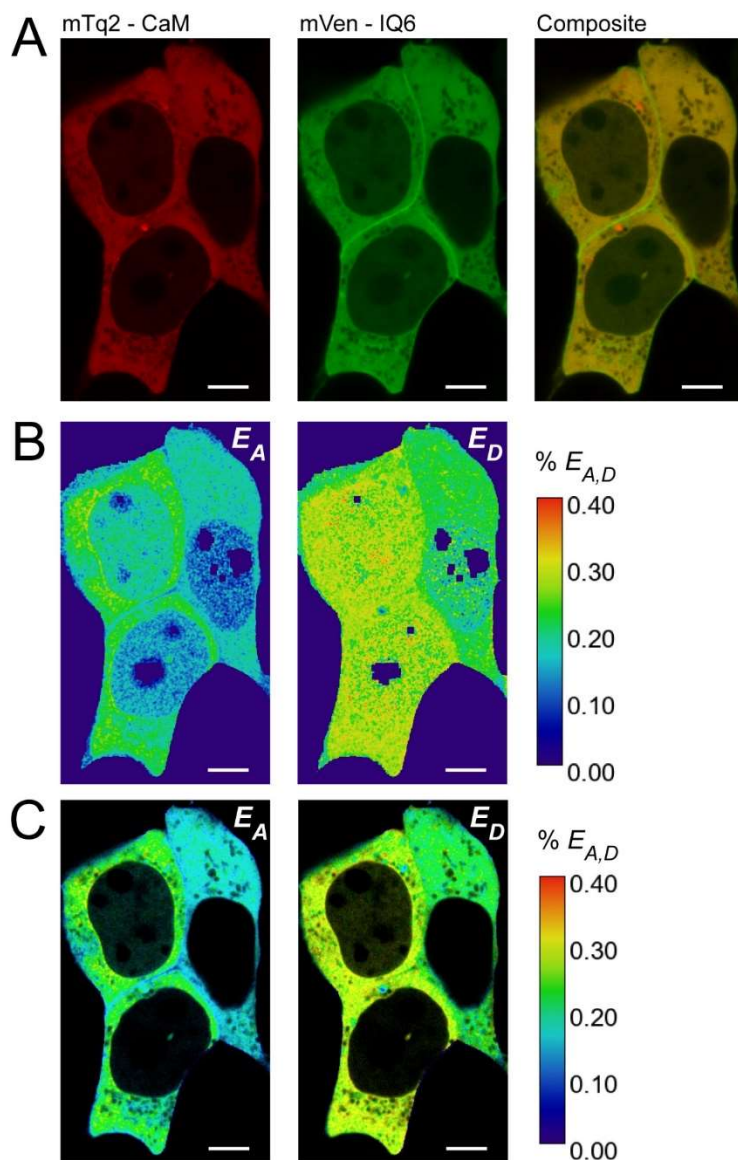


Figure 21: 2D map of color-coded FRET efficiencies (E_A and E_D) **A**, Confocal images of cells expressing both mTq2-CaM (red) and mVen-IQ6 (green). From the Two-Hybrid FRET multi-stack image (i_{CFP} , i_{FRET} , i_{CFP}), only i_{CFP} (displaying mTq2-CaM in red) and in the i_{YFP} (displaying mVen-IQ6 in green) are displayed. The composite image from these images is shown on the right. **B**, Using the image based Two-Hybrid FRET calculation for each pixel in the image, E_A and E_D FRET efficiencies are displayed and color-coded as shown on the right. The calculation was done using the multi-stack image (i_{CFP} , i_{FRET} , i_{YFP}) and running a custom ImageJ macro (“FRET_alpha”). The required calibration constants were acquired beforehand using the FRET evaluation software shown in Figure 11. **C**, The FRET efficiencies from B are now processed using alpha blending of the composite image. The color-coded FRET efficiencies are unchanged, but dark regions are displayed with a non-transparent, black overlay.

Part II: Characterization of Protein-Protein interactions using FRET assays

In part II the techniques established in part I were applied to investigate protein-protein interactions: In aim 5, the IQ6 binding domain is mutated to decrease its binding affinity to CaM. This was used to assess the reliability of determining relative binding affinities by comparing the mutated IQ6 binding curves to the [WT]-IQ6 reference protein interaction on the established instruments for Two-Hybrid FRET. In aim 6, the interaction between the endolysosomal cation-channels TPC1, TPC2 and TRPML1-3 with Rab-GTPases were investigated using the confocal image-based Two-Hybrid FRET method on a subcellular level.

5.5 Aim 5 – Cross-validation of determining protein binding affinity on four instruments

One challenge is to reliably compare relative binding affinities and FRET efficiencies across different FRET setups (photometry, flow cytometry, imaging plate reader, confocal microscope). However, the ability to determine both binding affinities and maximal FRET efficiencies is an advantage of the Two-Hybrid FRET technique, which sets it apart from other FRET assays. This section is set out to experimentally confirm that FRET efficiencies and relative binding affinities are independent of the FRET setup. Such an experimental validation would be considered robust, if a set of test pairs would yield similar FRET parameters across different FRET setups. In order to generate a set of test pairs, the mTq2-CaM with mVenus-IQ6 protein interaction was used and several mutations were introduced in the canonical IQ6 motif to screen for mutations that decrease the binding affinity to CaM. The idea was to generate test pairs which are as closely related to each other as possible, with the only difference being their binding affinities.

To this end, the canonical IQ motif of human myosinVa was compared across different mammalian species in order to identify highly conserved residues implicated in CaM binding (Figure 22 A). The canonical sequence of the IQ motifs of myosinVa is remarkably similar across all displayed Tetrapoda species (*H. sapiens*, *M. musculus*, *R. norvegicus*, *G. gallus*, *X. laevis*), as shown in Figure 22 A. The motif displays a perfect sequence conservation in *H. sapiens*, *M.*

musculus and *R. norvegicus*, and only one conservative substitution at position 5 (F) in *G. gallus* and *X. laevis*. Despite their phylogenetic distance, model organisms like *D. melanogaster*, *C. elegans*, and *A. thaliana* share four invariant positions in IQ motifs that are analogous to the IQ6 from myosinVa in *H. sapiens*. All invariant positions are displayed in bold. The phylogenetic relationship between the model organisms is displayed in Figure 22 B.

To alter the binding affinity of the IQ6 motif to CaM, five positions in the *H. sapiens* IQ6 motif were mutated: Positions that varied across shown species are chosen for mutation to assess whether these are sufficient to lower the binding affinity, and to avoid a complete abolishment of binding. These positions were substituted with Alanine or Isoleucine: [F5A]-IQ6 [M9A]-IQ6, [R7A]-IQ6 and [K11i]-IQ6. Additionally, the Arginine at position 6, which is invariant across all species, was mutated in case the less conserved positions do not result in a significant loss in binding affinity.

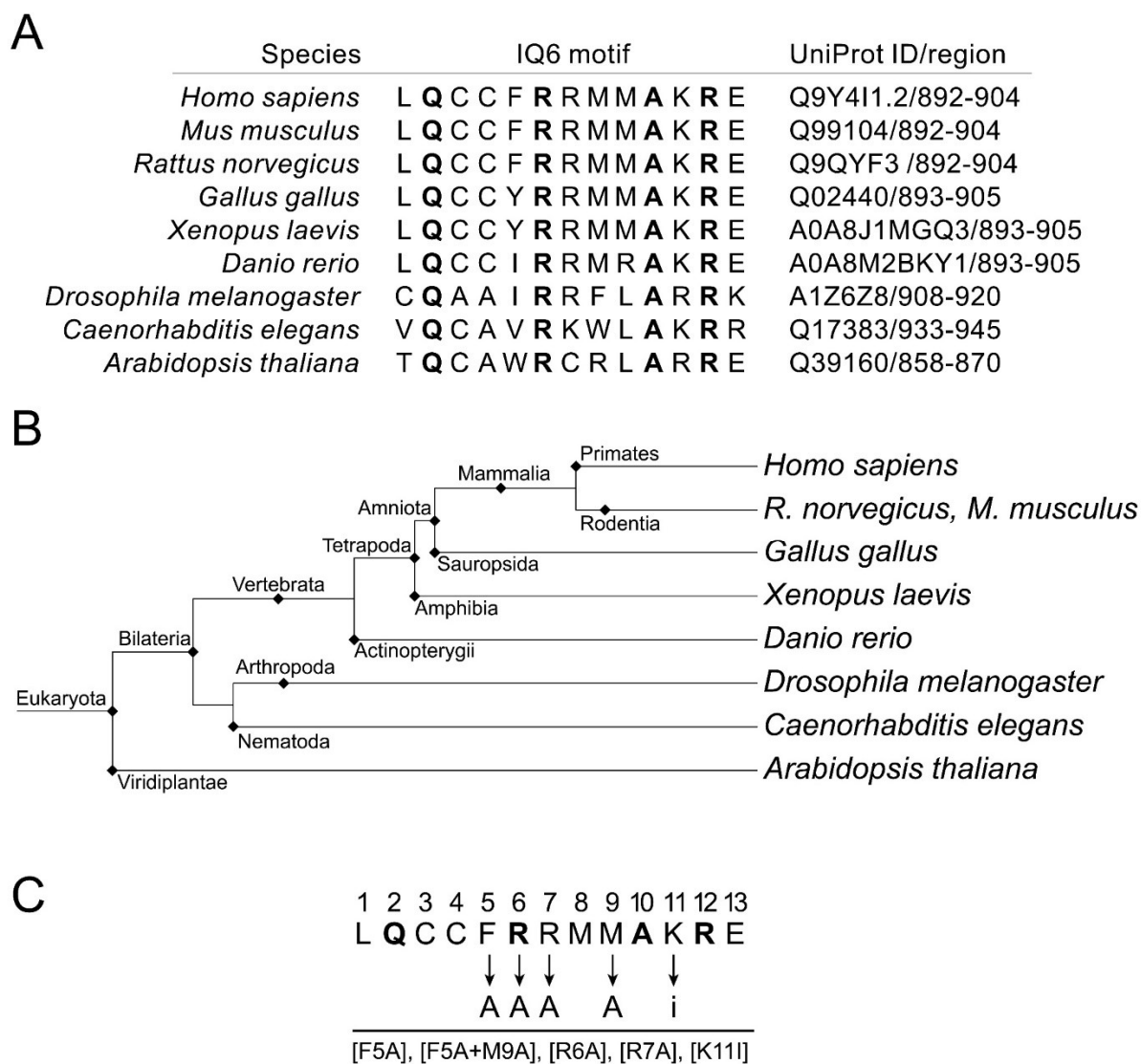
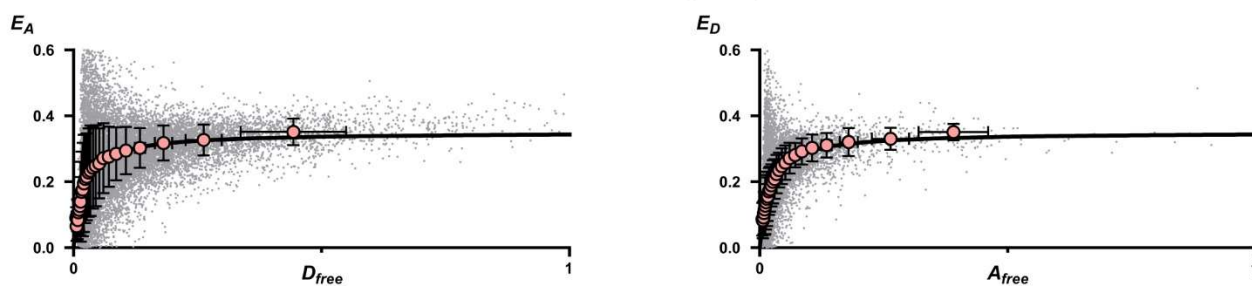


Figure 22: Sequence alignment of the IQ6 motif A. The sequence of the myosinVa IQ6 motif or analogous IQ motifs are displayed for 8 different model organisms. Conserved amino acids between all listed species are shown in bold letters. The UniProt ID of the myosinVa protein (or homologue) and the positions of the IQ6 motif in each protein are indicated in the rightmost column, separated by a slash. **B**, Phylogenetic relationship of the species listed in A. Phylogenetic data were acquired from the NCBI taxonomy database and visualized using iTOL. Prominent taxa are highlighted and labeled according to their localization in the tree. **C**, The [WT]-IQ6 canonical motif of *H. sapiens* is displayed. All generated mutants are indicated with their position and mutated amino acid, indicated by the black arrows. Each mutation was labelled corresponding to the exchanged amino acid and position: [F5A]-IQ6, [F5A+M9A]-IQ6, [R6A]-IQ6, [R7A]-IQ6, [K11I]-IQ6.

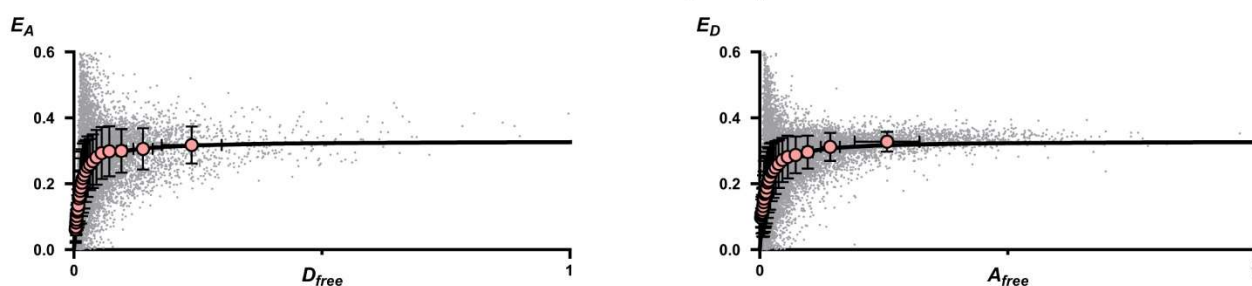
Validation of the set of mutated test pairs by flow cytometer Two-Hybrid FRET

The [F5A]-IQ6, [F5A+M9A]-IQ6, [R6A]-IQ6 and [R7A]-IQ6 motif mutants were compared to the [WT]-IQ6 interaction with CaM by using the Two-Hybrid FRET assay on a flow cytometer (Figure 23). All binding curves are well covered with data points. The data points scatter similar to the binding curve acquired on a flow cytometer shown in Figure 13: The lower the fluorescence values, the higher the scattering of the binding curve. All binding curves show a slight offset from the X-axis 0 value due to the exclusion of low fluorescence signals (< 1 % of maximum signal). All mutants inhabit similar maximum FRET efficiencies to the [WT]-IQ6 interaction, as shown in Figure 24 A (34-38 % FRET), as well as a 1:1 binding stoichiometry between CaM and the IQ6 motifs due to equal maximum FRET efficiencies between E_A and E_D binding curves. The fits are very robust for each interaction, indicated by the low error values that are displayed on each column in Figure 23 A. The K_D is similar for all mutants except [R6A]-IQ6 compared to the wildtype: Their relative K_D changed relative to the WT as follows: [F5A]-IQ6 = $0.53x K_D$, [F5A+M9A]-IQ6 = $0.72x K_D$ and [R6A]-IQ6 = $1.14x K_D$ F5A except the [R6A]-IQ6 mutant, which shows a 5-fold lower binding affinity to CaM than the [WT]-IQ6 motif (5x increased relative K_D , Figure 24 B). The robust fits are further validated by low error values for estimated $E_{A,max}$, $E_{D,max}$ and K_D values in the fitting process.

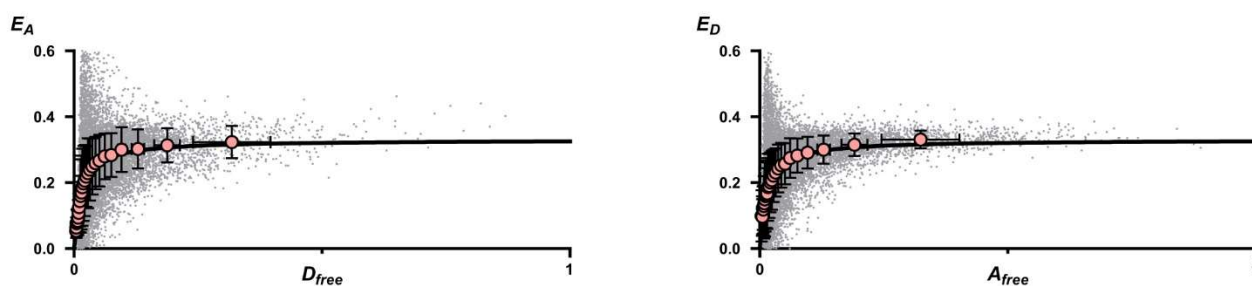
CaM + IQ6 [WT]



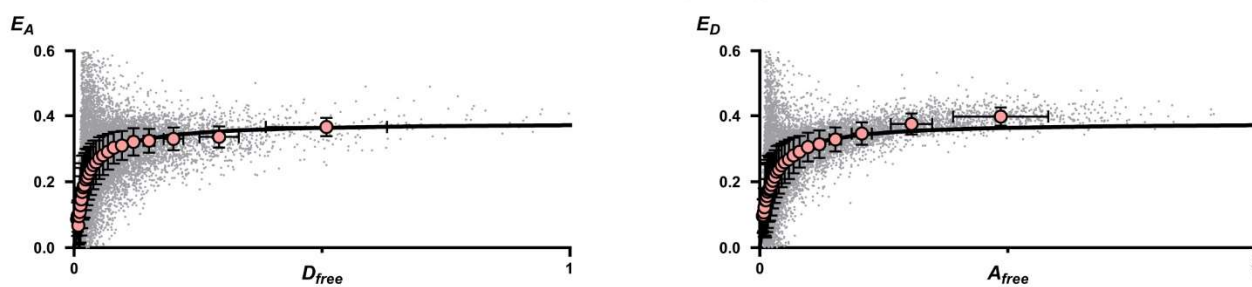
CaM + IQ6 [F5A]



CaM + IQ6 [F5A+M9A]



CaM + IQ6 [R7A]



CaM + IQ6 [R6A]

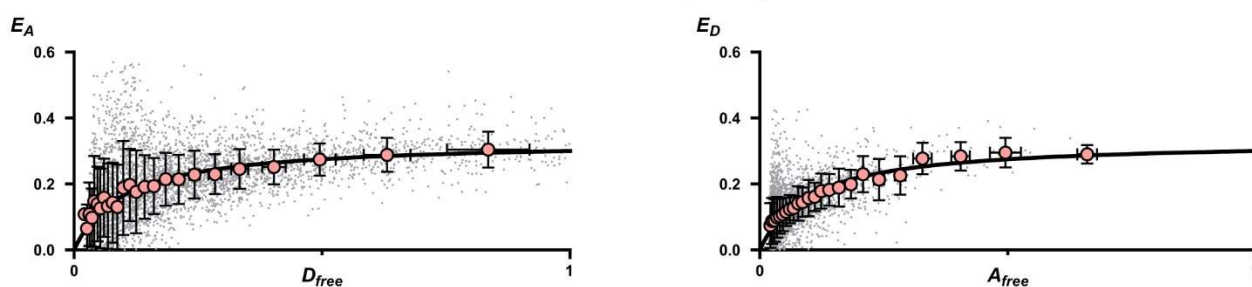


Figure 23: Protein interaction of CaM with mutated IQ6 motifs using a Flow Cytometer. Four different IQ6 mutants were measured using a flow cytometer Two-Hybrid FRET assay (F5A, F5A+M8A, R7A, R6A). These mutants were compared to the [WT]-IQ6 protein interaction with CaM (upmost two diagrams). Each grey dot represents a single cell measurement. Light red circles represent XY-binned data. Three different transfection stoichiometries of donor:acceptor plasmids (2:1, 1:1, 1:2 μg) were used for each interaction.

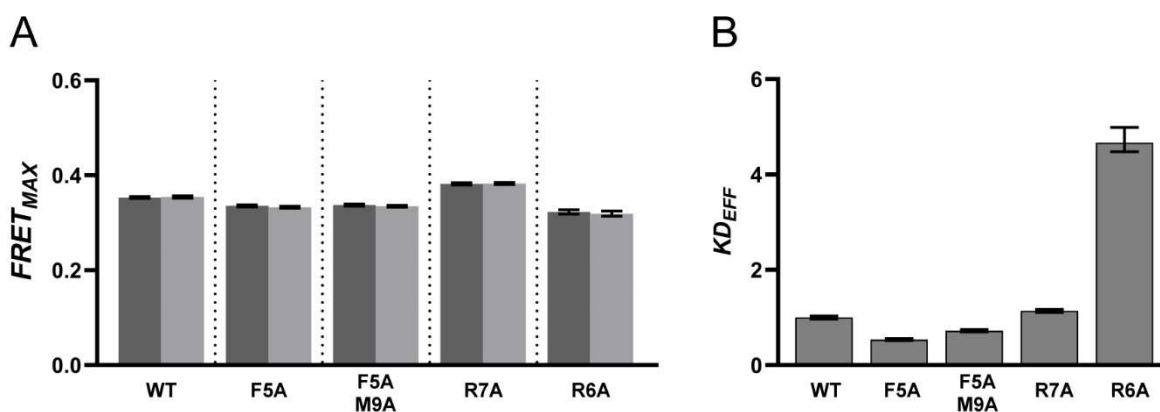
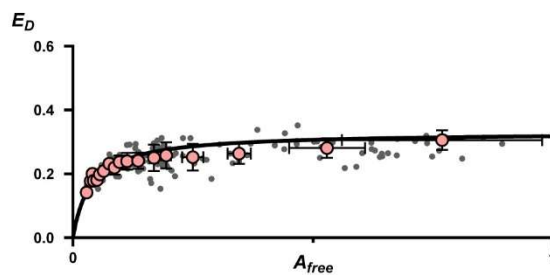
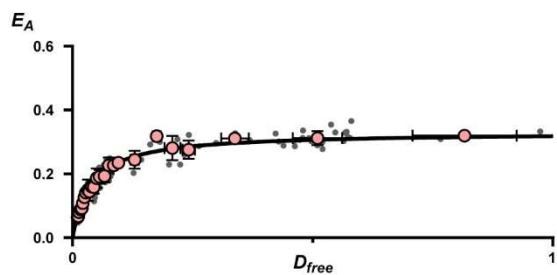


Figure 24: Comparison of binding curve parameter from measurements on CaM with IQ6 mutants using a Flow Cytometer. **A**, The maximum FRET efficiency from binding curves shown in Figure 23 are displayed. Dark grey columns show $E_{A,max}$ values, light grey columns show $E_{D,max}$ values for each mutant. The maximum FRET efficiency is displayed in percent. Error bars represent the 95 % confidence interval (CI) of the binding curve fit for the $FRET_{max}$ value. **B**, The K_D value is displayed for each mutant. All values are normalized to the [WT]-IQ6 with a K_D of 1. Error bars represent the 95 % CI of the binding curve fit for the K_D value.

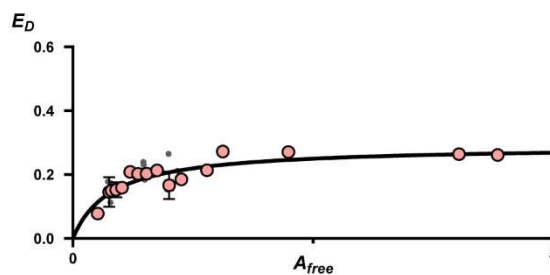
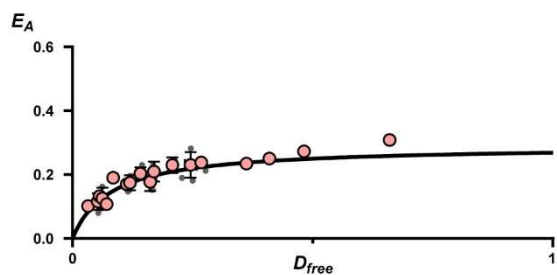
Validation of the set of mutated test pairs by Confocal image-based Two-Hybrid

Next, analog experiments were performed using the image-based Two-Hybrid FRET assay on a confocal microscope and the IQ mutants [F5A+M9A]-IQ6, [R7A]-IQ6, [R6A]-IQ6 and [K11i]-IQ6. The [K11i]-IQ6 mutant was introduced because the mutants that substitute not fully conserved positions ([F5A]-IQ6, [F5A+M9A]-IQ6 and [R7A]-IQ6) did not result a decreased binding affinity in the previous Flow Cytometer screening. The [R7A]-IQ6 and [K11i]-IQ6 mutants are not sufficiently covered with data points in the E_D binding curves, however, the E_A fit is robust. All other mutants display good coverage of both the E_A and E_D binding curves with data points (Figure 25). All mutants display similar maximum FRET efficiencies (33-38 % FRET) as well as a 1:1 binding stoichiometry between CaM and the IQ6 motifs, which is in line with previous measurements on the flow cytometer. Error values for the calculated maximum FRET efficiencies are higher compared to flow cytometer measurements but remain low (Figure 26 A). The [F5A]-IQ6, [F5A+M9A]-IQ6, [R7A]-IQ6 and [K11i]-IQ6 mutants show only a very small decrease in binding affinity. Their corresponding relative K_D increased relative to the WT as follows: [F5A+M9A]-IQ6 = $2.1x K_D$, [R7A]-IQ6 = $1.5x K_D$ and [K11i]-IQ6 = $2.1x K_D$ (Figure 26 B). However, the [R6A]-IQ6 mutant displays a ten-fold decrease in affinity ($10x K_D$) to CaM compared to the [WT]-IQ6 motif, which is higher than the estimated value calculated from the flow cytometer (five-fold decrease).

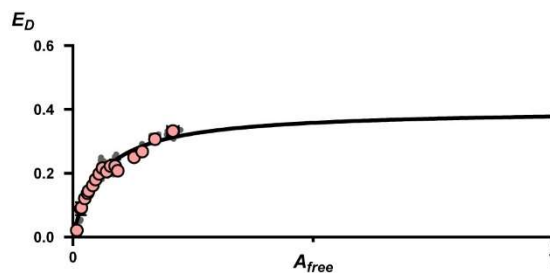
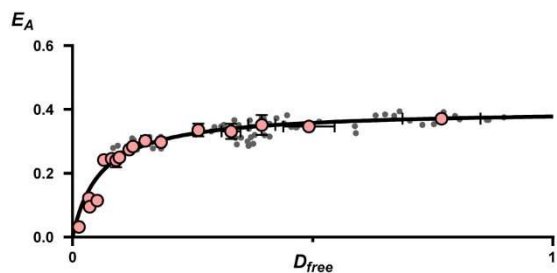
CaM + IQ6 [WT]



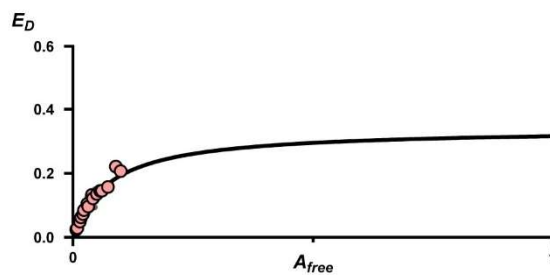
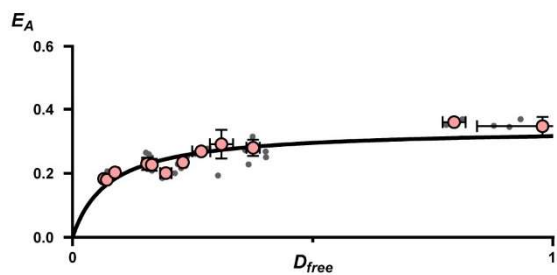
CaM + IQ6 [F5A+M9A]



CaM + IQ6 [R7A]



CaM + IQ6 [K11i]



CaM + IQ6 [R6A]

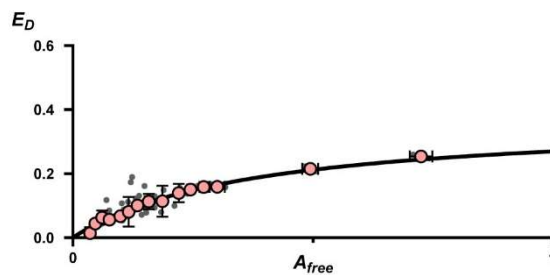
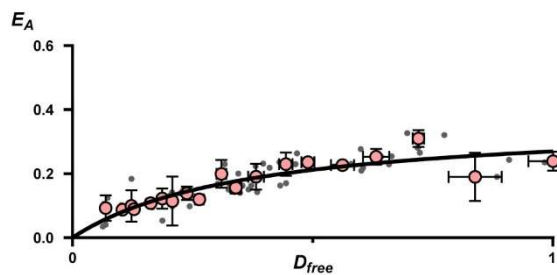


Figure 25: Protein interaction of CaM with mutated IQ6 motifs using the confocal image-based Two-Hybrid FRET assay. The measurements from the Flow Cytometer screen of the mutants [F5A+M9A]-IQ6, [R7A]-IQ6 and R6A shown in Figure 23 were repeated on a confocal microscope using the image-based Two-Hybrid FRET approach. One additional mutant (K11I) was analyzed, and all mutants are compared to the [WT]-IQ6 protein interaction with CaM (upmost two diagrams) on the same device. Grey dots represent manually drawn ROIs that were evaluated using the ImageJ macro shown in Figure 19. Light red circles represent XY-binned data. One transfection stoichiometry (1:1 μg of donor:acceptor) was used for each interaction.

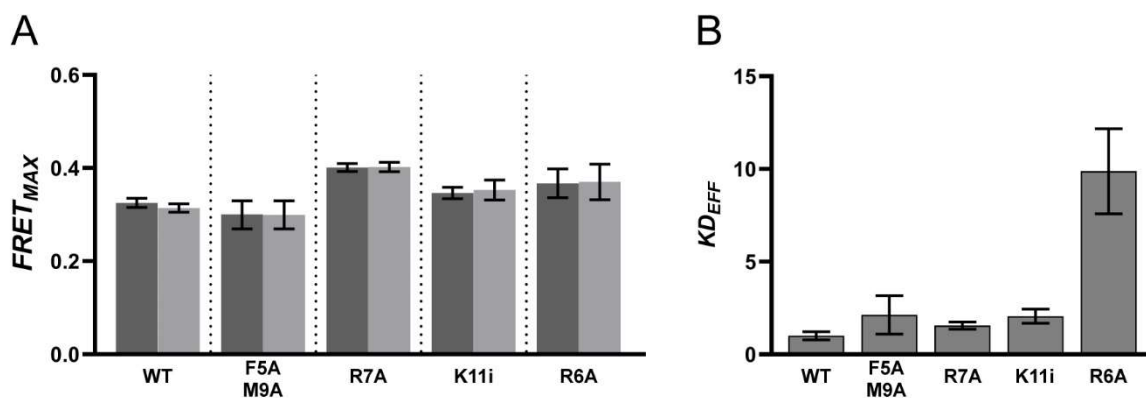


Figure 26: Comparison of binding curve parameter from measurements on CaM with IQ6 mutants using a Confocal Microscope. **A**, The maximum FRET efficiency from binding curves shown in Figure 25 are displayed. Dark grey columns show $E_{A,max}$ values, light grey columns show $E_{D,max}$ values for each mutant. The maximum FRET efficiency is displayed in percent. Error bars represent the 95 % CI of the binding curve fit for the $FRET_{max}$ value. **B**, The K_D value is displayed for each mutant. All values are normalized to the [WT]-IQ6 with a K_D of 1. Error bars represent the 95 % CI of the binding curve fit for the K_D value.

Validation of the test pair by image-based Two-Hybrid FRET using a plate-reader

In the previous screenings, only the [R6A]-IQ6 IQ6 mutant displayed a robust reduction in binding affinity. Therefore, the interaction of WT CaM and [R6A]-IQ6 was tested additionally on an optical plate reader (Figure 27). In these experiments, all binding curves are well covered. The binding curve fits significantly better to the data points compared to flow cytometry data. The maximum FRET efficiency is also similar to previous measurements for both [WT]-IQ6 and [R6A]-IQ6 (36 % and 39 %, respectively). Additionally, similar maximum FRET efficiencies of E_A and E_D indicate a 1:1 binding stoichiometry between CaM and the IQ6 motif. The relative protein binding affinity of the [R6A]-IQ6 mutant with CaM compared is 15-fold decreased, compared to ten-fold on the confocal microscope and five-fold on the flow cytometer. However, the error value for the estimated K_D value is also greater (Figure 28 B).

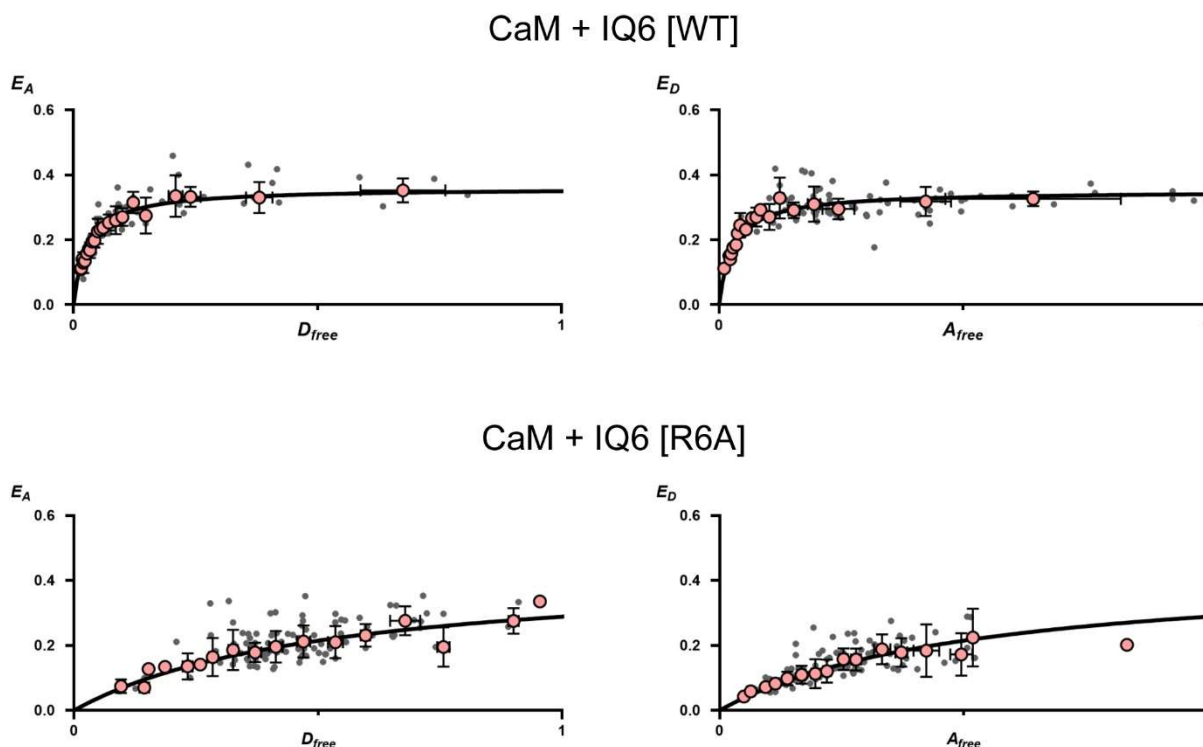


Figure 27: Protein interaction of CaM with [WT]-IQ6 or [R6A]-IQ6 using the wide-field image-based Two-Hybrid FRET assay. The [R6A]-IQ6 mutant was analyzed and compared to the [WT]-IQ6 interaction with CaM (upmost two diagrams) using an optical plate reader. Grey dots represent data from automatically identified cells using Ilastik as shown in Figure 15 and 16. Light red circles represent XY-binned data. Two transfection stoichiometries were used for each interaction (2:1, 1:2 μg of donor:acceptor).

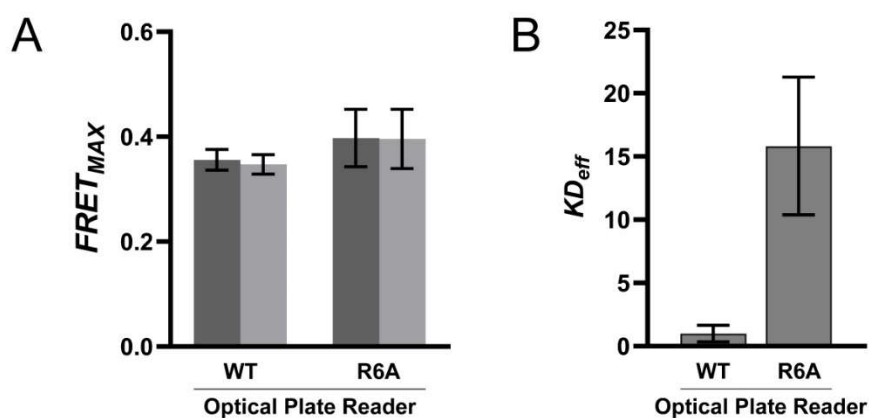


Figure 28: Comparison of binding curve parameter from measurements on CaM with [WT]-IQ6 or [R6A]-IQ6 using an Optical Plate Reader. **A**, The maximum FRET efficiency from binding curves shown in Figure 27 are displayed. Dark grey columns show $E_{A,max}$ values, light grey columns show $E_{D,max}$ values for each mutant. The maximum FRET efficiency is displayed in percent. Error bars represent the 95 % CI of the binding curve fit for the $FRET_{max}$ value. **B**, The K_D value is displayed for both the [WT]-IQ6 and [R6A]-IQ6 mutant. All values are normalized to the [WT]-IQ6 with a K_D of 1. Error bars represent the 95 % CI of the binding curve fit for the K_D value.

Quantifying protein binding affinities using three different confocal microscopes

In summary, the experiments revealed lowered binding affinity for the interaction between CaM and the [R6A]-IQ6 mutant as compared to the wild type interaction the flow cytometer, confocal microscope and optical plate-reader. Next, the interaction of CaM with WT-IQ6 or [R6A]-IQ6 was tested using three different confocal microscopes (Zeiss LSM980 and two Leica SP8 configurations), which are composed by different hardware components, and which utilize different acquisition and detection hardware (Figure 29). Because the confocal image-based Two-Hybrid FRET assay resulted in the best results in terms of accuracy previously (Figure 20, 25), this experiment aims to assess reproducibility and accuracy of the novel image-based confocal FRET assay under vastly different hardware conditions: The goal is to validate the applicability of the confocal Two-Hybrid FRET assay in any laboratory that has access to a confocal microscope. The first instrument used was a Zeiss LSM980 confocal microscope equipped with GaAsP PMT detectors (Figure 25, WT and R6A binding curves). The second instrument used is a Leica SP8X with Multialkali PMTs and different excitation and emission properties (Figure 29, top four binding curves). The third measurements were conducted using different light detector (Multi-Pixel Photon Counter, or: Leica Hybrid Detector S) with further altered excitation and emission settings (Figure 29, bottom four diagrams). In Figure 30 A, all measured maximum FRET efficiencies for E_A and E_D measuring both WT-IQ6 and the [R6A]-IQ6 mutant with CaM on these instruments are displayed. All measured FRET efficiencies are similar with only small differences between the instruments: $E_{A,max}$ and $E_{D,max}$ values are equal in all cases and maximum FRET efficiencies between the WT-IQ6 and [R6A]-IQ6 mutant interaction are similar. Further, total values between instruments are similar as well. The relative estimated K_D between WT-IQ6 and mutant is strikingly similar on all instruments used (Figure 30 B). The standard deviations are moderate and comparable between each instrument. The consistency between the relative binding affinities of WT-IQ6 and [R6A]-IQ6 indicates that the K_D estimation is robust for confocal image-based measurements, even when different excitation and emission settings are used, as well as different hardware for light detection.

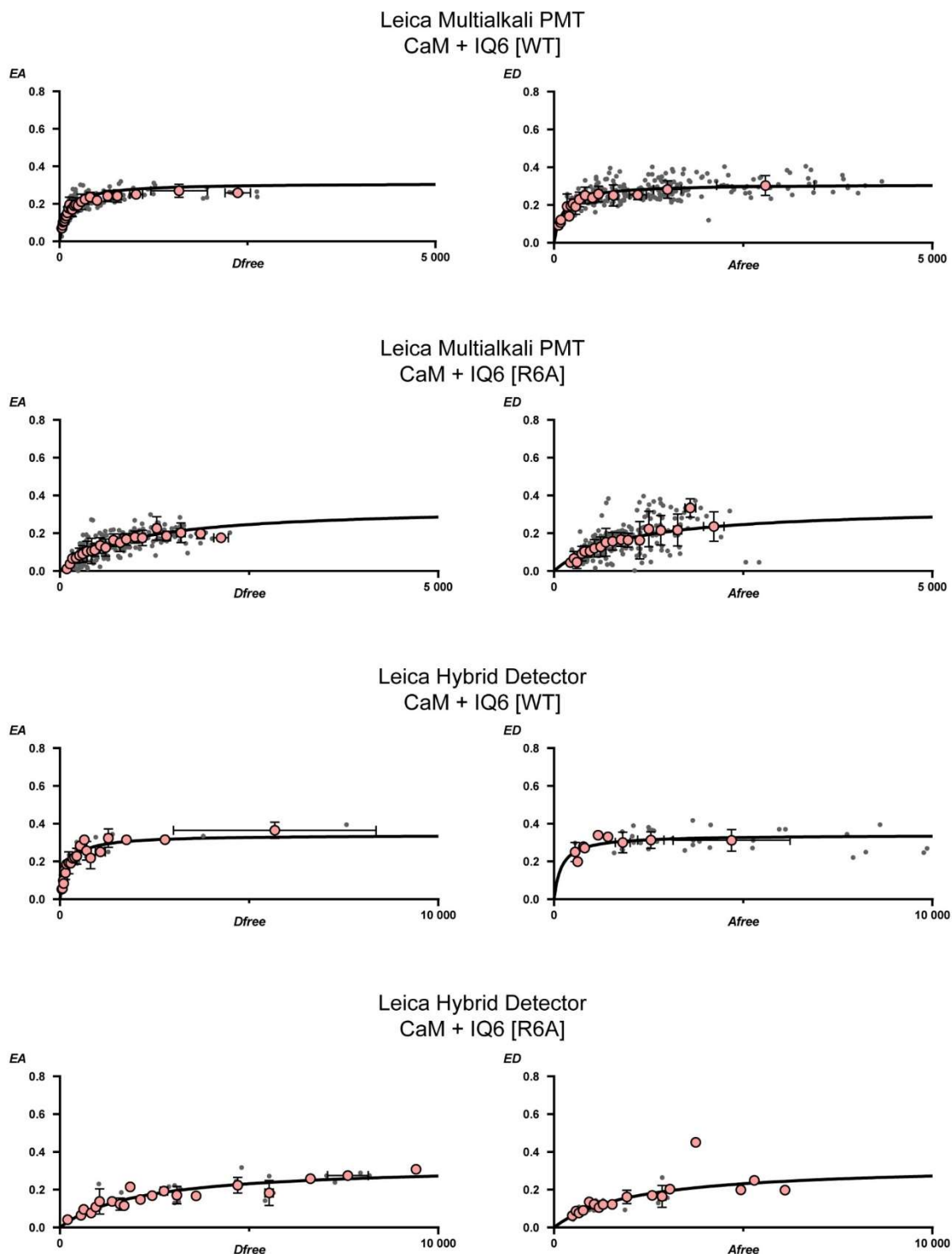


Figure 29: Analysis of protein binding affinities using the confocal image-based Two-Hybrid FRET assay on both Leica SP8 configurations. The analysis of the protein interaction CaM with the [WT]-IQ6 and [R6A]-IQ6 mutant was compared under two conditions to assess the reliability of the assay: The Leica GaAsP PMT measurements were conducted using a GaAsP PMT, different excitation lasers different excitation wavelengths compared to the Zeiss LSM980 shown in Figure 25. Additionally, the detection range for all channels was changed. The Leica HyD (Hybrid Detector) measurements were conducted using Hybrid Detectors, which are working differently compared to GaAsP PMTs and further alternated detection range properties in all channels. Data are shown for both Leica SP8 instruments for each interaction ([WT]-IQ6 and [R6A]-IQ6) and can be compared additionally to the Zeiss LSM980 in Figure 25. Grey dots represent manually drawn ROIs that were evaluated using the ImageJ

macro shown in Figure 19. Light red circles represent XY-binned data. One transfection stoichiometry was used for each interaction (1: 1 μg of donor:acceptor).

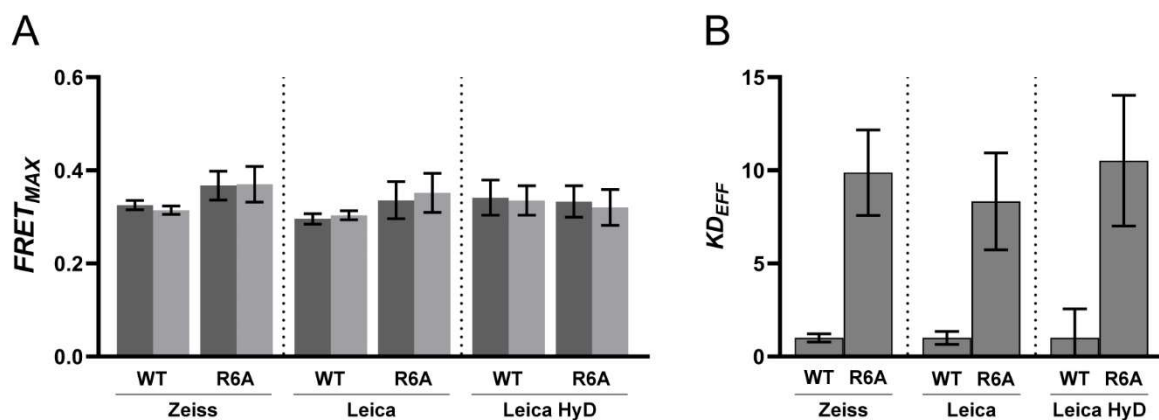


Figure 30: Comparison of binding curve parameter from measurements on CaM with IQ6 [WT] or IQ6 [R6A] using different confocal instruments. A, The maximum FRET efficiency from binding curves shown for CaM with IQ6 [WT] and [R6A] using the Zeiss confocal microscope (Figure 25) and Leica measurements (Figure 29) are shown. Dark grey columns show $E_{A,max}$ values, light grey columns show $E_{D,max}$ values for each mutant. The maximum FRET efficiency is displayed in percent. Error bars represent the 95 % CI of the binding curve fit for the $FRET_{max}$ value. **B,** The K_D value is displayed for both the [WT]-IQ6 and [R6A]-IQ6 mutant. All values are normalized to the [WT]-IQ6 with a K_D of 1. Error bars represent the 95 % CI of the binding curve fit for the K_D value.

Model for the interaction between CaM and [R6A]-IQ6

To visualize the interaction between CaM and [R6A]-IQ6, the 3D structures of CaM and the IQ6 motif from *Gallus gallus*⁴¹ (Figure 31 A; PDB ID: 2DFS) and additionally CaM with IQ1 and IQ2 motifs from *Mus musculus*⁹³ (Figure 31 B; PDB ID: 2IX7) are displayed. CaM wraps around the helical IQ motif but does not fully enclose it. This binding itself is calcium-independent, as the structures shown display only apo-CaM. The sidechain of the arginine in position 6 is located just at the opening site of a bound CaM (Figure 31 A, left panel). Notably, the [R6A]-IQ6 mutation points directly upwards in this binding, akin to a fingertip when a hand encloses around an object (IQ6 motif, Figure 31 A). This utmost part of CaM forms a small pocket for the arginine sidechain and displays a high polarity as shown in the hydrophobicity display in Figure 31 A in the right panel: The arginine occupies a CaM pocket and is surrounded by polar residues, likely enhancing binding through ionic bonds.

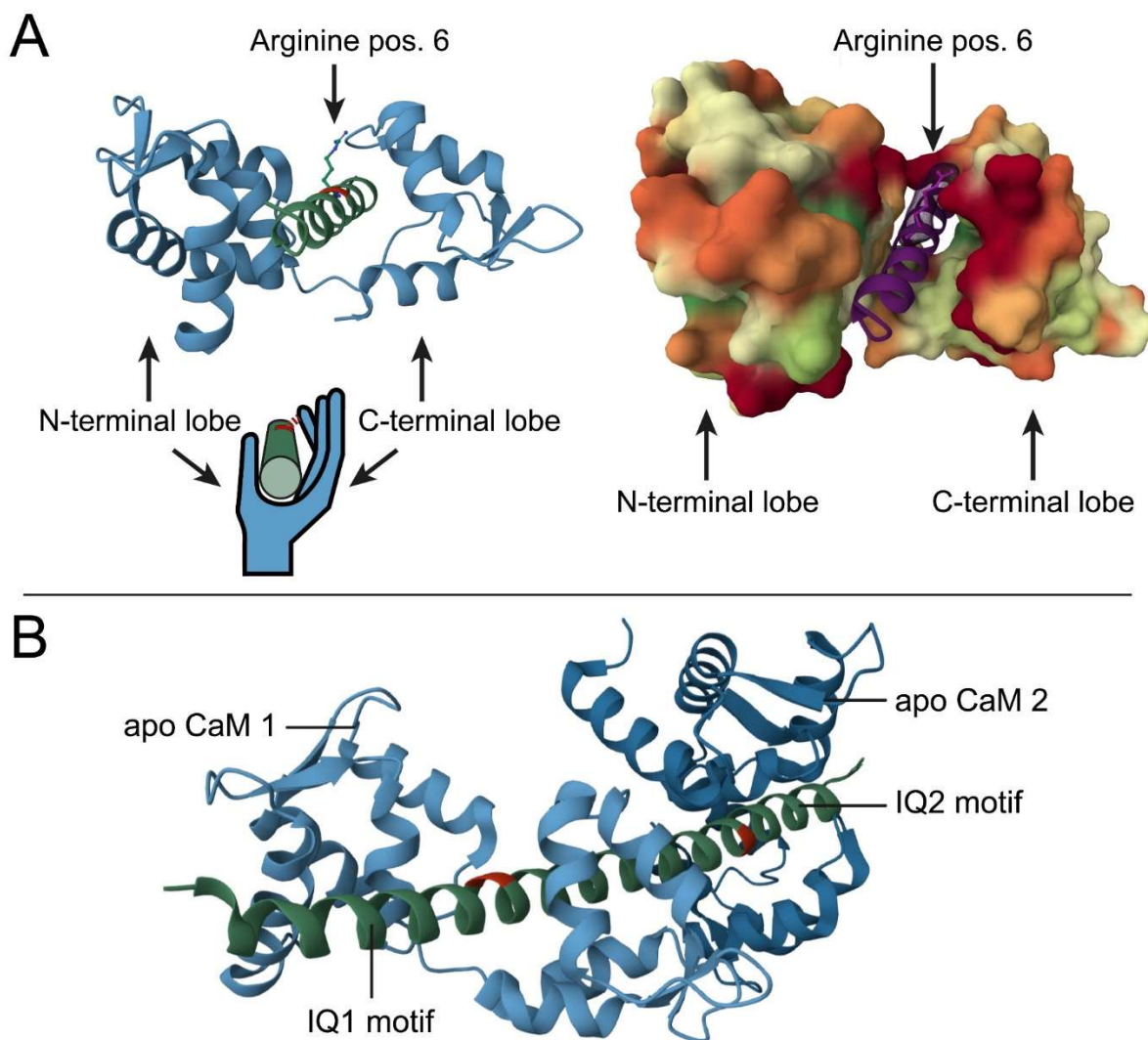


Figure 31: Structure of the mutated IQ motif bound to CaM **A**, The left image displays the structure of the IQ6 motif (green) from *G. gallus* with bound CaM obtained via cryo-electron microscopy⁴¹ (PDB ID: 2DFS). The CaM is shown in blue, indicating the left and right lobes. The IQ6 motif is displayed in green with the Arginine at position 6 highlighted. The backbone of the arginine is displayed, indicated by the upper black arrow. The cartoon below the x-ray structure emphasizes the similarity of a grabbing hand (representing the CaM) that closes around a green stick (representing the IQ motif). The position of the Arginine displayed above is highlighted in red, interacting with the finger (red dotted line). On the right, the same structure is shown using a hydrophobic surface representation for the CaM protein. Hydrophobic areas are indicated in green, hydrophilic areas in red. The IQ6 motif is shown in dark violet, with the R6 sidechain highlighted. It sits directly in a hydrophilic pocket of CaM (black arrow). **B**, Two different IQ motifs, derived from the *Mus musculus* structure of myosinVa bound to CaM are displayed. These structures were obtained by X-ray crystallography⁹³ (PDB ID: 2IX7). Color coding is similar to A. The IQ1 and IQ2 motifs are indicated and their respective conserved R6 amino acids are highlighted in red. Each motif binds one CaM protein, which are indicated as apo CaM 1 and 2. Both of these CaM – IQ bindings show an identical orientation of the R6 amino acid as shown in A, facing outward of the claw formation of CaM.

5.6 Aim 6 – Subcellular Two-Hybrid FRET analysis of endolysosomal proteins

The results obtained so far have shown that the confocal image-based Two-Hybrid FRET assay is performing with high fidelity on different microscope configurations with high precision and reliable acquisition of the binding curve parameter K_D and $FRET_{max}$. More importantly, this technique is reliable and accurate for investigating FRET signals at subcellular resolution. Therefore, this method is applied to investigate protein-protein interactions between the Rab GTPases Rab5 and Rab7 with the endolysosomal cation channels TPC1, TPC2 and TRPML1-3. Two large interactome studies of TPC channels^{83,84} revealed numerous candidates which potentially interact with TPC1 and/or TPC2, including the Rab-GTPases Rab5 and Rab7.

The putative interaction between Rab7 and TPC2 on late endosomes is the focus in aim 6 and will be investigated first and in most detail: An expression analysis of both proteins is carried out that is followed by confocal Two-Hybrid FRET assays. These FRET assays will include the two mutants ([Q67L] and [T22N]) that were described before. Then, Rab7 will be also investigated with TPC1 to analyze if Rab7 interacts vesicle-specific or not.

Then, the interaction of the early endosomal Rab5 and TPC1 or TPC2 will be tested.

Additional experiments are conducted to see if Rab7 interacts with other ion channels that reside on late endosomes and belong to the TRPML family. Lastly, an isoform of Rab7, named Rab7B, is investigated with TPC1, TPC2 and TRPML1.

5.6.1 Co-localization of Rab7a and TPC2

In Figure 32 A, the expression of TPC2 is shown in co-expression with a cytosolic marker. Super-resolution microscopy using the AiryScan technique on the Zeiss LSM980 confocal microscope revealed that TPC2 localizes at endolysosomal vesicles. Vesicles vary in size ranging from under 100 nm to 200 nm in diameter. Large vesicles in direct focus appear like circles or hollow dots, smaller vesicles are bright, sharp dots. Vesicles outside of the focused Z-plane are displayed as green dots with decreasing sharpness. In Figure 32 B confocal images of HEK293t cells co-expressing Rab7 with TPC2 with (right) and without (left) pretreatment by apilimod are shown. The expression profile of the Rab7 protein is partially cytosolic and mostly vesicular. Rab7 and TPC2 co-localize well at vesicles. Rab7 and TPC2 positive vesicles are

slightly shifted with respect to each other due to chromatic aberration. Due to standard confocal imaging, the resolution of the vesicles is lower compared to vesicles shown in super-resolution (Figure 32 A and B) and thus are visible only as bright dots. The treatment of cells with apilimod results in enlarged vesicles up to 4 μm in diameter. The vesicles are formed irregularly. Luminal areas of vesicles are completely devoid of fluorescence signals and replace cytosolic space almost entirely. The co-localization between Rab7 and TPC2 remains similar compared to cells without apilimod pretreatment. The amount Rab7 and TPC2 are different among individual vesicles. However, almost all vesicles display pronounced fluorescence signals corresponding to both proteins.

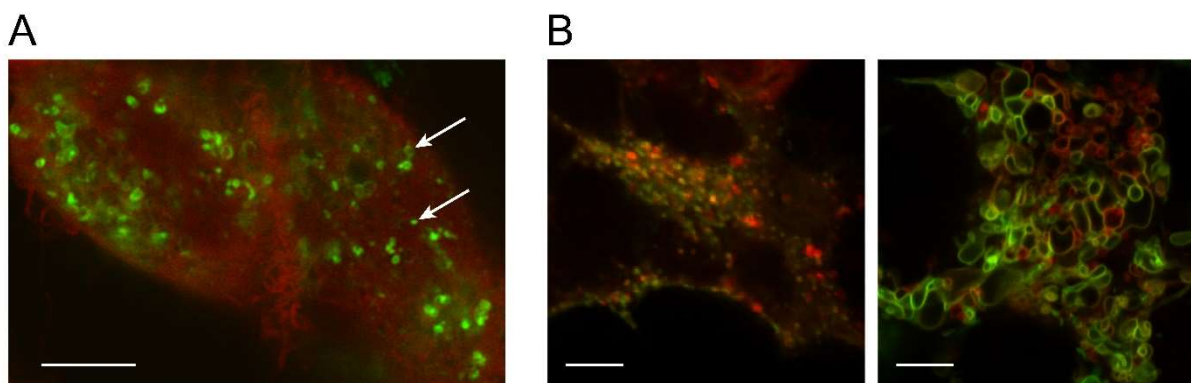


Figure 32: Heterologous expression of TPC2 (A, B) and Rab7 (B) in HEK293t cells. A, Super-resolution fluorescence imaging using the AiryScan technique on a Zeiss confocal microscope: A cytosolic expression marker is shown in red (mTq2). Heterologous expression of TPC2-mVen is displayed in green. White arrows indicate TPC2 positive vesicles. B, Standard confocal imaging showing co-expression of Rab7 with TPC2 without (left) and with apilimod (right). Red: Rab7, green: TPC2. Scale bars: 5 μm .

5.6.2 Functional analysis of Rab7a wildtype and mutants with TPC2

As described before, active Rab7 is GTP bound and contains an exposed geranylgeranyl anchor that attaches the protein to vesicular membranes. The inactive Rab7 binds GDP and the geranylgeranyl anchor is protected by GDI, which prevents insertion to vesicular membranes and leads to cytosolic localization. Consequently, Rab7 is expected to be localized partially at vesicles (active Rab7) and partially in the cytosol (inactive Rab7) depending on its state. The Rab7 [Q67L] mutant is expected to localize at vesicular membranes only (locked in active state), and the Rab7 [T22N] mutant is expected to be cytosolic only (locked in inactive state). The localization of the wildtype and both mutants is shown Figure 33.

The Rab7 wildtype displays both endolysosomal and cytosolic localization. The Rab7 [Q67L] mutant is localized at vesicular membranes, and the [T22N] mutant is found mostly in the cytosol. These findings correspond well to the proposed functions of the wildtype and mutants of Rab7⁹⁴⁻⁹⁶.

The images were further transformed using the 2D mapping of images into color coded donor-centric FRET efficiencies (E_D) in Figure 33 C. FRET signals are evident in the wildtype only at membranes of vesicular structures and vary between vesicles, reaching from low FRET values up to almost 35 % FRET. FRET values for the Rab7 [Q67L] mutant reach up to 40 % FRET efficiency at vesicular membranes. The [T22N] mutant exhibits low FRET efficiencies (up to 15 %), confined to membranes of vesicles, indicating that some co-localization remains intact in this mutant. The FRET imaging in the images fits well to the proposed mechanism of these mutants and their corresponding expression profiles.

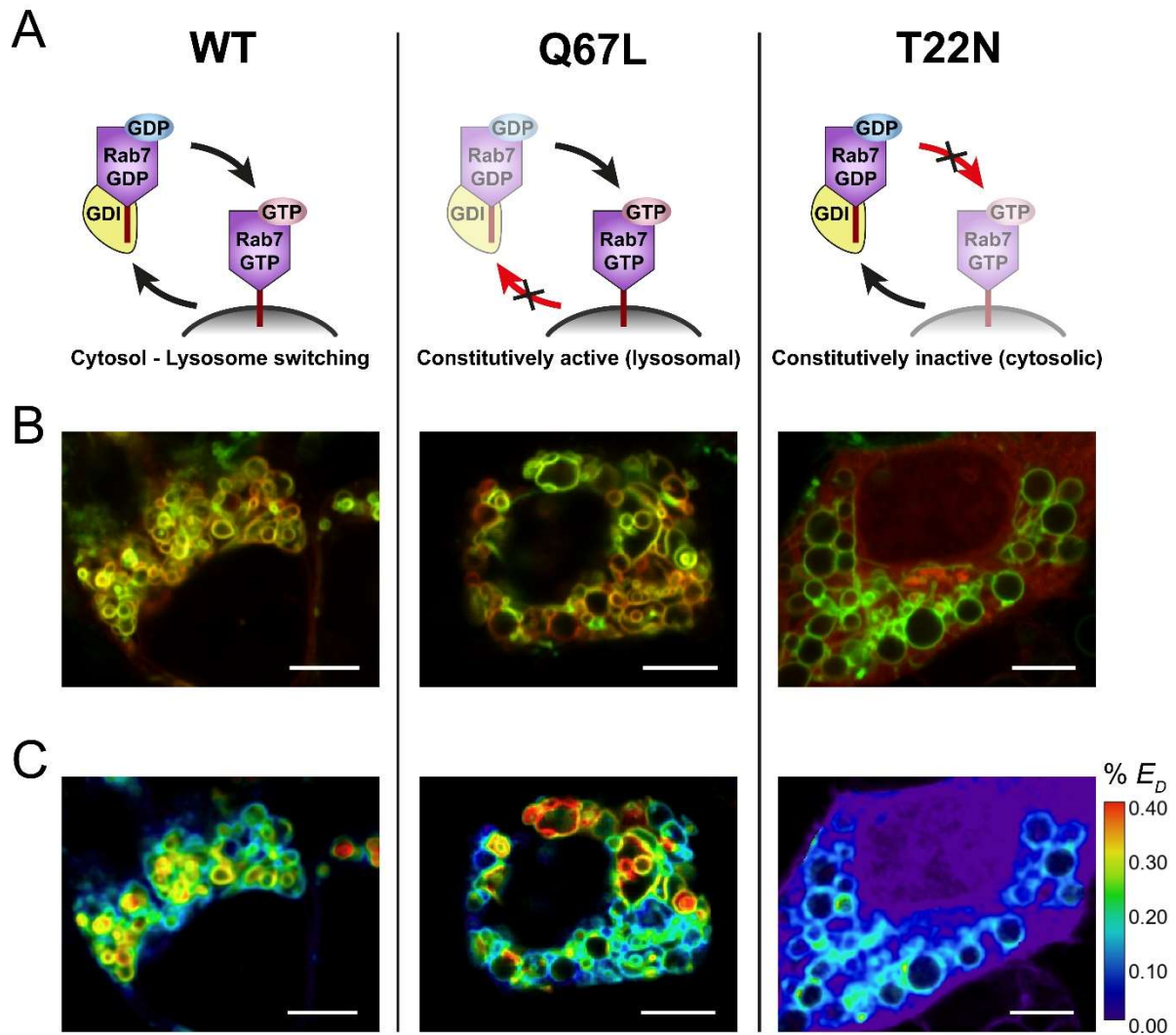


Figure 33: Protein interaction mechanism between Rab7 and TPC2 **A**, Schematic view of the functioning of Rab7 wildtype (left panel), Rab7 [Q67L] (central panel) and Rab7 [T22N] (right panel): The wildtype is in an inactive state, bound to the GDI and GDP. Upon interaction with a GEF (Figure 8 A), the GDP is exchanged for GTP and the GDI dissociates. Consequently, the Rab7 will be integrated into a vesicular membrane and is considered to be in its active state. This process is reversible when the intrinsic GTPase activity (and GAP) hydrolyses GTP to GDP, leading to the association of GDI in the cytosol, rendering the Rab7 inactive. The Rab7 [Q67L] mutant is impaired in its GTPase activity, thus the protein arrests in its active, GTP-bound state (central panel). The Rab7 [T22N] mutant is unable to bind GTP, thus not able to change into its active, GTP-bound state (right panel) **B**, Rab7 wildtype (green, left panel), Rab7 [Q67L] (green, central panel) and Rab7 [T22N] (green, right panel) were co-expressed with TPC2 (red) in HEK293T. Cells were treated with 1 μ M apilimod for 16 h. Scale bars: 5 μ m. TPC2 is exclusively localized in vesicles. The Rab7 wildtype is vesicular and partially cytosolic (left panel). Rab7a [Q67L] is localized only on vesicular membranes (central panel), and Rab7a [T22N] displays mostly cytosolic expression (right panel). **C**, 2D mapping of color-coded donor-centric FRET efficiency (E_D), corresponding to the upper images: Left panel shows E_D values of the Rab7 wildtype co-expressed with TPC2, central panel shows E_D values of the Rab7 [Q67L] mutant with TPC2, and the right panel displays E_D values of the Rab7 [T22N] mutant with TPC2. Each pixel was calculated in terms of donor FRET efficiency (E_D) and alpha blending was applied to the absolute brightness of the pixels, similar to Figure 20. The FRET efficiency (E_D) is color-coded corresponding to the legend on the right. Scale bars: 5 μ m. Images of Rab7 wildtype and Rab7a [Q67L] co-expressed with TPC2 show high FRET efficiencies at vesicular membranes, while the [T22N] mutant only displays low FRET efficiencies (< 15 %) in similar regions. Cytosolic regions display no FRET signals in all variants.

5.6.3 Two-Hybrid FRET binding curves of Rab7a with TPC2

The confocal image-based Two-Hybrid FRET assay was used for all data shown (Figure 34). The interaction between Rab7 wildtype and TPC2 without the pretreatment of apilimod was investigated in the upmost two binding curves. Images were taken on a confocal microscope by co-expressing Rab7 with TPC2. Regions of interests were drawn from bright dots indicating Rab7 and TPC2 positive vesicles. Data points align well to the binding curve fit. Both binding curves are covered with a FRET maximum of 35 % for both $E_{A,max}$ and $E_{D,max}$. In the lower six diagrams, apilimod was applied to the cells after transfection in order to enlarge vesicles (late endosomes and lysosomes)^{97,98}. Regions of interests were drawn in bright vesicular membrane regions, which are displayed in Figure 33 C and D for each mutant. The amount of data points is higher for binding curves with apilimod pretreatment compared to the upmost two diagrams, which show the wildtype interaction without the apilimod pretreatment. The maximum FRET efficiency derived from the binding curve with apilimod pretreatment is approximately 5 % higher (40 %) compared to the same interaction without apilimod (35 %, upmost two diagrams). Data for the mutants were acquired similarly using apilimod. The [Q67L] mutant displays slightly higher maximum FRET efficiencies compared to the Rab7 wildtype interaction with TPC2 (up to 43 %). The relative K_D between the wildtype and [Q67L] interaction with TPC2 is comparable (Rab7 [Q67L] $K_D = 1.33x$), indicating no difference in binding affinity to TPC2. The Rab7 [T22N] mutant with TPC2 displays a much lower maximum FRET value of 15 % for both $E_{A,max}$ and $E_{D,max}$. The binding curves correspond well to FRET efficiencies acquired from 2D mapping of E_D for these interactions, which are displayed in Figure 33 D. However, due to its much lower maximum FRET efficiency, the [T22N] mutant cannot be compared confidently in terms of binding affinity.

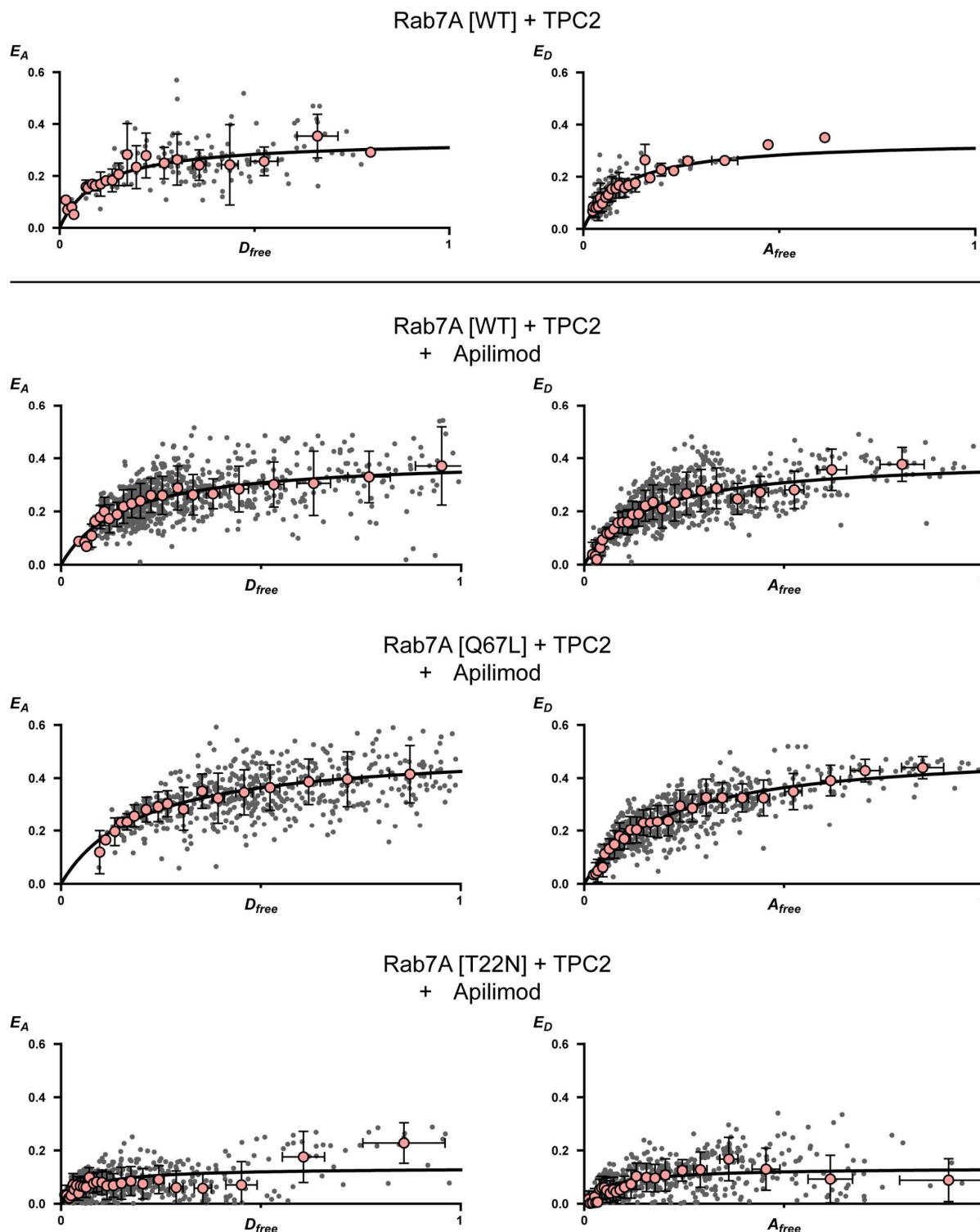


Figure 34: Confocal image-based Two-Hybrid FRET of Rab7a with TPC2. The upmost two diagrams display the binding curves (E_A and E_D) for Rab7 wildtype with TPC2 without applying apilimod. Below, the binding curves of the Rab7a wildtype, [Q67L] and [T22N] mutants with TPC2 are shown after apilimod treatment (16 h incubation of 1 μ M). Grey dots represent manually drawn ROIs that were evaluated using the ImageJ macro shown in Figure 19. Light red circles represent XY-binned data. D_{free} and A_{free} values are normalized identically and thus comparable for all diagrams shown. The Rab7a wildtype and [Q67L] mutant with TPC2 reach maximum FRET efficiencies of 40 % and 43%, for both E_A and E_D , respectively. The Rab7a [T22N] with TPC2 binding curves display significantly lower FRET efficiencies, reaching approximately 13 % for both $E_{A,max}$ and $E_{D,max}$. Two different stoichiometries were used for each interaction (2:1, 1:2 μ g for donor:acceptor).

5.6.4 Two-Hybrid FRET binding curves of Rab7 with TPC1

Next the interaction of Rab7 with TPC1 was investigated (Figure 35). Images were taken on a confocal microscope by co-expressing Rab7 with TPC1. Regions of interests were drawn from bright dots indicating Rab7 or TPC1 positive vesicles: Fluorescence signals in vesicles were mostly different between Rab7 and TPC1 due to a lower overall co-localization. Both binding curves are covered with data points and display an accurate fit. The maximum FRET efficiency is very low for both E_A and E_D with only 4 %.

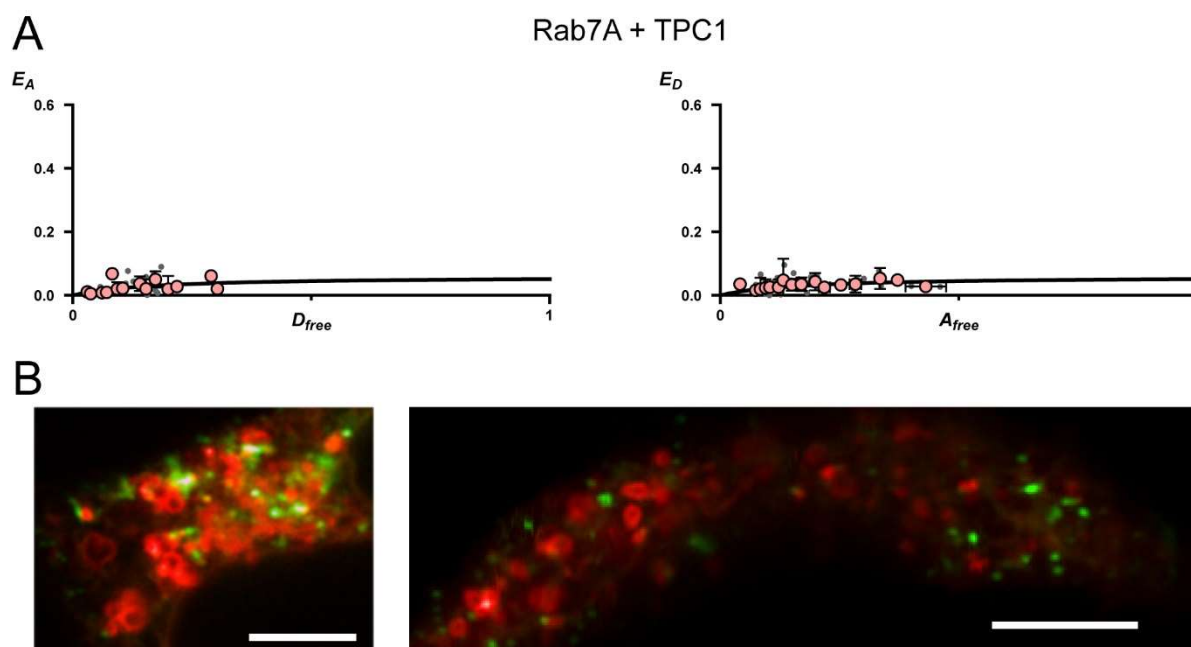


Figure 35: Confocal image-based Two-Hybrid FRET of Rab7 with TPC1. **A**, Two-Hybrid FRET binding curves. Grey dots represent manually drawn ROIs that were evaluated using the ImageJ macro shown in Figure 19. Light red circles represent XY-binned data. D_{free} and A_{free} values are normalized identically to Figure 34. Both binding curves result in very low maximum FRET efficiencies for both E_A and E_D (< 5 %). Two different stoichiometries were used (2:1, 1:2 μg for donor:acceptor). **B**, Confocal images of Rab7a in co-expression with TPC1. Scale bar: 5 μm .

5.6.5 Two-Hybrid FRET binding curve of Rab5 with TPC1

To investigate Rab5 with TPC1, cells were used co-expressing both proteins. The confocal Two-Hybrid FRET assay was used to investigate FRET signals. Bright dots of Rab5 and TPC1 positive vesicles were selected for analysis. As displayed in Figure 37 B, both proteins co-localize well, as Rab5 positive vesicles contain large amounts of TPC1. In contrast to the Rab5 + TPC2 binding curves, the binding curves of Rab5 with TPC1 are well covered, especially at higher X-values, and show moderate FRET efficiencies in both binding curves, with a maximum FRET efficiency of 22 % for both E_A and E_D .

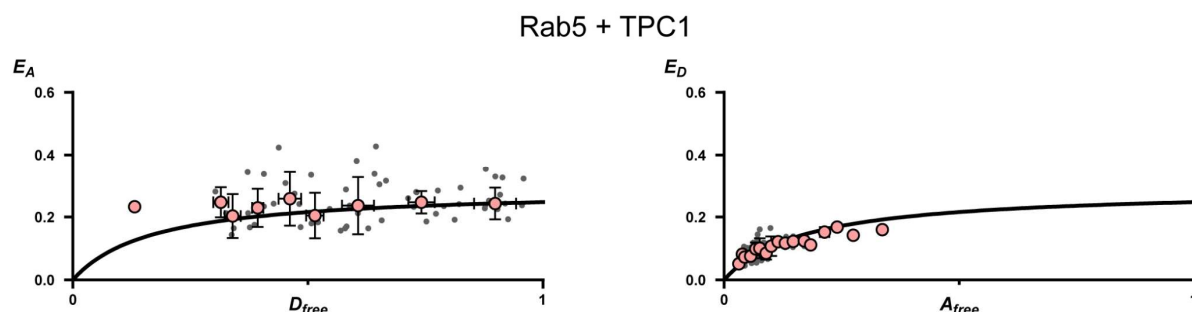


Figure 36: Confocal image-based Two-Hybrid FRET of Rab5 with TPC1. Grey dots represent manually drawn ROIs that were evaluated using the ImageJ macro shown in Figure 19. Light red circles represent XY-binned data. D_{free} and A_{free} values are normalized identically and thus comparable for all diagrams shown. The E_A binding curve is well saturated and the fit displays a maximum FRET value of around 24 % for both E_A and E_D . Two different stoichiometries were used for each interaction (2:1, 1:2 μg for donor:acceptor).

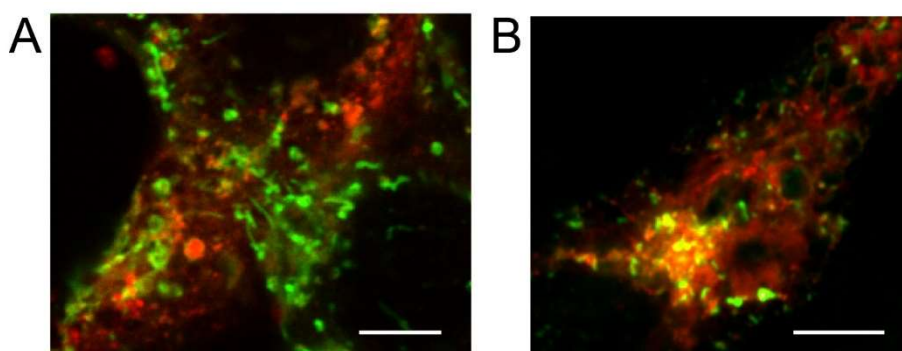


Figure 37: Confocal images of Rab5 with TPC2 and TPC1. A, TPC2 (green) co-expressed with Rab5 (red). B, TPC1 (green) co-expressed with Rab5 (red). Scalebar: 5 μm . Images acquired using standard confocal microscopy.

5.6.6 Two-Hybrid FRET binding curves of Rab7 with TRPML1-3

Our results revealed that FRET efficiencies for the interaction between Rab7 and TPC2 were rather high, indicating a potential interaction between these proteins. This raised the possibility that Rab7 could also interact with other endolysosomal cation channels, such as TRPML1⁹⁹, TRPML2¹⁰⁰ and TRPML3¹⁰¹. This was tested in the following three experiments.

Rab7 + TRPML1: Images were taken on a confocal microscope by co-expressing Rab7 and TRPML1 and shown in Figure 39 A. Regions of interests were drawn from bright dots indicating Rab7 and TRPML1 positive vesicles. TRPML1 has a predominantly late endosomal/lysosomal expression profile⁹⁹. The binding curves of TRPML1 and Rab7 show high FRET signals up to approximately 40 %. However, the binding curves do not display a proper saturation point, indicating that the estimated maximum FRET value from the fit is higher than the FRET data obtained. Data points align to the fit for both binding curves, but E_A FRET values seem to be consistently higher (40 % FRET) with significant more scattering of data points around the fit. The E_D binding curve data show up to 30 % FRET in contrast to the E_D fit.

Rab7 + TRPML2: The FRET analysis was conducted using confocal images of cells co-expressing Rab7 with TRPML2. Regions of interests were drawn from bright dots indicating Rab7 and TRPML2 positive vesicles. Binding curves are well covered and show very low FRET signals up to 9 %. The data points align well to the fit, with very low error values, especially in terms of the E_D binding curve.

Rab7 + TRPML3: FRET analysis was done by using confocal images of cells co-expressing Rab7 with TRPML3. Binding curves display similarly low FRET values compared to binding curves measured with Rab7 and TRPML2. The binding curves are covered and display low FRET values for both E_A and E_D .

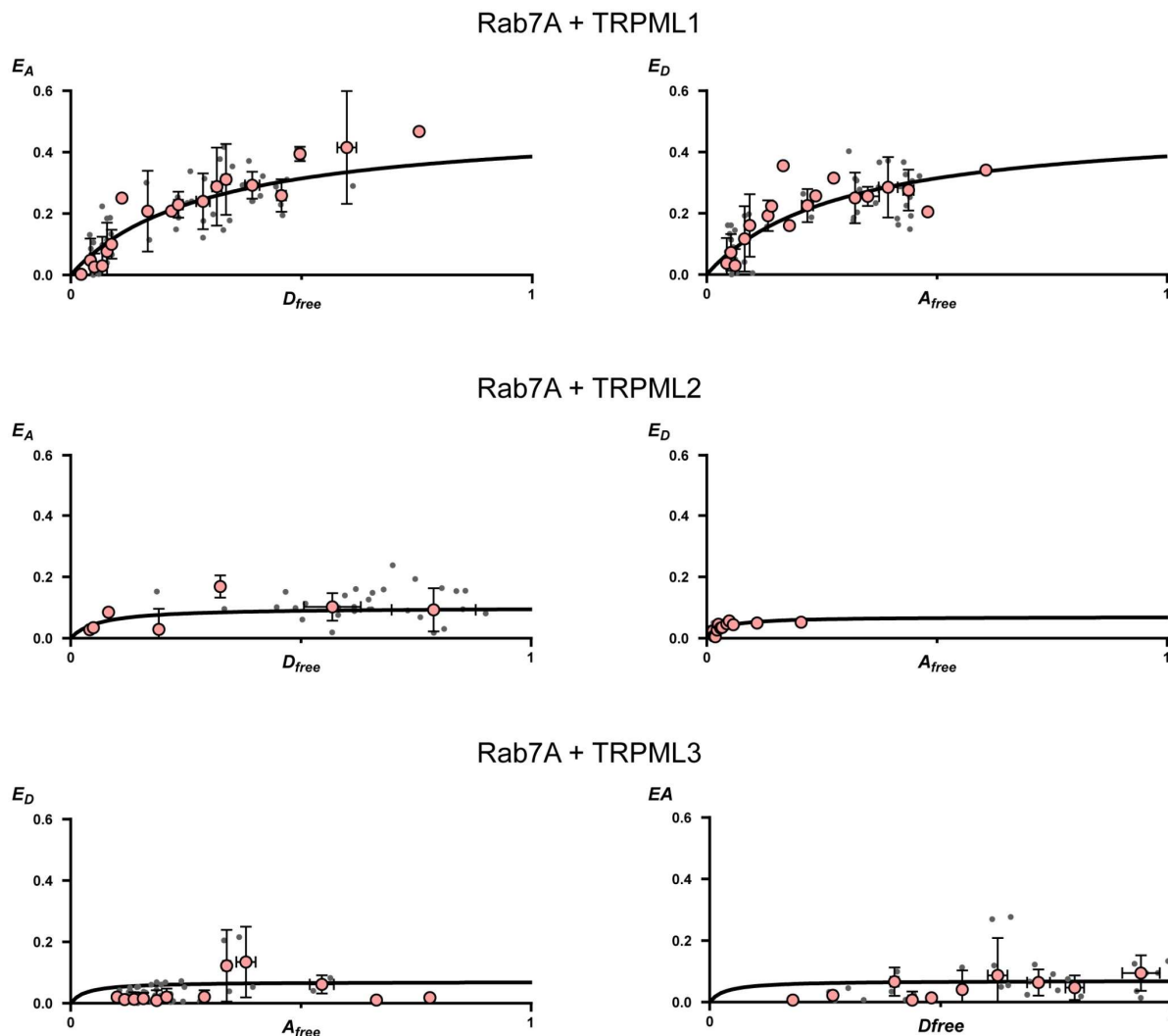


Figure 38: Confocal image-based Two-Hybrid FRET of Rab7 with TRPML1-3. Grey dots represent manually drawn ROIs that were evaluated using the ImageJ macro shown in Figure 19. Light red circles represent XY-binned data. D_{free} and A_{free} values are normalized identically and thus comparable for all diagrams shown. FRET efficiencies for the TRPML1 interaction reach values up to 40 % (E_A), but the curve does not reach a saturation point, thus not displaying a distinct maximum FRET efficiency in the fit. TRPML2 and TRPML3 with Rab7a display low FRET efficiencies, which stay low in higher FRET partner abundance, thus resulting in low maximum FRET efficiencies for both E_A and E_D (< 5 %). Two different stoichiometries were used for each interaction (2:1, 1:2 μg for donor:acceptor).

The interaction of Rab7 and TRPML1 was further investigated by co-localization and 2D mapping of E_A and E_D as described before. Very bright, Rab7-positive vesicles co-localize with bright TRPML1-positive vesicles. Exceptionally high FRET values are evident in confined vesicular regions within cells (Figure 39 B). FRET signals between vesicles differ from low FRET values (15 %) up to high values (40 %). Cytosolic regions display FRET signals below 15 %.

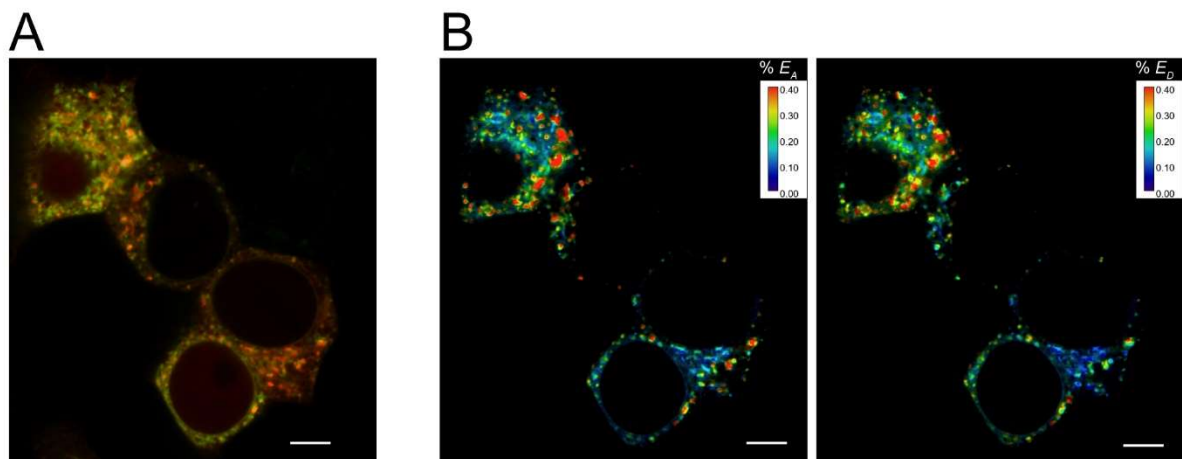


Figure 39: Expression and Two-Hybrid FRET imaging of Rab7a with TRPML1. **A**, Composite image of the heterologous co-expression of Rab7 (red) and TRPML1 (green) in HEK293T cells. Scale Bar: 5 μm . **B**, 2D mapping of color-coded FRET efficiencies E_A and E_D of the image in A for both FRET efficiencies, E_A and E_D . The FRET efficiency legend is shown in the top right-hand corner in each image. Scale bars: 5 μm .

5.6.7 Two-Hybrid FRET binding curves of Rab7B with TPC2, TRPML1 and TPC1

Rab7B is a splice variant of Rab7 that is expressed in humans. It localizes slightly different compared to Rab7A (referred to as Rab7), targeting the TGN and late endosomes^{102,103}. Because Rab7 displayed strong FRET signals with ion channels that co-localize well at late endosomes (TPC2 and TRPML1), also the interaction between Rab7B and TPC2, TRPML1 and TPC1 (negative control) was investigated.

In Figure 41, the co-localization of Rab7B and TPC2, TRPML1 or TPC1 is displayed by using confocal microscopy and co-expression of corresponding proteins.

Rab7B + TPC2: Binding curves and derived parameters calculated for the interaction of Rab7B and TPC2 are similar to the binding curves of Rab7 with TPC2 (Figure 34 for Rab7a, Figure 40 for Rab7B). The E_D binding curve is well covered with data points with a maximum FRET efficiency of 25 %. Data align well to the fit and both proteins co-localize well (Figure 41 A).

Rab7B + TRPML1: Binding curves of Rab7B and TRPML1 display in lower FRET signals compared to the analysis of Rab7a with TRPML1. Both binding curves are covered with data points covering the FRET maximum, which results in a fit with a FRET maximum of 22 % and very low scattering of data points around the fit. In contrast to Rab7a, a saturation point in the binding curves could be reached experimentally for Rab7B with TRPML1. Both proteins co-localize well (Figure 41)

Rab7B + TPC1: Binding curves are covered worse compared to Rab7a with TPC1, but both interactions display similarly low FRET efficiencies. Further, Rab7B and TPC1 do not co-localize (Figure 41).

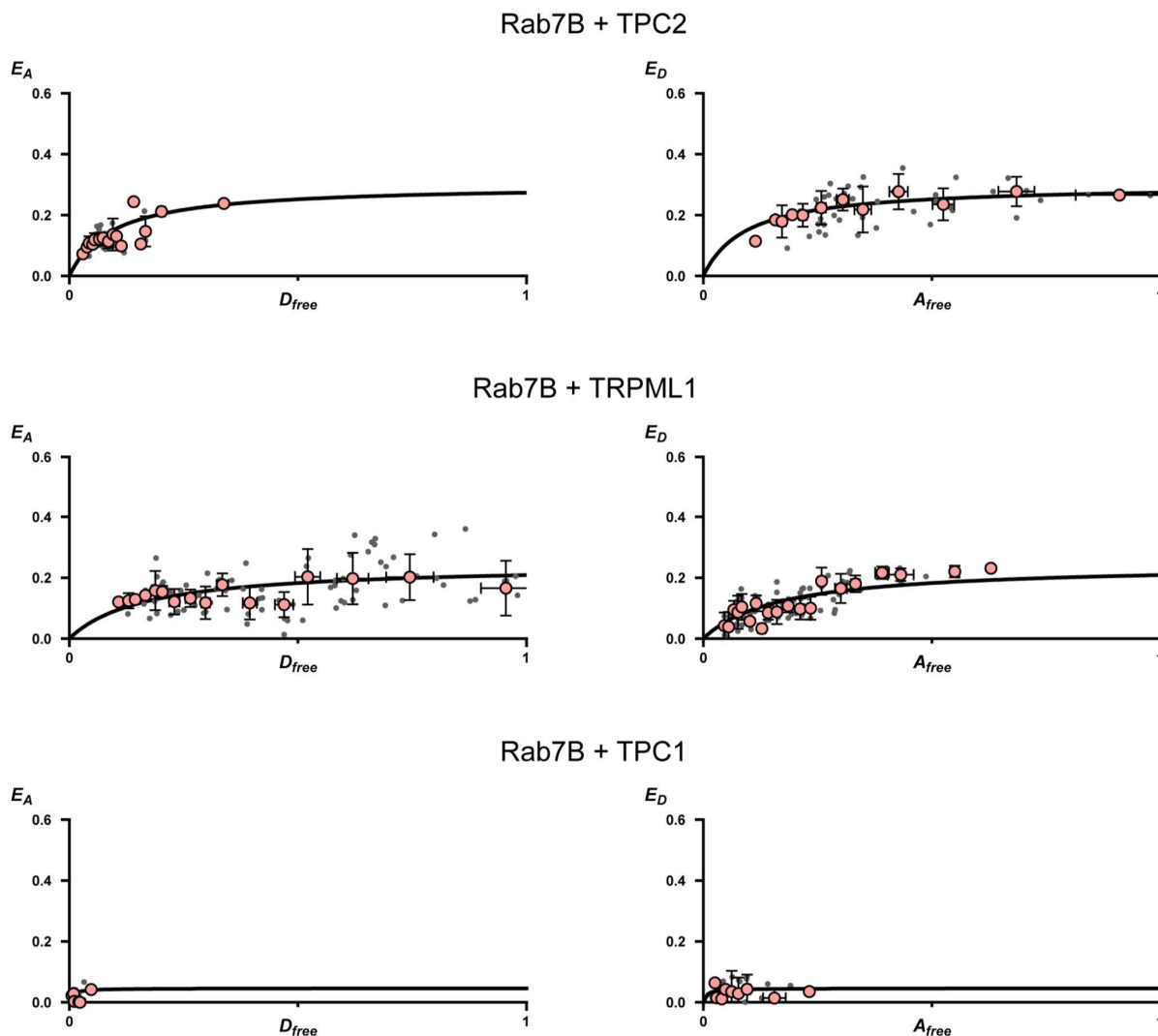


Figure 40: Confocal image-based Two-Hybrid FRET of Rab7B with TPC2, TRPML1 or TPC1. Grey dots represent manually drawn ROIs that were evaluated using the ImageJ macro shown in Figure 19. Light red circles represent XY-binned data. The binding curves of Rab7B with TPC2 result in very similar data compared to Rab7A with TPC2 (Figure 34) reaching a maximum FRET efficiency of approximately 30 % for both E_A and E_D . The binding curves of Rab7B with TRPML1 result in significantly lower FRET efficiencies compared to Rab7A with TRPML1. In contrast, the binding curves displayed are better covered and the maximum FRET efficiency is deductible at approximately 22 % for both E_A and E_D . The binding curves of Rab7B with TPC1 display very low FRET signals, comparable to Rab7A with TPC1 as shown in Figure 35. Two different stoichiometries were used for each interaction (2:1, 1:2 μg for donor:acceptor).

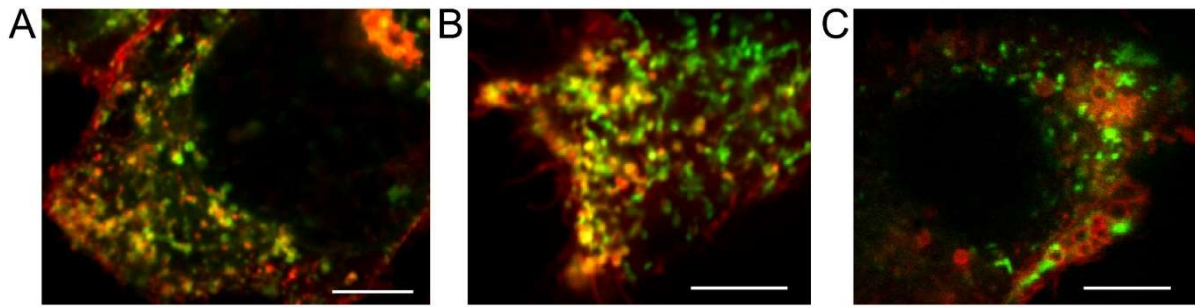


Figure 41: Confocal images of Rab7B with TPC2, TRPML1 and TPC1. **A**, TPC2 (green) co-expressed with Rab7B (red). **B**, TRPML1 (green) co-expressed with Rab7B (red). **C**, TPC1 (green) co-expressed with Rab7B. Scalebar: 5 μ m. Images acquired using standard confocal microscopy.

6 Discussion

Part I: Two-Hybrid FRET

The main achievements in part I are related to the development of the Two-Hybrid FRET assay on four different FRET setups, each with specific experimental indications. The Two-Hybrid FRET Method could be substantially improved in terms of reliability and fidelity, which is discussed in the first section by using a photometry setup (aim 1). With these improvements at hand, the Two-Hybrid FRET assay was established on a flow cytometer (aim 2). Further, two novel, image-based Two-Hybrid FRET assays were developed: A high-throughput, image-based assay was developed using an imaging plate reader (aim 3) and a high-fidelity, image-based assay on a confocal laser scanning microscope (aim 4). Importantly, each device used has its own specific strengths that are discussed in the following sections.

6.1 Improvements to the Two-Hybrid FRET assay

Using a highly efficient FRET pair

The use of a more potent FRET pair (mTurquoise2 and mVenus) that replaces the previously used CFP and YFP fluorophores¹ improves the assay in multiple ways: Both fluorophores have higher quantum yields^{91,92}, which gives rise to higher brightness compared to CFP and YFP. This results in a better signal-to-noise ratio for proteins that are expressed at low levels.

Further, this FRET pair has an improved dynamic range due to a 23 % increased Förster distance compared to ECFP/EYFP (equation 3⁸⁸⁻⁹²), which leads to a greater amplitude of donor quenching and sensitized emission and therefore more precise FRET quantification: Consequently, FRET signals when using the new fluorophore pair are 75 % greater (35 % $FRET_{max}$) compared to the ECFP/EYFP data (20 % $FRET_{max}$, Figure 12 A). The new FRET pair is also less prone to protonation or de-protonation during measurement, as both fluorophores have pK_a values that are lower compared to their ECFP/EYFP counterparts. A change in protonation can change the spectral properties, which negatively impacts FRET measurements¹⁰⁴.

Design of new FRET calibration constructs

The second improvement is the development of optimized FRET calibration constructs (dimers, Figure 4). The FRET calibration constants (G_{ratio} and F_{ratio}) are critical for the robustness of the method, as they have great influence on the reliable estimation of the binding parameters K_D and E_{max} (equations 20-27). A reliable assessment of both G_{ratio} and F_{ratio} is only given when each dimer used for FRET calibration yields identical FRET efficiencies for E_A (sensitized emission) and E_D (donor quenching), as shown in Figure 4 B. Further, it is critical that the FRET efficiencies between all three dimers employed are well separated: This is necessary, because the G_{ratio} and F_{ratio} are derived from a linear regression of dimer data as shown in Figure 4 C. The larger the range of FRET efficiencies between the dimers, the better the regression line becomes, and the more robust the G_{ratio} and F_{ratio} are.

Previously used dimers¹ had a very low range of FRET efficiencies ranging from 12 % to 30 %¹ FRET, which resulted in an unstable regression line and variations when deriving G_{ratio} and F_{ratio} . The novel dimers were designed to increase the range of FRET efficiencies and consequently yield a more stable linear regression line: They range from <5% to 56 % FRET efficiency (D2A = <5 %, D42 = 30 %, D3 = 56 %, Figure 10 A). This increased the dynamic range for FRET calibration by 177 %. With this improvement, the determination of the G_{ratio} and F_{ratio} became stable over several months. Consequently, binding curve parameter could be reliably compared between protein interactions which were measured on different days.

Development of a standardized fitting procedure

The third improvement to the Two-Hybrid FRET technique is the new matlab FRET evaluation software, which was created by Manu Ben-Johny (Columbia University, Medical Center) and

extended by me and Dr. Michael Schänzler (Hanover Medical School). The new analysis software allows for data evaluation compatibility across the different FRET setups used. Secondly, it features an automatic fitting procedure that eliminates the need for manual fitting by the investigator. Thirdly, the filtering of data by brightness to exclude measurements below certain thresholds, which is especially crucial for the flow cytometer, as this instrument has a poor fidelity in terms of fluorescence quantification at low intensity signals.

6.2 Establishment and validation of the Two-Hybrid FRET assay on four devices

Validation on the photometry setup

By using the reference protein interaction of CaM and the IQ6 domain from myosinVa, the improvements to the assay discussed in the previous section were compared to published data that did not employ these improvements on a similar photometry setup. This revealed that the FRET maxima E_A and E_D increased from 20% up to 35 % (Figure 12). This change is based on the increased Förster distance (R_0) of the new FRET pair, which leads to increased FRET signals at a given proximity between fluorophores. Increasing the Förster distance also reduces the false negative rate of FRET assays, as it allows for detecting FRET signals that are otherwise too small to be detected.

Flow cytometer based Two-Hybrid FRET

To overcome the large amount of time required for data acquisition by the photometry setup FRET assay, a flow cytometry based Two-Hybrid FRET assay was established as a high-throughput version. The measurement speed (more than 5000 data points per binding curve in under one hour) and the coverage of binding curves is highly improved when using a flow cytometer Two-Hybrid FRET assay (Figure 13). However, flow cytometers measure cells in a flowing stream with short acquisition time, which limits the accuracy for fluorescence quantification. Due to this, binding curves data scatter significantly more compared to the photometry assay. The scattering effect is amplified for low intensity fluorescence signals (low estimated D_{free} or A_{free} values, Figure 13). This problem is of greater importance for the K_D estimation and will be discussed in a later section. The flow cytometer Two-Hybrid FRET assay is best suited for high-throughput applications that focus on determining maximum FRET values only.

Image-based Two-Hybrid FRET

An image-based Two-Hybrid FRET method was developed to combine the fidelity of the photometry-based assay and the high-throughput nature of the flow-cytometer. Previously published Two-Hybrid FRET assays were conducted either on a photometry setup¹, or a flow cytometer^{23,24}, thus the image-based method is a new approach to conduct Two-Hybrid FRET measurements. The image-based approach uses complete images (i_{CFP} , i_{FRET} , i_{YFP}) that are transformed into FRET binding curves; therefore FRET data can be correlated directly to the images they are derived from. To achieve a high throughput of measurements, an optical plate reader is employed which allows the imaging of multiple wells in a single run, creating more sample images (> 20) in a short (15-30 min.) measurement session. The developed automatic cell detection (Figure 15) is a highly flexible tool that shortens the evaluation time. The training process allows not only for the detection of cells (pixel classifier), but also includes a second step, which serves as a quality control for detected objects (object classifier), therefore leading to the high data quality that is comparable to measurements conducted using a photometry setup (Figure 17). This assay combines the speed of the flow-cytometer assay with the accuracy from the photometry-based assay. However, the plate-reader based Two-Hybrid FRET assay is similar to the other Two-Hybrid FRET assays limited to whole-cell FRET analysis.

Confocal image-based Two-Hybrid FRET

The image-based confocal Two-Hybrid FRET assay was developed to enable FRET evaluation from subcellular regions. This is a major success, as in previous publications significant difficulties have been reported that precluded robust FRET quantification on confocal microscopes¹⁰⁵.

Due to the manual drawing of ROIs within cells, the confocal assay is more time consuming than the image-based plate-reader assay. However, binding curves can be evaluated with outstanding precision (Figure 20), because undesired regions that negatively impact the FRET quantification, such as nuclei or vesicle (Figure 19), can be excluded from FRET evaluation. Another advantage is the ability to cover binding curves completely without the need to transfect multiple stoichiometries of donor:acceptor samples. This can be attributed to the non-uniform distribution of donor and acceptor FRET partners within a cell, which results in more diverse FRET scenarios within one sample. Further, fluorescence quantification is precise

for a wide range of fluorescence intensities, including very low intensities, which allows the investigation of poorly expressed proteins.

In addition to its subcellular binding curve analysis, the confocal image-based technique can be modified to transform high-resolution confocal images into color-coded 2D maps of FRET efficiencies (Figure 21). This application is particularly helpful when subcellular regions are investigated that display distinct FRET efficiencies (Figure 33). The calculation for the 2D mapping of E_A and E_D is described in equation 17 and 18. The 2D mapping only displays FRET efficiencies and no binding affinities.

Part II: Proteins used in Two-Hybrid FRET assays

The most powerful feature of the Two-Hybrid FRET method is the possibility to quantitatively determine protein-protein binding affinities. In the following this important property of the method will be discussed for the binding mechanism of the IQ6-domain of myosinVa and CaM (aim 5), which is a protein-protein interaction that occurs within the cytosolic compartment of the cell. In addition, subcellular FRET measurements of small regulatory Rab GTPases with endolysosomal cation channels are discussed (aim 6).

6.3 Mutation of the IQ6 motif to alter its binding affinity to CaM

In Part I it could be validated that absolute FRET efficiencies can be reliably determined on any presented instrument by using the reference protein interaction of CaM with the IQ6 binding domain from myosinVa. However, to characterize unknown protein-protein interactions also in terms of their relative binding affinity, an additional reference IQ6 – CaM protein interaction with a decreased binding affinity needs to be created, so that both interactions can be compared against each other.

From all IQ6 mutants, only R6A-IQ6 exhibited a reduced binding affinity to CaM. This observation was consistent throughout all instruments used for screening; thus this mutant was selected for the reference system.

The ability to measure a decreased K_D for the R6A-IQ6 mutant consistently using the confocal image-based Two-Hybrid FRET assay could be validated by using three different instruments, as the decrease in binding affinity was similar on all devices (Figure 29 and Figure 30). The decreased binding affinity of the R6A-IQ6 mutant can be explained due to an easier dissociation of CaM from the IQ helix, because CaM is not sufficiently stabilized around the the opening site due to the loss of the polar arginine residue in the mutant (Figure 31 A).

6.4 Analysis of protein interactions in the endolysosomal system

The development of an image-based confocal Two-Hybrid FRET assay allows for the investigation of protein-protein interactions in subcellular compartments such as the endolysosomal system. In particular, interactions between small regulatory Rab GTPases and ion channels within the endolysosomal system (TPC1, TPC2, TRPML1-3).

TPC2 and Rab7 protein expression

To analyze FRET from vesicles, these vesicles first need to be characterized by using a vesicular marker protein such as TPC2. For live cell standard confocal microscopy, the lateral resolution is limited to more than 200 nm and the axial resolution to more than 500 nm^{105,106}. However, vesicular structures are variable in size ranging from 20-200 nm in diameter and are therefore slightly below the resolution limit. TPC2 was co-expressed with Rab7 and visualized using standard confocal microscopy. Despite the limiting resolution, vesicles are visible as dots and the co-localization of TPC2 and Rab7 is evident (Figure 32 B). To increase the visibility of vesicular membranes without using super-resolution techniques, cells were pretreated with apilimod. This results in an improved visibility of vesicular membranes and protein co-localization (Figure 32 B). Additionally, the AiryScan super-resolution technique (Figure 32 A) was used for imaging (resulting in 140 nm lateral resolution and under 500 nm axial resolution). With this technique, non-enlarged vesicles shapes became visible, but this technique could not be used for FRET assays due to the post-processing of absolute intensity values within the image.

2D FRET maps of Rab7 mutants with TPC2

The 2D color-coded FRET maps (Figure 33 C) reveal that FRET efficiencies vary significantly along vesicular membranes in both the wildtype and [Q67L] Rab7 mutant. This is in line with the co-expression analysis of Rab7 and TPC2 when pretreated with apilimod (Figure 32 B), which indicates highly variable concentrations of both proteins along vesicle membranes. In conclusion, the Rab7 mutants display expected results in both co-expression and 2D FRET maps according to their mode of actions.

Rab7 and TPC2 Two-Hybrid FRET

The 2D FRET maps revealed FRET signals between Rab7 and TPC2 at vesicular membranes. To understand if these signals occur because of an underlying protein binding interaction, the confocal image-based Two-Hybrid FRET assay was used: If binding curves display data that fit to a slope and a FRET maximum (saturation point), an interaction can be assumed due to the presence of a measurable binding affinity (K_D value). Apilimod does not influence binding behavior, as the interaction was also measured without apilimod pretreatment which resulted in similar binding curves. However, utilizing apilimod markedly enlarges the region of interest, allowing for clearer spatial resolution of vesicular membranes and a more refined FRET assessment specific to these regions (Figure 34, 2nd from top). Most importantly, binding curves display a distinct saturation point, indicating a protein binding affinity instead of a FRET signal that would arise due to accumulating proteins.

The localization between the wildtype and Rab7 [Q67L] mutant have shown to be similar (Figure 33 B). Given that the Rab7 [Q67L] mutant functions identical to the active state of the wildtype, the binding parameter should be comparable as well: The slightly higher FRET maximum (40 %) and similar relative K_D ($[QL] = 1.3x K_D$) of the Rab7 [Q67L] mutant compared to the wildtype interaction is in line with these expectations.

The low FRET signals (15 %, Figure 34) of the Rab7 [T22N] mutant are in line with the 2D FRET map (Figure 33 C) and its proposed function, because the majority of Rab7 [T22N] is localized in the cytosol, while TPC2 is at vesicular membranes. The K_D cannot be compared, as this mutant has a significant lower $FRET_{max}$ value accompanied by a less robust fit.

Rab7 and TPC1 Two-Hybrid FRET

It is plausible to assume that the TPC1 channel and the Rab7 GTPase co-localize during endosome maturation⁷⁵, even though TPC1 is predominantly present at early endosomes and not late endosomes. Indeed, both proteins have shown to co-localize on some occasions (Figure 35 B). The binding curves shown in Figure 35 A indicate that, even if both proteins co-localize, they likely do not interact: Binding curves display good coverage, which underlines that proteins co-localize on vesicular membranes (refer to Figure 5). However, the lack of any FRET signals along the binding curves provides strong evidence that these proteins do not come in close proximity for a protein-protein binding to occur. Further, these data support the

argument that collisional FRET signals are negligible due to the absence of FRET signals even at higher protein concentrations along the x-axis of the binding curves.

Rab5 and TPC1 Two-Hybrid FRET

Rab5 and TPC1 yield FRET signals (22 %) in binding curves with a clear saturation point, underlining that this is a FRET signal caused by binding reaction.

The main conclusions derived from Two-Hybrid FRET experiments of Rab5 or Rab7 with TPC1 or TPC2 are that small Rab-GTPases interact with ion-channels, but in a vesicle-dependent manner: Early and late-endosomes contain specific ion-channels (TPC1 and TPC2, respectively), that are regulated via specific Rab-GTPases, namely Rab5 for early endosomes (TPC1), and Rab7 for late endosomes (TPC2).

Rab7 and TRPML1-3 Two-Hybrid FRET

The interaction of ion channels of the TRPML family and Rab7 was tested to investigate if Rab7 has additional interaction partners at late endosomes besides TPC2. TRPML1 is predominantly present in lysosomes and early lysosomes¹⁰⁷ and although binding curves reach very high FRET values (Figure 38), they do not contain data points that indicate a FRET saturation at higher protein concentrations (X-axis values). This indicates that measurements could be accompanied by protein aggregation artifacts. Further, Rab7 was measured with TRPML2, which also resides at late-endosomes and early-lysosomes¹⁰⁰, as well as TRPML3, which can potentially localize at late-endosomes or early-lysosomes, but mainly localizes in the ER¹⁰¹. There were no FRET signals observed between Rab7 and TRPML2 or TRPML3, indicating no interaction.

Rab7B and TPC1, TPC2 and TRPML1 Two-Hybrid FRET

Rab7A (in this work referred to as Rab7) and Rab7B share an amino acid sequence identity of 50 % and an amino acid sequence similarity of 69 %. Rab7B is only 8 amino acids shorter than Rab7A. Both proteins are proposed to have similar functions but with slightly different localization^{102,103,108}. Thus, it is plausible that Rab7B interacts similar to Rab7A with endosomal channel proteins, such as TPC2, TRPML1 and TPC1. Indeed, the results are strikingly similar. Importantly, the binding curves of Rab7B with TRPML1 (Figure 40) are more convincing compared to the Rab7A data, due to the presence of saturation point of FRET efficiencies (Figure 40). This finding underlines that there is an interaction between Rab7A or Rab7B and TRPML1.

7 References

1. Butz, E.S., Ben-Johny, M., Shen, M., Yang, P.S., Sang, L., Biel, M., Yue, D.T., and Wahl-Schott, C. (2016). Quantifying macromolecular interactions in living cells using FRET two-hybrid assays. *Nature protocols* *11*, 2470-2498.
2. Förster, T. (1946). Energiewanderung und fluoreszenz. *Naturwissenschaften* *33*, 166-175.
3. Förster, T. (1947). Ein beitrag zur theorie der photosynthese. *Zeitschrift für Naturforschung B* *2*, 174-182.
4. Förster, T. (1949). Experimentelle und theoretische Untersuchung des zwischenmolekularen Übergangs von Elektronenanregungsenergie. *Zeitschrift für naturforschung A* *4*, 321-327.
5. Kleppner, D. (1999). A short history of atomic physics in the twentieth century. *Reviews of Modern Physics* *71*, S78.
6. Sun, Y., Wallrabe, H., Seo, S.A., and Periasamy, A. (2011). FRET microscopy in 2010: the legacy of Theodor Förster on the 100th anniversary of his birth. *Chemphyschem* *12*, 462-474.
7. Medintz, I.L., and Hildebrandt, N. (2013). FRET-Förster Resonance Energy Transfer: From Theory to Applications (John Wiley & Sons).
8. Algar, W.R., Hildebrandt, N., Vogel, S.S., and Medintz, I.L. (2019). FRET as a biomolecular research tool—understanding its potential while avoiding pitfalls. *Nature methods* *16*, 815-829.
9. Grecco, H.E., and Verveer, P.J. (2011). FRET in cell biology: still shining in the age of super-resolution? *ChemPhysChem* *12*, 484-490.
10. Lauterbach, M.A. (2012). Finding, defining and breaking the diffraction barrier in microscopy—a historical perspective. *Optical nanoscopy* *1*, 1-8.
11. Zeug, A., Woehler, A., Neher, E., and Ponimaskin, E.G. (2012). Quantitative intensity-based FRET approaches—a comparative snapshot. *Biophysical journal* *103*, 1821-1827.
12. Kenworthy, A.K. (2001). Imaging protein-protein interactions using fluorescence resonance energy transfer microscopy. *Methods* *24*, 289-296.
13. Preus, S., and Wilhelmsson, L.M. (2012). Advances in quantitative FRET-based methods for studying nucleic acids. *ChemBioChem* *13*, 1990-2001.
14. Terai, K., Imanishi, A., Li, C., and Matsuda, M. (2019). Two decades of genetically encoded biosensors based on Förster resonance energy transfer. *Cell structure and function* *44*, 153-169.
15. Zheng, J. (2010). FRET and its biological application as a molecular ruler. In *Biomedical applications of biophysics*, (Springer), pp. 119-136.
16. Padilla-Parra, S., Auduge, N., Coppey-Moisan, M., and Tramier, M. (2011). Non fitting based FRET-FLIM analysis approaches applied to quantify protein-protein interactions in live cells. *Biophysical Reviews* *3*, 63-70.
17. Fruhwirth, G.O., Fernandes, L.P., Weitsman, G., Patel, G., Kelleher, M., Lawler, K., Brock, A., Poland, S.P., Matthews, D.R., and Kéri, G. (2011). How Förster resonance energy transfer imaging improves the understanding of protein interaction networks in cancer biology. *ChemPhysChem* *12*, 442-461.
18. Wlodarczyk, J., Woehler, A., Kobe, F., Ponimaskin, E., Zeug, A., and Neher, E. (2008). Analysis of FRET signals in the presence of free donors and acceptors. *Biophysical journal* *94*, 986-1000.
19. Ben-Johny, M., Yue, D.N., and Yue, D.T. (2016). Detecting stoichiometry of macromolecular complexes in live cells using FRET. *Nature communications* *7*, 13709.
20. Ben-Johny, M., and Yue, D.T. (2014). Calmodulin regulation (calmodulation) of voltage-gated calcium channels. *Journal of General Physiology* *143*, 679-692.
21. Erickson, M.G., Liang, H., Mori, M.X., and Yue, D.T. (2003). FRET two-hybrid mapping reveals function and location of L-type Ca²⁺ channel CaM preassociation. *Neuron* *39*, 97-107.

22. Chen, H., Puhl III, H.L., and Ikeda, S.R. (2007). Estimating protein-protein interaction affinity in living cells using quantitative Förster resonance energy transfer measurements. *Journal of biomedical optics* 12, 054011-054011-054019.
23. Liu, G., Papa, A., Katchman, A.N., Zakharov, S.I., Roybal, D., Hennessey, J.A., Kushner, J., Yang, L., Chen, B.-X., and Kushnir, A. (2020). Mechanism of adrenergic CaV1. 2 stimulation revealed by proximity proteomics. *Nature* 577, 695-700.
24. Lee, S.-R., Sang, L., and Yue, D.T. (2016). Uncovering aberrant mutant PKA function with flow cytometric FRET. *Cell reports* 14, 3019-3029.
25. Liao, J.-y., Song, Y., and Liu, Y. (2015). A new trend to determine biochemical parameters by quantitative FRET assays. *Acta Pharmacologica Sinica* 36, 1408-1415.
26. Padilla-Parra, S., and Tramier, M. (2012). FRET microscopy in the living cell: different approaches, strengths and weaknesses. *Bioessays* 34, 369-376.
27. Zimmermann, T. (2005). Spectral imaging and linear unmixing in light microscopy. *Microscopy Techniques: -/-*, 245-265.
28. Shimozono, S., and Miyawaki, A. (2008). Engineering FRET constructs using CFP and YFP. *Methods in cell biology* 85, 381-393.
29. Rivas, S., Hanif, K., Chakouri, N., and Ben-Johny, M. (2021). Probing ion channel macromolecular interactions using fluorescence resonance energy transfer. In *Methods in enzymology*, (Elsevier), pp. 319-347.
30. Erickson, M.G., Moon, D.L., and Yue, D.T. (2003). DsRed as a potential FRET partner with CFP and GFP. *Biophysical Journal* 85, 599-611.
31. Friedberg, F., and Rhoads, A.R. (2001). Evolutionary aspects of calmodulin. *IUBMB life* 51, 215-221.
32. Tidow, H., and Nissen, P. (2013). Structural diversity of calmodulin binding to its target sites. *The FEBS journal* 280, 5551-5565.
33. Bähler, M., and Rhoads, A. (2002). Calmodulin signaling via the IQ motif. *FEBS letters* 513, 107-113.
34. Fili, N., and Toseland, C.P. (2019). Unconventional myosins: how regulation meets function. *International journal of molecular sciences* 21, 67.
35. Desnos, C., Huet, S., and Darchen, F. (2007). 'Should I stay or should I go?': myosin V function in organelle trafficking. *Biology of the Cell* 99, 411-423.
36. Seabra, M.C., and Coudrier, E. (2004). Rab GTPases and myosin motors in organelle motility. *Traffic* 5, 393-399.
37. Langford, G.M. (2002). Myosin-V, a versatile motor for short-range vesicle transport. *Traffic* 3, 859-865.
38. Trybus, K.M. (2008). Myosin V from head to tail. *Cellular and Molecular Life Sciences* 65, 1378-1389.
39. Van Gele, M., Dynoodt, P., and Lambert, J. (2009). Griscelli syndrome: a model system to study vesicular trafficking. *Pigment cell & melanoma research* 22, 268-282.
40. Tyska, M.J., and Warshaw, D.M. (2002). The myosin power stroke. *Cell motility and the cytoskeleton* 51, 1-15.
41. Liu, J., Taylor, D.W., Kremetsova, E.B., Trybus, K.M., and Taylor, K.A. (2006). Three-dimensional structure of the myosin V inhibited state by cryoelectron tomography. *Nature* 442, 208-211.
42. Yu, F.H., Yarov-Yarovoy, V., Gutman, G.A., and Catterall, W.A. (2005). Overview of molecular relationships in the voltage-gated ion channel superfamily. *Pharmacol Rev* 57, 387-395. 10.1124/pr.57.4.13.
43. Patel, S., Yuan, Y., Chen, C.-C., Jašlan, D., Gunaratne, G., Grimm, C., Rahman, T., and Marchant, J.S. (2022). Electrophysiology of endolysosomal two-pore channels: A current account. *Cells* 11, 2368.
44. Patel, S. (2015). Function and dysfunction of two-pore channels. *Science signaling* 8, re7-re7.

45. Jašlan, D., Böck, J., Krogsaeter, E., and Grimm, C. (2020). Evolutionary aspects of TRPMLs and TPCs. *International Journal of Molecular Sciences* *21*, 4181.
46. Grimm, C., Chen, C.-C., Wahl-Schott, C., and Biel, M. (2017). Two-pore channels: catalyzers of endolysosomal transport and function. *Frontiers in pharmacology* *8*, 45.
47. Krogsaeter, E.K., Biel, M., Wahl-Schott, C., and Grimm, C. (2019). The protein interaction networks of mucolipins and two-pore channels. *Biochimica et Biophysica Acta (BBA)-Molecular Cell Research* *1866*, 1111-1123.
48. Grimm, C., Chen, C.C., Wahl-Schott, C., and Biel, M. (2017). Two-Pore Channels: Catalyzers of Endolysosomal Transport and Function. *Front Pharmacol* *8*, 45. 10.3389/fphar.2017.00045.
49. Zhu, M.X., Ma, J., Parrington, J., Calcraft, P.J., Galione, A., and Evans, A.M. (2010). Calcium signaling via two-pore channels: local or global, that is the question. *American Journal of Physiology-Cell Physiology* *298*, C430-C441.
50. Grimm, C., Holdt, L.M., Chen, C.C., Hassan, S., Muller, C., Jors, S., Cuny, H., Kissing, S., Schroder, B., Butz, E., et al. (2014). High susceptibility to fatty liver disease in two-pore channel 2-deficient mice. *Nat Commun* *5*, 4699. 10.1038/ncomms5699.
51. Grimm, C., Butz, E., Chen, C.C., Wahl-Schott, C., and Biel, M. (2017). From mucopolidosis type IV to Ebola: TRPML and two-pore channels at the crossroads of endo-lysosomal trafficking and disease. *Cell Calcium* *67*, 148-155. 10.1016/j.ceca.2017.04.003.
52. Luzio, J.P., Parkinson, M.D., Gray, S.R., and Bright, N.A. (2009). The delivery of endocytosed cargo to lysosomes. *Biochemical Society Transactions* *37*, 1019-1021.
53. Jašlan, D., Ferro, I.F., Kudrina, V., Yuan, Y., Patel, S., and Grimm, C. (2023). PI (3, 5) P2 and NAADP: Team players or lone warriors?—New insights into TPC activation modes. *Cell Calcium* *109*, 102675.
54. Yamasaki, M., Masgrau, R., Morgan, A.J., Churchill, G.C., Patel, S., Ashcroft, S.J., and Galione, A. (2004). Organelle selection determines agonist-specific Ca²⁺ signals in pancreatic acinar and β cells. *Journal of Biological Chemistry* *279*, 7234-7240.
55. Masgrau, R., Churchill, G.C., Morgan, A.J., Ashcroft, S.J., and Galione, A. (2003). NAADP: a new second messenger for glucose-induced Ca²⁺ responses in clonal pancreatic β cells. *Current Biology* *13*, 247-251.
56. Zong, X., Schieder, M., Cuny, H., Fenske, S., Gruner, C., Rötzer, K., Griesbeck, O., Harz, H., Biel, M., and Wahl-Schott, C. (2009). The two-pore channel TPCN2 mediates NAADP-dependent Ca²⁺-release from lysosomal stores. *Pflügers Archiv-European Journal of Physiology* *458*, 891-899.
57. Beckers, C., and Balch, W. (1989). Calcium and GTP: essential components in vesicular trafficking between the endoplasmic reticulum and Golgi apparatus. *The Journal of cell biology* *108*, 1245-1256.
58. Mayorga, L.S., Beron, W., Sarrouf, M.N., Colombo, M.I., Creutz, C., and Stahl, P.D. (1994). Calcium-dependent fusion among endosomes. *Journal of Biological Chemistry* *269*, 30927-30934.
59. Ogunbayo, O.A., Duan, J., Xiong, J., Wang, Q., Feng, X., Ma, J., Zhu, M.X., and Evans, A.M. (2018). mTORC1 controls lysosomal Ca²⁺ release through the two-pore channel TPC2. *Science signaling* *11*, ea05775.
60. Zhang, J., Guan, X., Shah, K., and Yan, J. (2021). Lsm12 is an NAADP receptor and a two-pore channel regulatory protein required for calcium mobilization from acidic organelles. *Nature communications* *12*, 4739.
61. Wang, X., Zhang, X., Dong, X.-p., Samie, M., Li, X., Cheng, X., Goschka, A., Shen, D., Zhou, Y., and Harlow, J. (2012). TPC proteins are phosphoinositide-activated sodium-selective ion channels in endosomes and lysosomes. *Cell* *151*, 372-383.
62. Cang, C., Zhou, Y., Navarro, B., Seo, Y.-j., Aranda, K., Shi, L., Battaglia-Hsu, S., Nissim, I., Clapham, D.E., and Ren, D. (2013). mTOR regulates lysosomal ATP-sensitive two-pore Na⁺ channels to adapt to metabolic state. *Cell* *152*, 778-790.

63. Chao, Y.-K., Schludi, V., Chen, C.-C., Butz, E., Nguyen, O.P., Müller, M., Krüger, J., Kammerbauer, C., Ben-Johny, M., and Vollmar, A.M. (2017). TPC2 polymorphisms associated with a hair pigmentation phenotype in humans result in gain of channel function by independent mechanisms. *Proceedings of the National Academy of Sciences* *114*, E8595-E8602.
64. Wang, Q., Wang, Z., Wang, Y., Qi, Z., Bai, D., Wang, C., Chen, Y., Xu, W., Zhu, X., and Jeon, J. (2023). A gain-of-function TPC2 variant R210C increases affinity to PI (3, 5) P2 and causes lysosome acidification and hypopigmentation. *Nature Communications* *14*, 226.
65. Gerndt, S., Chen, C.-C., Chao, Y.-K., Yuan, Y., Burgstaller, S., Scotto Rosato, A., Krogsaeter, E., Urban, N., Jacob, K., and Nguyen, O.N.P. (2020). Agonist-mediated switching of ion selectivity in TPC2 differentially promotes lysosomal function. *Elife* *9*, e54712.
66. Scotto Rosato, A., Krogsaeter, E.K., Jašlan, D., Abrahamian, C., Montefusco, S., Soldati, C., Spix, B., Pizzo, M.T., Grieco, G., and Böck, J. (2022). TPC2 rescues lysosomal storage in mucopolidosis type IV, Niemann–Pick type C1, and Batten disease. *EMBO Molecular Medicine* *14*, e15377.
67. She, J., Zeng, W., Guo, J., Chen, Q., Bai, X.-c., and Jiang, Y. (2019). Structural mechanisms of phospholipid activation of the human TPC2 channel. *Elife* *8*, e45222.
68. Stenmark, H., and Olkkonen, V.M. (2001). The rab gtpase family. *Genome biology* *2*, 1-7.
69. Pylypenko, O., Hammich, H., Yu, I.-M., and Houdusse, A. (2018). Rab GTPases and their interacting protein partners: Structural insights into Rab functional diversity. *Small GTPases* *9*, 22-48.
70. Anant, J.S., Desnoyers, L., Machius, M., Demeler, B., Hansen, J.C., Westover, K.D., Deisenhofer, J., and Seabra, M.C. (1998). Mechanism of Rab geranylgeranylation: formation of the catalytic ternary complex. *Biochemistry* *37*, 12559-12568.
71. Stenmark, H. (2009). Rab GTPases as coordinators of vesicle traffic. *Nature reviews Molecular cell biology* *10*, 513-525.
72. Dirac-Svejstrup, A.B., Sumizawa, T., and Pfeffer, S.R. (1997). Identification of a GDI displacement factor that releases endosomal Rab GTPases from Rab–GDI. *The EMBO journal* *16*, 465-472.
73. Li, X., Garrity, A.G., and Xu, H. (2013). Regulation of membrane trafficking by signalling on endosomal and lysosomal membranes. *The Journal of physiology* *591*, 4389-4401.
74. Nordmann, M., Cabrera, M., Perz, A., Bröcker, C., Ostrowicz, C., Engelbrecht-Vandré, S., and Ungermann, C. (2010). The Mon1-Ccz1 complex is the GEF of the late endosomal Rab7 homolog Ypt7. *Current Biology* *20*, 1654-1659.
75. Borchers, A.-C., Janz, M., Schäfer, J.-H., Moeller, A., Kümmel, D., Paululat, A., Ungermann, C., and Langemeyer, L. (2023). Regulatory sites in the Mon1–Ccz1 complex control Rab5 to Rab7 transition and endosome maturation. *Proceedings of the National Academy of Sciences* *120*, e2303750120.
76. Wang, T., Ming, Z., Xiaochun, W., and Hong, W. (2011). Rab7: role of its protein interaction cascades in endo-lysosomal traffic. *Cellular signalling* *23*, 516-521.
77. Pfeffer, S., and Aivazian, D. (2004). Targeting Rab GTPases to distinct membrane compartments. *Nature reviews Molecular cell biology* *5*, 886-896.
78. Ullrich, O., Stenmark, H., Alexandrov, K., Huber, L.A., Kaibuchi, K., Sasaki, T., Takai, Y., and Zerial, M. (1993). Rab GDP dissociation inhibitor as a general regulator for the membrane association of rab proteins. *Journal of Biological Chemistry* *268*, 18143-18150.
79. Soldati, T., Shapiro, A.D., Dirac Svejstrup, A.B., and Pfeiffer, S.R. (1994). Membrane targeting of the small GTPase Rab9 is accompanied by nucleotide exchange. *Nature* *369*, 76-78.
80. Blümer, J., Rey, J., Dehmelt, L., Mazel, T., Wu, Y.-W., Bastiaens, P., Goody, R.S., and Itzen, A. (2013). RabGEFs are a major determinant for specific Rab membrane targeting. *Journal of Cell Biology* *200*, 287-300.
81. Wu, Y.-W., Oesterlin, L.K., Tan, K.-T., Waldmann, H., Alexandrov, K., and Goody, R.S. (2010). Membrane targeting mechanism of Rab GTPases elucidated by semisynthetic protein probes. *Nature chemical biology* *6*, 534-540.

82. Langemeyer, L., Fröhlich, F., and Ungermann, C. (2018). Rab GTPase function in endosome and lysosome biogenesis. *Trends in cell biology* *28*, 957-970.
83. Grimm, C., Holdt, L.M., Chen, C.-C., Hassan, S., Müller, C., Jörs, S., Cuny, H., Kissing, S., Schröder, B., and Butz, E. (2014). High susceptibility to fatty liver disease in two-pore channel 2-deficient mice. *Nature communications* *5*, 4699.
84. Lin-Moshier, Y., Keebler, M.V., Hooper, R., Boulware, M.J., Liu, X., Churamani, D., Abood, M.E., Walseth, T.F., Brailoiu, E., and Patel, S. (2014). The Two-pore channel (TPC) interactome unmasks isoform-specific roles for TPCs in endolysosomal morphology and cell pigmentation. *Proceedings of the National Academy of Sciences* *111*, 13087-13092.
85. McCray, B.A., Skordalakes, E., and Taylor, J.P. (2010). Disease mutations in Rab7 result in unregulated nucleotide exchange and inappropriate activation. *Human molecular genetics* *19*, 1033-1047.
86. Feldmann, C., Schänzler, M., Ben-Johny, M., and Wahl-Schott, C. (2023). Protocol for deriving proximity, affinity, and stoichiometry of protein interactions using image-based quantitative two-hybrid FRET. *STAR protocols* *4*, 102459.
87. Berg, S., Kutra, D., Kroeger, T., Straehle, C.N., Kausler, B.X., Haubold, C., Schiegg, M., Ales, J., Beier, T., and Rudy, M. (2019). Ilastik: interactive machine learning for (bio) image analysis. *Nature methods* *16*, 1226-1232.
88. Merola, F., Levy, B., Demachy, I., and Pasquier, H. (2010). Photophysics and spectroscopy of fluorophores in the green fluorescent protein family. *Advanced Fluorescence Reporters in Chemistry and Biology I: Fundamentals and Molecular Design*, 347-383.
89. Kremers, G.-J., Gilbert, S.G., Cranfill, P.J., Davidson, M.W., and Piston, D.W. (2011). Fluorescent proteins at a glance. *Journal of cell science* *124*, 157-160.
90. Heim, R., and Tsien, R.Y. (1996). Engineering green fluorescent protein for improved brightness, longer wavelengths and fluorescence resonance energy transfer. *Current biology* *6*, 178-182.
91. Kremers, G.-J., Goedhart, J., van Munster, E.B., and Gadella, T.W. (2006). Cyan and yellow super fluorescent proteins with improved brightness, protein folding, and FRET Förster radius. *Biochemistry* *45*, 6570-6580.
92. Goedhart, J., Von Stetten, D., Noirclerc-Savoye, M., Lelimosin, M., Joosen, L., Hink, M.A., Van Weeren, L., Gadella Jr, T.W., and Royant, A. (2012). Structure-guided evolution of cyan fluorescent proteins towards a quantum yield of 93%. *Nature communications* *3*, 751.
93. Houdusse, A., Gaucher, J.-F., Kremontsova, E., Mui, S., Trybus, K.M., and Cohen, C. (2006). Crystal structure of apo-calmodulin bound to the first two IQ motifs of myosin V reveals essential recognition features. *Proceedings of the National Academy of Sciences* *103*, 19326-19331.
94. Cogli, L., Piro, F., and Bucci, C. (2009). Rab7 and the CMT2B disease. *Biochemical Society Transactions* *37*, 1027-1031.
95. Spinosa, M.R., Progida, C., De Luca, A., Colucci, A.M.R., Alifano, P., and Bucci, C. (2008). Functional characterization of Rab7 mutant proteins associated with Charcot-Marie-Tooth type 2B disease. *Journal of neuroscience* *28*, 1640-1648.
96. Gutierrez, M.G., Munafó, D.B., Berón, W., and Colombo, M.I. (2004). Rab7 is required for the normal progression of the autophagic pathway in mammalian cells. *Journal of cell science* *117*, 2687-2697.
97. Chen, C.-C. (2023). Electrophysiological Techniques on the Study of Endolysosomal Ion Channels. In *Endolysosomal Voltage-Dependent Cation Channels*, (Springer), pp. 217-233.
98. Chen, C.-C., Butz, E.S., Chao, Y.-K., Grishchuk, Y., Becker, L., Heller, S., Slaugenhaupt, S.A., Biel, M., Wahl-Schott, C., and Grimm, C. (2017). Small molecules for early endosome-specific patch clamping. *Cell chemical biology* *24*, 907-916. e904.
99. Di Paola, S., Scotto-Rosato, A., and Medina, D.L. (2018). TRPML1: The Ca²⁺ retaker of the lysosome. *Cell calcium* *69*, 112-121.

100. García-Añoveros, J., and Wiwatpanit, T. (2014). TRPML2 and mucolipin evolution. *Mammalian Transient Receptor Potential (TRP) Cation Channels: Volume I*, 647-658.
101. Venkatachalam, K., Hofmann, T., and Montell, C. (2006). Lysosomal localization of TRPML3 depends on TRPML2 and the mucopolipidosis-associated protein TRPML1. *Journal of Biological Chemistry* *281*, 17517-17527.
102. Progida, C., Cogli, L., Piro, F., De Luca, A., Bakke, O., and Bucci, C. (2010). Rab7b controls trafficking from endosomes to the TGN. *Journal of cell science* *123*, 1480-1491.
103. Progida, C., Nielsen, M.S., Koster, G., Bucci, C., and Bakke, O. (2012). Dynamics of Rab7b-dependent transport of sorting receptors. *Traffic* *13*, 1273-1285.
104. Oltrogge, L.M., Wang, Q., and Boxer, S.G. (2014). Ground-state proton transfer kinetics in green fluorescent protein. *Biochemistry* *53*, 5947-5957.
105. Tadross, M.R., Park, S.A., Veeramani, B., and Yue, D.T. (2009). Robust approaches to quantitative ratiometric FRET imaging of CFP/YFP fluorophores under confocal microscopy. *Journal of microscopy* *233*, 192-204.
106. Fouquet, C., Gilles, J.-F., Heck, N., Dos Santos, M., Schwartzmann, R., Cannaya, V., Morel, M.-P., Davidson, R.S., Trembleau, A., and Bolte, S. (2015). Improving axial resolution in confocal microscopy with new high refractive index mounting media. *PLoS one* *10*, e0121096.
107. Colletti, G.A., and Kiselyov, K. (2011). Trpml1. *Transient Receptor Potential Channels*, 209-219.
108. Bucci, C., Bakke, O., and Progida, C. (2010). Rab7b and receptors trafficking. *Communicative & integrative biology* *3*, 401-404.

8 Publications

Colin Feldmann, Michael Schänzler, Manu Ben-Johny, Christian Wahl-Schott (2023): **Protocol for deriving proximity, affinity, and stoichiometry of protein interactions using image-based quantitative two-hybrid FRET.** *STAR protocols*, *4*(3), 102459.

Carla Abrahamian, Rachel Tang, Rebecca Deutsch, Lina Ouologuem, Julia Blenninger, Eva-Maria Weiden, Veronika Kudrina, Julia Rilling, Colin Feldmann, Youli Stepanov, Anna Scotto Rosato, Guadalupe Calvo, Marisol Soengas, Thomas Gudermann, Martin Biel, Christian Wahl-Schott, Cheng-Chang Chen, Karin Bartel, Christian Grimm: **Rab7a is a direct effector of the intracellular Ca²⁺ channel TPC2 regulating melanoma progression through modulation of the Wnt signaling pathway** *Nature Communications*, *in revision*

9 Appendix

9.1 List of abbreviations

A_{free}	Free donor molecules
APB	Acceptor photo-bleaching
ATP	Adenosine triphosphate
CaM	Calmodulin
CFP	Cyan fluorescent protein
CFP _{direct}	Corrected emission signal of donor fluorophore from direct excitation
D_{free}	Free donor molecules
E_A	Acceptor FRET efficiency
$E_{A,max}$	Acceptor maximum FRET efficiency
E_D	Donor FRET efficiency
$E_{D,max}$	Acceptor maximum FRET efficiency
EE	Early endosome
ELY	Early lysosome
FLIM	Fluorescence lifetime imaging
F_{ratio}	Fluorophore specific FRET calibration constant
FRET	Förster resonance energy transfer
$FRET_{max}$, or FRET maximum	Summarizes $E_{A,max}$ and $E_{D,max}$ if both are similar
GAP	GTPase activating protein
GDI	GDP dissociation inhibitor
GDP	Guanosine diphosphate

GEF	Guanine nucleotide exchange factor
G_{ratio}	Instrument specific FRET calibration constant
GTP	Guanosine triphosphate
ILV	Intraluminal vesicle
IQ6 <i>sapiens</i>	IQ6 motif of unconventional MyosinVa <i>homo sapiens</i>
K_D	Dissociation constant
$K_{D,eff}$	Effective K_D (similar to measured K_D)
LE	Late endosome
LY	Lysosome
MST	Microscale Thermophoresis
MT	Microtubuli
mTq2	mTurquoise2
MVB	Multivesicular body
mVen	mVenus
N_A	Estimated acceptor molecules
NAADP	Nicotinic acid adenine dinucleotide phosphate
N_D	Estimated donor molecules
ORF	Open reading frame
PCR	Polymerase chain reaction
PDB	Protein Data Base
PI(3,5)P ₂	Phosphatidylinositol-3.5-bisphosphate
R_{A1}	Cross excitation of acceptor fluorophore in FRET channel

R_{D1}	Emission bleed-through of donor fluorophore in FRET channel
R_{D2}	Cross excitation of donor fluorophore in YFP channel
REP	Rab exchange protein
$S_{CFP,FRET,YFP}$	Fluorescence signal acquired in each channel
SPR	Surface Plasmon Resonance
TGN	Trans golgi-network
TM	Transmembraneous
YFP	Yellow fluorescent protein
YFP_{direct}	Corrected emission signal of acceptor fluorophore from direct excitation
YFP_{FRET}	Corrected emission signal of acceptor fluorophore from donor excitation

9.2 Supplementary tables

Table 5. All plasmid constructs that I created. All plasmids were generated via classical restriction-ligation cloning as described.

Plasmid number	Plasmid name
CC#1	LSM12-mCherry
CC#2	LSM12-tdTomato
CC#3	LSM12-Venus
CC#4	Rab7
CC#5	mCherry-Rab7
CC#6	mCherry-Rab7 [Q67L]
CC#7	mCherry-Rab7 [T22N]
CC#8	tdTomato-Rab7
CC#9	mTq2-Rab7

CC#10	Venus-Rab7
CC#11	Venus-Rab7 [Q67L]
CC#12	Venus-Rab7 [T22N]
CC#13	CFP-Rab7
CC#14	Rab5
CC#15	Venus-Rab5
CC#16	mCherry-Rab5
CC#17	hTPC2-mTq2
CC#18	hTPC2-Venus
CC#19	mCherry C-terminal
CC#20	mCherry N-terminal
CC#21	tdTomato C-terminal
CC#22	tdTomato N-terminal
CC#23	Venus C-terminal
CC#24	mTq2 C-terminal
CC#25	mTq2 N-terminal
CC#26	Gamillus C-terminal
CC#27	mTq2-Calmodulin
CC#28	Venus-Myosin_Va
CC#29	hTPC1-Venus
CC#30	hTPC1 N-terminal
CC#31	hTPC2 N-terminal
CC#32	TPRML1 N-terminal
CC#33	TRPML1 Venus
CC#34	TRPML2 N-terminal
CC#35	TRPML2-Venus
CC#36	mTq2-Rab5
CC#37	mTq2-Rab5 [S34N]
CC#38	mTq2-Rab5 [Q67L]
CC#39	mTq2-Rab7 [Q67L]
CC#40	mTq2-Rab7 [T22N]

CC#41	mTq2-Rab4
CC#42	mTq2-Rab4 [Q72L]
CC#43	mTq2-Rab4 [S22N]
CC#44	LAMP1-Venus
CC#45	TRPML1-mTq2
CC#46	(d11)-mTq2-Rab7
CC#47	ALG1-Venus
CC#48	mTq2-ALG1
CC#49	LSM12-mTq2
CC#50	Arl8b-mTq2
CC#51	ALG2-Venus
CC#52	D6 Dimer GSG mTq2-Ven
CC#53	D10 Dimer GSG mTq2-Ven
CC#54	D18 Dimer GSG mTq2-Ven
CC#55	JPT2-iso1-mCherry
CC#56	JPT2-iso2-mCherry
CC#57	JPT2-iso3-mCherry
CC#58	D6 Dimer GSG mTq2-Gamillus
CC#59	D10 Dimer GSG mTq2-Gamillus
CC#60	D18 Dimer GSG mTq2-Gamillus
CC#61	hTPC2-mVen
CC#62	LAMP1-mVen
CC#63	TRPML1-mVen
CC#64	mTq2-Rab11
CC#65	mTq2-Rab11 [QL]
CC#66	SYNGR2-mTq2
CC#67	D3 Dimer GSG mTq2-mVen
CC#68	D42 Dimer LAMP1 forward
CC#69	D42 Dimer LAMP1 reversed
CC#70	D12 Dimer MCS mTq2-mVen
CC#71	D2A Dimer mVen-mTq2

CC#72	JPT2-iso1-mTq2
CC#73	JPT2-iso3-mTq2
CC#74	D78 Dimer LAMP1 mTq2-mVen
CC#75	D105 Dimer LAMP1 mTq2-mVen
CC#76	LAMP1-mCherry
CC#77	D105 Dimer LAMP1 CFP-YFP
CC#78	D27 Dimer CFP-YFP
CC#79	Ccz1-mTq2
CC#80	D6 Dimer GSG CFP-YFP
CC#81	mTq2-Rab7B
CC#82	Ccz1-mVenus
CC#83	mTq2-Mon1A
CC#84	Rab7 Indel CRISPR eGFP
CC#85	Rab7 Indel CRISPR eGFP
CC#86	RFP-Rab7B
CC#87	Venus-IQ6 [F5A]
CC#88	Venus-IQ6 [M9A]
CC#89	Venus-IQ6 [R7A]
CC#90	Venus-IQ6 [L0A]
CC#91	RFP-Rab7B [TN]
CC#92	RFP-Rab7B [QL]
CC#93	Venus-IQ6 [F5A+M9A]
CC#94	hTPC2-iso1-mVen
CC#95	mVenus-IQ6 [F5A]
CC#96	mVenus-IQ6 [F5A+M9A]
CC#97	mVenus-IQ6 [R7A]
CC#98	hTPC1-iso2-mVenus
CC#99	mVen-IQ6 [mVen N212T]
CC#100	mVen-IQ6 [WT]
CC#101	mVen-IQ6 [R6A]
CC#102	mVen-IQ6 [K10i]

CC#103	D3 Dimer GSG mTq2-mVen [mVen N212T]
CC#104	TMEM63A-mTq2
CC#105	Ccz1-mVenus [mVen N212T]
CC#106	TMEM63A-mTq2
CC#107	TMEM63B-mTq2
CC#108	mVen C-terminal
CC#109	ML3-mVen

Table 6. Primer and restriction sites of plasmids of data shown here.

Plasmid	Primer sequence	Restriction site
mTq2	GTAGTCGAATTCATGGTGAGCAAGGGCGAGGAGC	EcoRI
mVen	Reverse: CGCGGATCCGGAATGGTGAGCAAGGGCGAGG	XhoI
D3	mTq2 Forward: CCCAAGCTTATGGTGAGCAAGGGCGAGG	HindIII
	mTq2 Reverse: CGCGGATCCCTTGTACAGCTCGTCCATGCC	BamHI
	mVen Forward: CGCGGATCCGGAATGGTGAGCAAGGGCGAGG	BamHI
	mVen Reverse: GTCGGGCCCTTACTTGTACAGCTCGTCCATGCCGAG	Apal
D42	mTq2 Forward: AGTCTAGCTAGCATGGTGAGCAAGGGCGAGGAG	NheI
	mTq2 Reverse: CGCGGATCCCTTGTACAGCTCGTCCATGCC	Kp2nI
	mVen Forward: ATAGGATCCGGAGGTGGAGGTATGGTGAGCAAGGGCGAGG	BamHI
	mVen Reverse: GTCGGGCCCTTACTTGTACAGCTCGTCCATGCCGAG	Apal
	LAMP1 Linker Forward: ATTACGGATCCAACACGACGGTGACAAGG	BamHI
	LAMP1 Linker Reverse: ATACCGGATCCGACGGTGGTGCCCTCGC	BamHI
D2A	mVen Forward: AGTCTAGCTAGCATGGTGAGCAAGGGCGAGGAG	NheI

	mVen Reverse: ATTA CT CCGGACTTGTACAGCTCGTCCATGCCG	Kp2nl
mTq2- Calmodulin	mTq2 Forward: AGTCTAGCTAGCATGGT G GAGCAAGGGCGAGGAG	NheI
	mTq2 Reverse: GAATCGCCATTCCGGATCCCTTGTACAGCTCGTCCATGC	BamHI
	Calmodulin Forward: TATCTAGGATCCATGGCTGACCAACTGACTGAAGAG	BamHI
	Calmodulin Reverse: TAGTATGGGCCCTCACTTCGCTGTCATCATTTGTACAAACTC	Apal
mVen-IQ6 [WT]	mVen Forward: AGTCTAGCTAGCATGGT G GAGCAAGGGCGAGGAG	NheI
	mVen Reverse: GAATCGCCATTCCGGATCCCTTGTACAGCTCGTCCATGC	BamHI
	IQ6 Forward: TATCATGGATCCACCATGAAAGCCATCGTCTACCTTC	BamHI
	IQ6 Reverse: TAGTATGGGCCCTTACTTCTTGTAGCGTTCCACAGAGC	Apal
IQ6 mutants	F5A Forward: GTGCTGCGCCCCGGCGGATG F5A Reverse: CATCATCCGCCGGGCGCAG	Site directed mutagenesis
	M9A Forward: GGCGGATGGCGGCCAAGC M9A Reverse: CACGCTTGGCCGCCATCC	
	R6A Forward: GTGCTGCTTCGCACGGATGATGG R6A Reverse: GGCCATCATCCGTGCGAAGCAGC	
	R7A Forward: GCTTCCGGGCGATGATGGC R7A Reverse: GCTTGGCCATCATCGCCCCG	
mTq2- Rab5	mTq2 Forward: AGTCTAGCTAGCATGGT G GAGCAAGGGCGAGGAG	NheI
	mTq2 Reverse: CGCGGATCCCTTGTACAGCTCGTCCATGCC	BamHI
	Rab5 Forward: AATCAGGATCCATGGCTAATCGAGGAGCAACAAGAC	BamHI
	Rab5 Reverse: TCATGGGGCCCCTTACTACAACACTGGCTTCTGGCTG	Apal

mTq2- Rab7A	mTq2 Forward: CTAGCTAGCATGGTGAGCAAGGGCGAGGAG	NheI
	mTq2 Overlap-Reverse: AGAGGTCATTCCGGATCCCTTGTACAGCTCGTCCATGCCGAG	Overlap extension PCR
	Rab7A Overlap-Forward: CTGTACAAGGGATCCGGAATGACCTCTAGGAAGAAAGTGTGCTG AAG	
	Rab7A Reverse: CCGAAGCTTTCAGCAACTGCAGCTTCTGCC	HindIII
Rab7A mutants	[Q67L] Forward: CACAGCAGGACTGGAACGGTTCC [Q67L] Reverse: CCGTTCCAGTCCTGCTGTGTCCC	Site directed mutagenesi s
	[T22N] Forward: GTCGGGAAGAACTCACTCATG [T22N] Reverse: GTTCATGAGTGAGTTCTTCCC	
mTq2- Rab7B	mTq2 Forward: AGTCTAGCTAGCATGGTGAGCAAGGGCGAGGAG	NheI
	mTq2 Reverse: GAATCGCCATTCCGGATCCCTTGTACAGCTCGTCCATGC	BamHI
	Rab7B Forward: ATAGGATCCGGAATGAATCCCCGGAAGAAGGTGG	BamHI
	Rab7B Reverse: AATAGGGCCCTCAGCAGCATCTGCTCCTTGAC	Apal
hTPC1- mVen	hTPC1 Forward: ATAACGCTAGCATGGAGTCTTGCTACATTGCC	NheI
	hTPC1 Reverse: GTCTGAATTCCCGGTAACGGTCTGGGAGCGC	EcoRI
	mVen Forward: GTAGTCGAATTCGATGGTGAGCAAGGGCGAGGAGC	EcoRI
	mVen Reverse: CTATGCGGCCGCTTACTTGTACAGCTCGTCCATGCC	NotI
hTPC2- mVen	hTPC2 Forward: GTACTIONGGCTAGCATGGCGGAACCCAGGCG	NheI
	hTPC2 Reverse: CATGCGGGAATTCTCCCCTGCACAGCCACAGGTG	EcoRI
	mVen Forward: GTACTIONGGCTAGCATGGCGGAACCCAGGCG	EcoRI
	mVen Reverse: CATGCGGGAATTCTCCCCTGCACAGCCACAGGTG	XhoI
TRPML1- mVen	TRPML1 Forward: GTGCAAGCTTATGACAGCCCCGGCG	HindIII
	TRPML1 Reverse: CTGAATTCATTACCAGCAGCGAATGC	EcoRI

	mVen Forward: GTAGTCGAATTCGATGGTGAGCAAGGGCGAGGAGC	EcoRI
	mVen Reverse: CATGTACCTCGAGTTACTTGTACAGCTCGTCCATGCC	Apal
TRPML2- mVen	TRPML2 Forward: ATCAGGCTAGCATGGCCCGGCAGCC	HindIII
	TRPML2 Reverse: GTACAAGCTTATGGCCCGGCAGCC	BamHI
	mVen Forward: CGCGGATCCGGAATGGTGAGCAAGGGCGAGG	BamHI
	mVen Reverse: GTCGGGCCCTTACTTGTACAGCTCGTCCATGCCGAG	Apal
TRPML3- mVen	/	De novo gene synthesis

9.3 Acknowledgements

Firstly, I want to thank my external supervisor, Professor Christian Wahl-Schott, who was very patient and extremely invested in shaping me into a good scientist. You, more than anyone else, changed the way I think and work scientifically. You always put great effort into improving my skills, which far exceeded any expectations. I am most thankful for that.

I would like to thank Professor Martin Biel for the kind supervision and great collaboration, which includes projects outside of this thesis. I am also grateful for the scientific discussions we had, which provided me with plenty inspiration to improve my scientific thinking.

Also, I would like to thank Dr. Michael Schänzler for providing the inspiration and curiosity for all things related to natural sciences. Talking about physics, math, teaching students, and discussing with you was the most fun and repeatedly made me aware that I am exactly where I want to be.

Lastly, I would like to thank all my colleagues and friends from the Hanover Medical School, as well as the people who welcomed me at the LMU Munich.